Chapter 2

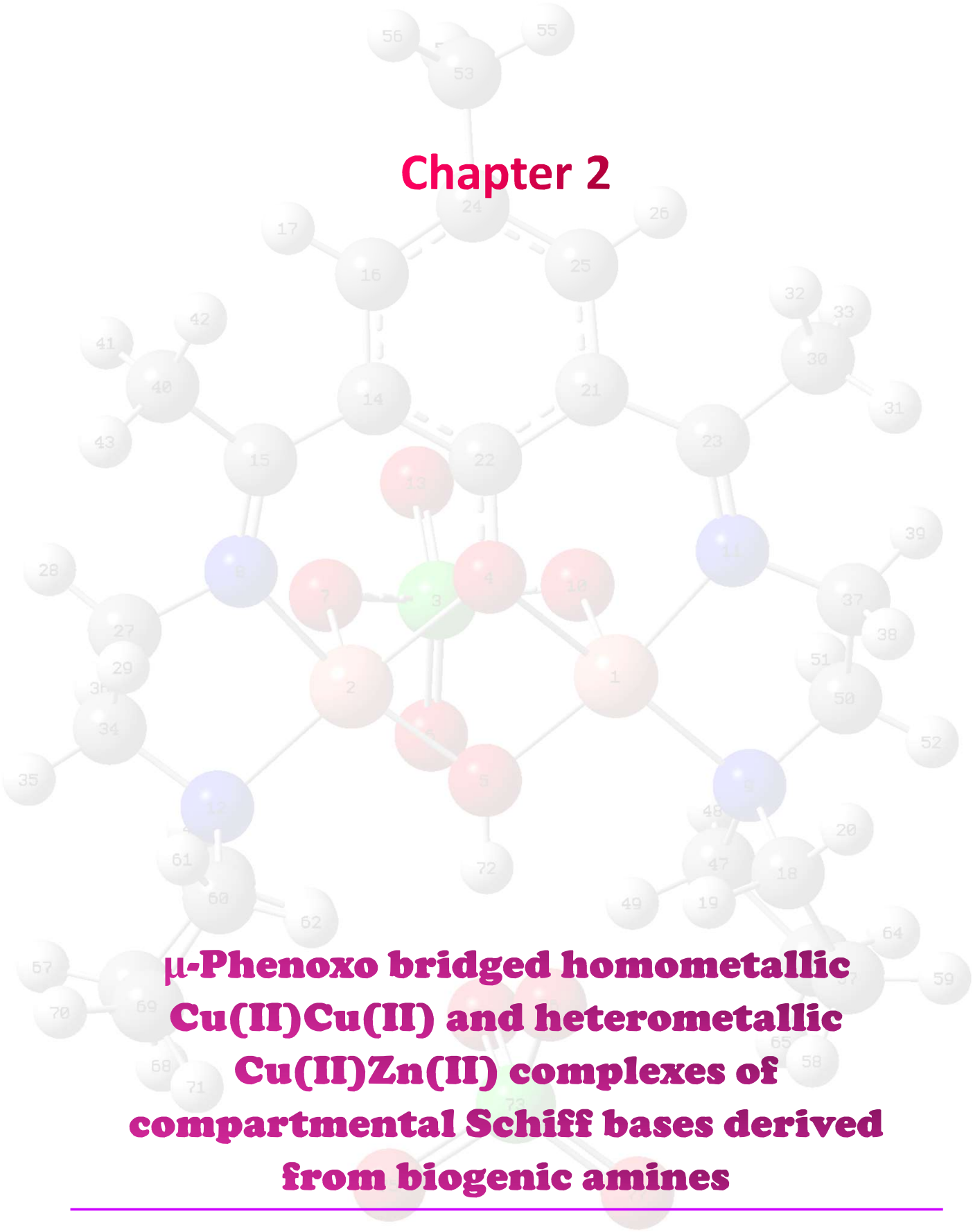

μ-Phenoxo bridged homometallic Cu(II)Cu(II) and heterometallic Cu(II)Zn(II) complexes of compartmental Schiff bases derived from biogenic amines

Chapter 2: μ-Phenoxo bridged homometallic Cu(II)Cu(II) and heterometallic Cu(II)Zn(II) complexes of compartmental Schiff bases derived from biogenic amines

2.1 Introduction

Immense attention of bioinorganic chemists has been drawn for studies and preparation of biomimetic models of oxidases, oxygenages, dehydrogenases and other metalloenzymes for dioxygen activation by dinuclear transition metal complexes. Multicopper oxidase comes from an important class of oxidase enzyme which contains five active sites based on the structural and functional properties of copper centre[1–3]. Since last several years, the complexes of macrocyclic and compartmental ligands have invited lot of attention due to their ability to hold metal ions in close proximity and facilitate electron and spin delocalization[4–6]. The main focus of these studies has been to understand the spin exchange interactions which has led to the evolution of structure-magnetism correlations[7–13] and understanding the role of bridging moieties[14–16]. The capability of the bridging moieties to hold the metal ions in proximity can modulate their redox potentials. Hence, systematic structural variations in ligands in such complexes are expected to help finely tune the redox behaviour of the metal centers. This fine tuning of redox potentials is expected to be the key factor in deciding the selectivity of active sites in redox enzymes, specially so in those having coupled binuclear active sites[17–23]. Attempts have been made to design dinuclear copper complexes using binucleating ligands, to accommodate two proximal copper ions which can have applications in modelling the active sites of many metalloenzymes[24–26] and hosting small molecules in catalysis[27–31]. Structural models of type-3 copper active sites in enzymes, like tyrosinase (hydroxylation of monophenols and oxidation of diphenols) and catechol oxidase (oxidation of catechols) with antiferromagnetically coupled binuclear copper centre have been developed. Some of them have been shown to possess catecholase activity[32–41]. The ability to oxidize diphenols is important in medical diagnosis for determination of hormonally active catecholamines, adrenaline, noradrenaline and dopa[42,43]. The direct use of these metalloproteins is difficult for their availability and stability in vitro while the synthetic mimics which function as highly efficient catalysts can be used to overcome this difficulty[26,40,41]. Thus, studies on the model compounds mimicking the catecholase activity are useful and promising for the development of new, more efficient bioinspired, environment friendly catalysts, for in vitro oxidation reactions. The development and design of relatively simple, synthetic models of active site structures of copper proteins are also of considerable interest for understanding their

unusual spectroscopic characteristics and the catalytic mechanisms[17,44–46]. The catecholase activity of various mononuclear and dinuclear complexes of copper (II) investigated in the past years point to the fact that a good steric match between dicopper(II) complex and substrate is necessary for good catalytic activity of a complex while several other parameters also can influence the activity[45,47]. Various structure-functional relationship studies have shown that the catecholase type activity of dicopper complexes depends on the metal-metal distance in dicopper(II) core[45,48–50] and the redox potentials of the sites[51,52]. Nature of the ligands (basicity, flexibility, electronic properties, functional groups over the ligands)[50,52,53] and the bridging unit can significantly affect the activity while, pH[54], solvents[55], concentration of dissolved oxygen can be the other parameters. The rate of oxidation of catechol to o-quinone is shown to depend on the basicity of donating sites of nitrogen-containing ligands[37,38,51,56,57]. The structural correlations in phenoxy-bridged dinuclear copper(II) complexes have been reported earlier where it is shown that the non-planar mononuclear as well as binuclear copper(II) complexes with Cu···Cu distance in the range 2.9–3.2 Å have better catecholase activity.

Toxic effects of superoxides in biological cells are protected by SOD enzymes. SODs have been divided into Cu-Zn SOD, Mn-SOD and Fe-SOD out of which first one is found in mammals based on the metal ions present on the active sites. Deficiency of SOD concentration in human body leads to various diseases and disorders like diabetes, cataract, ischemia, Parkinson's disease, cancer, etc. to overcome such harmful consequences, all oxygen metabolizing organisms possesses metalloenzymes known as superoxide dismutase (SODs). These SODs dismutase O_2^- radical to O_2 and H_2O_2. They employ ping pong mechanism shown in equations (i) and (ii), where M is a redox active metal center capable of oxidizing and reducing superoxide[58].

$$\mathbf{M^{ox} + O_2^- \rightarrow M^{red} + O_2 \text{ ---------- (i)}}$$

$$\mathbf{M^{red} + O_2 + 2H^+ \rightarrow M^{ox} + H_2O_2 \text{ ---------- (ii)}}$$

Synthetic superoxide distmutase (SOD) mimetics have emerged as a potential novel class drugs for the treatment of the oxidative stress related diseases. Many efforts have been made by bio-inorganic chemists for the synthesis of low molecular weight copper (II) complexes showing better SOD activity[59–65].

Ascorbic acid (AA) as a water-soluble vitamin is widely found in many fruits and vegetables. It can be absorbed by the human small intestine and plays an important role in immunity improvement, and cancer, heart disease and cardiovascular disease prevention[66]. Ascorbate oxidase (AAO) is a multi-copper enzyme which catalyzes the reduction of O_2 into water with oxidation of ascorbic acid (AA)[67]. Homogenous copper nano-clusters (Cu NCs) exhibited excellent ascorbic acid oxidase (AAO) mimic activities[68].

The activity of metallobiosites is better mimicked by the complexes of compartmental ligands (end-off, side-off and macrocycles) possessing endogenous phenoxide bridge[51,52]. Also, the complexes with alkoxo[48,69] or hydroxo[30,47] bridging ligands have been shown to be active. Though a lot of work on dicopper(II) complexes with catecholase type activity is reported, majority is with 3,5-di(tertiary butyl)catechol (3,5-DTBC) as substrate. There is a lacuna and no systematic studies have been reported on the selectivity of these complexes. Small molecule catalysts usually lack selectivity towards the substrate though it is one of the important properties of the enzyme active sites and hence needs to be explored.

With these considerations, it was thought worthwhile, developing new mimics of type 3 copper active sites to explore the structure-activity relationship by way of systematic variations in the ligand structures. To begin with, the binucleating ligands based on Schiff bases of biogenic amines have been considered.

2.1.1 Biogenic amines

A biogenic amine is *a biogenic substance with one or more amine groups. They are basic nitrogenous compounds formed mainly by decarboxylation of amino acids or by amination and transanimation of aldehydes and ketones*[70]. The list of notable biogenic amines is given in schematic representation (**Figure 2.1.1.1**).

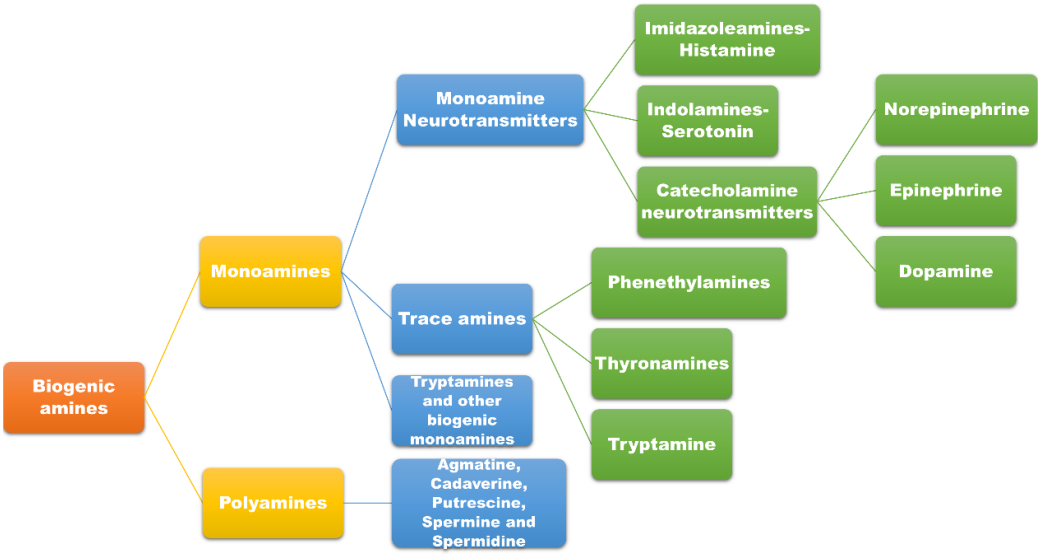

Figure 2.1.1.1 *A schematic representation of list of notable biogenic amines*

Tryptamine, histamine and pyridoxamine have been considered in the present study for their importance in biochemical processes and for their structures which are thought to be useful in designing new binucleating ligands.

Tryptamine is an indole-based amine of essential amino acid, tryptophan. Activation of 5-HT_4 receptors is done by tryptamine which are derived from dietary tryptophan with the help of symbiotic bacteria. These receptors regulate gastrointestinal motility in human guts[71,72]. It is primarily found in the brain, but also in the lungs, heart, intestines, liver, kidneys and urine. It acts as a neurotransmitter and as a serotonin releasing agent, modulating behavior and food intake[70]. For treatments of migraines, multiple tryptamine derived drugs have been developed[73].

Histamine is an organic nitrogenous compound involved in local immune responses, as well as regulating physiological functions in the gut and acting as a neurotransmitter for the brain, spinal cord, and uterus. It is a monoamine neurotransmitter. Decarboxylation of the amino acid histidine by the enzyme L-histidine decarboxylase yields histamine. It is either stored or rapidly inactivated by its primary degradative enzymes, histamine-*N*-methyltransferase. It plays a vital role in the body despite being small and is associated with functions such as gastric acid release, sleep-wake regulation, effects on nasal mucous membrane, vasodilation and fall in blood pressure etc.

Pyridoxamine is one form of Vitamin B_6. Both aminomethyl at position 4 and hydroxyl at position 3 of its ring possess variety of chemical reactivities which includes the scavenging of free radical species and carbonyl species formed in sugar and lipid degradation and chelation of metal ions that catalyze Amadori reactions. With a number of transition metal ions, it forms fairly weak complexes, with a preference for Cu^{+2} and Fe^{+3} metal ions[74,75].

Various group of researchers have worked on the synthesis of Schiff bases of various biogenic amines and studied their physico-chemical properties, structural properties and their biological applications[76–81]. Spectral, DFT and structural as well as conformational studies of metal complexes of various Schiff bases of biogenic amines have been reported[82–86].

This chapter deals with the synthesis of homometallic and heterometallic binuclear complexes of Schiff bases of biogenic amines formed by condensation with 2,6-diformyl-4-methylphenol (**Scheme 2.1.1.1**).

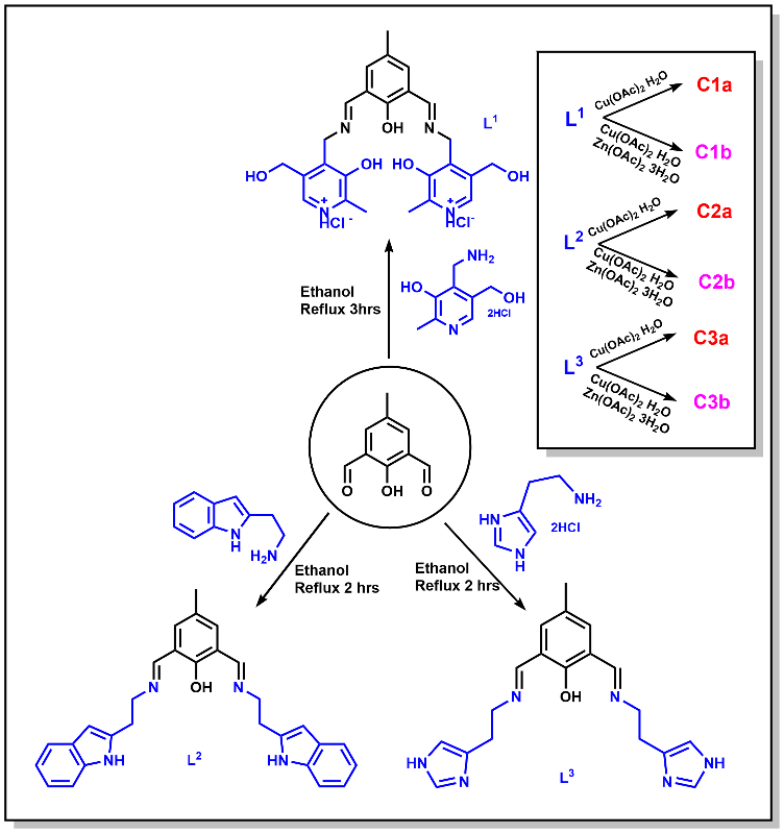

Scheme 2.1.1.1 *Schematic representation of synthesis of ligands (**L[1] -L[3]**) and complexes (**C1(a,b)-C3(a,b)**)*

These complexes were then explored for its catalytic promiscuity in terms of SOD mimic activity, Ascorbic Acid Oxidase activity and Catecholase activity (**Figure 2.1.1.2**).

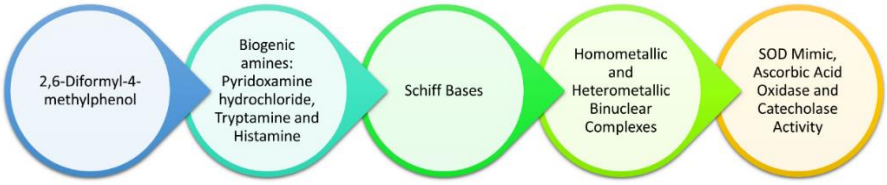

Figure 2.1.1.2 *Diagrammatic representation of synthesis and activities of synthesized complexes*

2.2 Experimental Section

2.2.1 Reagents and materials

p-Cresol, paraformaldehyde, sodium acetate, copper acetate monohydrate, Zinc acetate trihydrate and hexamine were procured from Merck. Pyridoxamine hydrochloride, tryptamine, 3,5-DTBC, 4-methyl catechol, dopamine, pyrocatechol, 2,3-dihydroxy naphthalene were purchased from Sigma Aldrich. Histamine dihydrochloride was purchased from Spectrochem. Ascorbic acid, potassium iodide and ammonium molybdate were purchased from Loba chem. β-NADH, phenazine methosulphate (PMS), nitroblue tetrazolium (NBT), acetic acid, sodium dihydrogen phosphate monohydrate and dibasic sodium phosphate (anhydrous) were purchased from SRL chemicals. All other chemicals used were of AR grade and were used as received. The solvents were distilled prior to use and dried according to standard procedures wherever necessary.

2.2.2 Synthesis of binucleating ligands

2.2.2.1 Synthesis of 2,6- diformyl-4-methylphenol (dfc)

2,6-Diformyl-4-methylphenol (dfc) was synthesized starting from p-cresol and following a modified literature procedure[87]: Hexamine (30 g, 20mmol) and paraformaldehyde (32g, 100mmol) were added to a solution of p-cresol (10.8g, 10mmol) in 50.0 ml glacial acetic acid. The mixture was allowed to stir continuously until a deep orange or brown viscous solution was obtained. Then the reaction mixture was heated to 70°-90°C for two hours. The solution was cooled to room temperature and conc. H_2SO_4 (10.0 ml) was added carefully. The resulting solution was allowed

to reflux for half an hour and then treated with distilled water (400.0 ml). A light-yellow coloured precipitate formed, was stored overnight at 4°C. The yellow product was isolated by filtration and washed with small amount of cold methanol till the filtrate had a single spot in TLC corresponding to the product. Yield: 4 g (24.4%) (lit. 35%). M.P.: 134-132°C. Solubility: Methanol, Ethanol, Chloroform, Dimethyl sulphoxide (DMSO).

*2.2.2.2 Synthesis of 2,6-bis-(2-(3-aminomethyl)pyridoxolideneamino)-4-methylphenol (**L^1**)*

4-Methyl-2,6-diformylphenol (0.082 g, 0.5mmol) was dissolved in hot ethanol (10 ml) and a solution of pydrioxamine hydrochloride (0.2591g, 1 mmol) in 5 ml of hot ethanol was added to it. The mixture was allowed to reflux for ~5h. The reaction was monitored by TLC. At the end of 5h, a single spot for the product appeared on TLC. The reaction mixture was concentrated to about 10 ml and cooled to obtain yellow-orange oil was obtained. The ligand was not isolated and was used for its complex synthesis.

*2.2.2.3 Synthesis of 2,6-bis-(2-(1H-indol-2-yl)ethyl)imino)methyl)-4-methylphenol (**L^2**)*

4-Methyl-2,6-diformylphenol (0.164 g, 1 mmol) was dissolved in hot ethanol (10 ml) and tryptamine (0.320g, 2 mmol) dissolved in hot ethanol (5 ml) was added to it. The mixture was allowed to reflux for 2 h. The reaction was monitored by TLC. At the end of 2 h, a single spot for the product appeared on TLC. The reaction mixture was concentrated to about 10 ml and cooled to obtain orange-yellow colour microcrystalline solid. The product was filtered and washed with cold ethanol to remove the traces of any soluble impurities. No purification method was employed as single spot was obtained on TLC. Yield: 0.319g (71.13%). Solubility: Chloroform, DMSO, DMF. M.P.: 84-85°C.

*2.2.2.4 Synthesis of 2,6-bis-(2-(2-aminoethyl)imidazolideneamino)-4-methylphenol (**L^3**)*

4-Methyl-2,6-diformylphenol (0.164 g, 1 mmol) was dissolved in hot ethanol (10 ml) and 4-(2-aminoethyl) imidazole dihydrochloride (0.368 g, 2 mmol) dissolved in hot ethanol (5 ml) was added to it. The mixture was allowed to reflux for ~$2^1/_2$ h. The reaction was monitored by TLC. At the end of $2^1/_2$ h, a single spot for the product appeared on TLC. The reaction mixture was concentrated to about 10 ml and cooled

to obtain yellow-orange microcrystalline solid. The product was filtered and washed with cold ethanol to remove the traces of any soluble impurities. No purification method was employed as single spot was obtained on TLC. Yield = 0.155 g (44.29%). Solubility: Methanol, Ethanol, DMSO. M.P.: 125-126°C.

2.2.3 Synthesis of homometallic and heterometallic binuclear complexes

*2.2.3.1 Synthesis of homometallic binuclear Copper(II) complex (**C1a**): [$Cu_2(L^1)(\mu$-Cl)]*

A hot ethanolic solution (5.0 ml) of 4-methyl-2,6-diformylphenol (0.082 g, 0.5 mmol) was added dropwise to a hot ethanolic solution (10 ml) of pyridoxamine hydrochloride (0.2411g, 1 mmol). The resulting mixture was allowed to reflux. The reaction was monitored by TLC for the formation of $\mathbf{L^1}$ and completion of the reaction. After 5 h, this solution was added to a hot ethanolic solution (15 ml) of cupric acetate monohydrate (0.1996g, 1 mmol). Immediately on mixing the two solutions, the colour of the reaction mixture became green. It was allowed to reflux further for 2 h. During this time, the colour of the solution changed from green to dark olive green and after 30 min, olive-green complex started precipitating as microcrystalline solid. The product was collected by filtration and washing several times with ethanol (10 x 2 mL). Yield: 0.130g (18.64%). Solubility: Methanol, DMSO, DMF

*2.2.3.2 Synthesis of heterometallic binuclear Copper(II) Zinc(II) complex (**C1b**): [CuZn (L^1)(μ-Cl)]*

A hot ethanolic solution (5.0 ml) of 4-methyl-2,6-diformylphenol (0.082g, 0.5 mmol) was added dropwise to a hot ethanolic solution (10 ml) of pyridoxamine hydrochloride (0.2411g, 1 mmol). The resulting mixture was allowed to reflux. The reaction was monitored by TLC for the formation of $\mathbf{L^1}$ and completion of the reaction. After $2^1/_2$ h, this solution was added to a hot ethanolic solution (15 ml) of zinc acetate dihydrate (0.10969g, 0.5 mmol) and the resulting mixture was allowed to reflux further for $^1/_2$ h. After completion of half an hour, hot ethanolic solution of copper acetate monohydrate (0.0998g, 0.5mmol) was added to the above solution and was allowed to reflux for about 2 hours. During this time, the colour of the solution changed from yellowish orange to light olive green and after 30 min, light olive-green complex started precipitating as microcrystalline solid. The product was collected by filtration and washing several times with ethanol (10 x 2mL). Yield: 0.145g (20.74%). Solubility: Methanol, DMSO, DMF.

*2.2.3.3 Synthesis of homometallic binuclear Copper(II) complex (**C2a**): [$Cu_2(L^2)_2(\mu$-$OAc)_2$]*

A hot ethanolic solution (5.0 ml) of 4-methyl-2,6-diformylphenol (0.164 g, 1 mmol) was added dropwise to a hot ethanolic solution (10 ml) of tryptamine (0.3204g, 2 mmol). The resulting mixture was allowed to reflux. The reaction was monitored by TLC for the formation of $\mathbf{L^2}$ and completion of the reaction. After 2 h, this solution was added to a hot ethanolic solution (15 ml) of cupric acetate monohydrate (0.399 g, 2 mmol) and the resulting mixture was allowed to reflux further for 2 h. During this time, the color of the solution changed from green to light green and after 30 min, light green complex started precipitating as microcrystalline solid. The product was collected by filtration and washing several times with ethanol (10 x 2 mL). Yield: 0.450g (39.54%). Solubility: Methanol, DMSO.

*2.2.3.4 Synthesis of heterometallic binuclear Copper(II) Zinc(II) complex (**C2b**): [$CuZn(L^2)_2(\mu$-$OAc)_2$]*

A hot ethanolic solution (5.0 ml) of 4-methyl-2,6-diformylphenol (0.164 g, 1 mmol) was added dropwise to a hot ethanolic solution (10 ml) of tryptamine (0.3204g, 2 mmol). The resulting mixture was allowed to reflux. The reaction was monitored by TLC for the formation of $\mathbf{L^2}$ and completion of the reaction. After $2^1/_2$ h, this solution was added to a hot ethanolic solution (15 ml) of zinc acetate dihydrate (0.219g, 1 mmol) and the resulting mixture was allowed to reflux further for $^1/_2$ h. After completion of half an hour, hot ethanolic solution of copper acetate monohydrate (0.199g, 1 mmol) was added to the above solution and was allowed to reflux for about 2 hours. During this time, the colour of the solution changed from yellowish orange to light olive green and after 30 min, light olive-green complex started precipitating as microcrystalline solid. The product was collected by filtration and washing several times with ethanol (10 x 2 mL). Yield: 0.543g (47.63%). Solubility: Methanol, DMSO.

*2.2.3.5 Synthesis of homometallic binuclear Copper(II) complex (**C3a**): $[Cu_2(L^3)(\mu\text{-}Cl)_2]_2$*

A hot ethanolic solution (5.0 ml) of 4-methyl-2,6-diformylphenol (0.082 g, 0.5 mmol) was added dropwise to a hot ethanolic solution (10 ml) of 4-(2-aminoethyl)imidazole dihydrochloride (0.184 g, 1 mmol). The resulting mixture was allowed to reflux. The reaction was monitored by TLC for the formation of **L^3** and completion of the reaction. After $2^1/_2$ h, this solution was added to a hot ethanolic solution (15 ml) of cupric acetate monohydrate (0.199 g, 1 mmol) and the resulting mixture was allowed to reflux further for 2 h. During this time, the colour of the solution changed from green to dark olive green and after 30 min, olive-green complex started precipitating as microcrystalline solid. The product was collected by filtration and washing several times with ethanol (10 x 2 mL). Yield: 0.178 g (65.2%). Solubility: Methanol, DMSO.

*2.2.3.6 Synthesis of heterometallic binuclear Copper(II) Zinc(II) complex (**C3b**): $[CuZn(L^3)(\mu\text{-}Cl)_2]Cl$*

A hot ethanolic solution (5.0 ml) of 4-methyl-2,6-diformylphenol (0.164 g, 1 mmol) was added dropwise to a hot ethanolic solution (10 ml) of 4-(2-aminoethyl) imidazole dihydrochloride (0.368 g, 2 mmol). The resulting mixture was allowed to reflux. The reaction was monitored by TLC for the formation of **L^3** and completion of the reaction. After $2^1/_2$ h, this solution was added to a hot ethanolic solution (15 ml) of zinc acetate dihydrate (0.219g, 1 mmol) and the resulting mixture was allowed to reflux further for $^1/_2$ h. After completion of half an hour, hot ethanolic solution of copper acetate monohydrate (0.199g, 1 mmol) was added to the above solution and was allowed to reflux for about 2 hours. During this time, the colour of the solution changed from yellowish orange to light olive green and after 30 min, olive-green complex started precipitating as microcrystalline solid. The product was collected by filtration and washing several times with ethanol (10 x 2 mL). Yield: 0.485g (66.42%). Solubility: Water, DMSO.

2.2.4 SOD mimic activity

The superoxide dismutase (SOD) activity was measured by using non-enzymatic method (NADH-PMS-NBT) (**Scheme 2.2.4.1**). [61,62,88,89] Superoxide anion ($O_2^{\cdot-}$) was generated by a non-enzymatic system containing 30 μM PMS and 80 μM NADH in phosphate buffer (pH=7.8) at RT (313 K) which reacted with 75 μM NBT to form bluish-black colored formazan complex. This bluish-black colour formazan complex

gives absorbance at 560nm. The absorbance of the solutions was monitored at 560.0 nm at various concentrations of the complexes under uniform conditions in triplicate experiments. The copper ions and their complexes can scavange the superoxide radicals and decrease the absorption at 560nm.

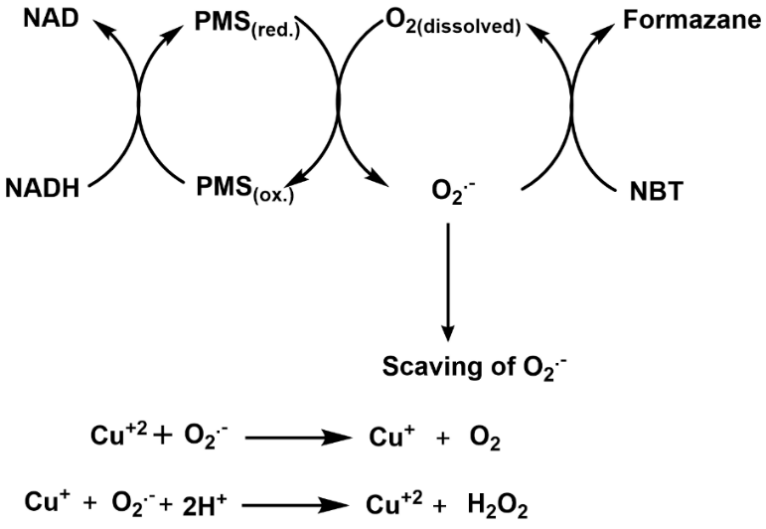

Scheme 2.2.4.1 *Generation of superoxide ($O_2^{\cdot-}$) radical by NADH-PMS-NBT assay and its scavenging*

The % inhibition of NBT reduction was calculated using the following equation:

$$\%\ \boldsymbol{inhibition\ of\ NBT\ reduction} = \left(1 - {}^{k'}/_{k}\right) \times 100 \qquad \ldots\ldots\ldots\ (\mathbf{2.1})$$

where k, k'= slope of the straight line obtained from absorbance values as a function of time in absence and presence of a complex. The IC_{50} value was calculated as the concentration of the complex that caused 50% inhibition of NBT reduction, from the plot of %inhibition as a function of concentration of complex (μM).

2.2.5 Ascorbic Acid Oxidase (AAO) activity

Conductivity water was used for preparation of acetate buffer (pH 5.5). Aqueous solutions of Ascorbic acid were made in acetate buffer. Ascorbic Acid Oxidase (AAO) activity of all synthesized complexes has been evaluated by kinetic studies with ascorbic acid as substrate wherein three different parameters such as substrate concentration, catalyst concentration and temperature have been varied. The ascorbate oxidase activity of all six complexes were studied by treating 2 x 10^{-6} M complex solution with 1 x 10^{-4} M ascorbic acid solution under aerobic condition at 30°C. The time dependent wavelength scan was performed in acetate buffer medium (pH 5.5) to

understand the potential of all complexes as catalyst towards the oxidation of ascorbic acid.

The kinetic study of the oxidation of ascorbic acid in presence of the complexes involved initial rate method. Solutions of ascorbic acid with concentrations ranging from 10 x 10^{-6} to 200 x 10^{-6} M were prepared from a 5 x 10^{-3} M stock solution. The dependence of the initial rate on the concentration of the ascorbic was monitored by UV-Vis spectroscopy by maintaining constant catalyst concentration (2 x 10^{-6} (**C1a, C2a** and **C2b**) or 4 x 10^{-6} M (**C2b**, **C3a** and **C3b**)) for each set. The catalyst concentration was varied for different complexes by maintaining constant substrate concentration 1 x 10^{-4} M. The reaction rates were obtained from the slope of the A × t plot by initial rate method. Rate units were calculated from ε = 14500 $dm^3mol^{-1}cm^{-1}$ (λ_{max} = 265 nm) for dehydroascorbic acid (DHAA) in acetate buffer (pH 5.5). A kinetic treatment on the basis of the Michaelis-Menten approach was applied and the results were evaluated from Lineweaver-Burk double reciprocal plots. The activation energy was evaluated by Arrhenius plot. The order of the reaction was determined using concentration dependence of rates by initial rate method.

2.2.6 Catecholase activity

Catecholase activity of all synthesized complexes has been evaluated by kinetic studies wherein three different parameters such as substrate concentration, catalyst concentration and temperature have been varied. Catalytic activity of the complex towards oxidation of five different diphenols, namely 3,5-DTBC, 4-methyl catechol, pyrocatechol, dopamine and 2,3-dihydroxy naphthalene has been evaluated. The reaction with pyrocatechol, dopamine hydrochloride and 2,3-dihydroxy naphthalene was found to be very slow. Hence, 3,5-DTBC and 4-methylcatechol have been selected for kinetic studies. The catecholase activity of all six complexes were studied by treating particular complex solution with different equivalents of 3,5-di-*tert*-butylcatechol (3,5-DTBC) under aerobic condition at 30°C and different equivalents of 4-methyl catechol solution under aerobic condition at 40°C. The time dependent wavelength scan was performed in methanol to understand the potential of all complexes as catalyst towards the oxidation of the substrate.

Table 2.2.6.1 *Temperature & Concentration of substrate and catalyst employed in this study*

Parameters		Concentration(mM)/Temp (°C)					
C2a							
3,5-DTBC	**Substrate**	[Cat=0.06mM and Temp= 30°C]					
		0.08	0.20	0.40	0.80	1.0	1.2
	Catalyst	[Sub=0.8 mM and Temp= 30°C]					
		0.02	0.04	0.06	0.08	0.10	
	Temperature	[Sub=0.8 mM and Cat=0.06 mM]					
		30	35	40	45	50	
4-MC	**Substrate**	[Cat=0.06mM and Temp= 30°C]					
		0.8	2	4	6	8	12
	Catalyst	[Sub=8 mM and Temp= 30°C]					
		0.02	0.04	0.06	0.08	0.10	
	Temperature	[Sub=8 mM and Cat=0.06 mM]					
		30	35	40	45	50	
C3a							
3,5-DTBC	**Substrate**	[Cat=0.02mM and Temp= 30°C]					
		1.9	9.6	17	21	24	
	Catalyst	[Sub=24mM and Temp= 30°C]					
		0.012	0.016	0.02	0.028	0.032	
	Temperature	[Sub=24 mM and Cat=0.02 mM]					
		30	35	40	45	50	
4-MC	**Substrate**	[Cat=0.08mM and Temp= 50°C]					
		40		45		50	
	Catalyst	[Sub=50mM and Temp= 50°C]					
		0.03	0.06	0.07	0.08	0.1	
	Temperature	[Sub=50 mM and Cat=0.08mM]					
		40	42	45	50	55	

The kinetic study of the oxidation of o-diphenol substrates in presence of all complexes was performed by initial rate method. The reaction rates were obtained from the slope of the A × t plot by initial rate method. Rate units were calculated from ε = 1900 $dm^3mol^{-1}cm^{-1}$ (λ_{max} = 390 nm) for 3,5-DTBQ in methanol and ε = 2140 $dm^3mol^{-1}cm^{-1}$ (λ_{max} = 392 nm) for 4-methylquinone in methanol. All reactions were carried out under aerobic conditions and were spectrophotometrically monitored at λ_{max} = 390 nm and λ_{max} = 392 nm respectively, for 3,5-DTBC and 4-methyl catechol.

A kinetic treatment on the basis of the Michaelis-Menten approach was applied and the results were evaluated from Lineweaver-Burk double reciprocal plots. The

activation energy was evaluated by Arrhenius plot. The order of the reaction was determined using concentration dependence of rates by initial rate method.

2.2.7 Physical Measurements

2.2.7.1 Infrared studies

Infrared spectra (4000 - 400 cm^{-1}) were recorded in the form of KBr pellets at 27ºC using Perkin Elmer RX1 FTIR spectrometer and Bruker Alpha Transmission FT-IR spectrometer. The solid sample was ground together with anhydrous KBr to form a homogenous mixture and then pressed in a 10mm die using hydraulic press to get transparent pellet which used for FT-IR analysis.

2.2.7.2 NMR studies

The ^{1}H and ^{13}C NMR spectra of all synthesized ligands were recorded on Bruker Avance (400 MHz) NMR spectrometer in $CDCl_3$ and DMSO-*d*6.

2.2.7.3 Mass spectral studies

The mass spectra of all ligands was recorded using DSQ2 GC–MS ThermoScientific spectrometer. ESI-Mass of all complexes were recorded using A B SCIEX LC-MS/MS 3200 QTRAP (MSU) and Waters Alliance E2695/HPLC-TQD mass spectrometer from CDRI Lucknow.

2.2.7.4 Electronic studies

Electronic spectra (200–900 nm) were recorded in methanolic and aqueous solutions using PerkinElmer UV-Vis spectrophotometer Model Lamda 35.

2.2.4.5 Photoluminescence studies

The emission spectra of all synthesized ligands and complexes were recorded on FP-6300 spectrofluorophotometer.

2.2.7.6 Elemental Analysis

Elemental analysis of synthesized complexes was recorded using EuroVector EA 300 from SAIF CDRI Lucknow.

2.2.7.7 Magnetic Susceptibility studies

Variable temperature magnetic susceptibility measurements were carried out in the temperature range of 90–295 K using an indigenous Faraday set up equipped with a

Mettler UMX5 ultramicrobalance at 0.8 Tesla. Diamagnetic corrections have been incorporated using Pascal constants.

2.2.7.8 ESR studies

ESR of all complexes were recorded using E-112 VARIAN USA spectrometer and JEOL ESR in solid and solution phase at LNT using X- band frequency with 9.3 GHz from SAIF IIT Bombay.

2.2.7.9 Single Crystal X-ray Diffraction studies

Single crystal diffraction data for the **complex C3a** was collected on an Xcalibur, EOS, Gemini four circle diffractometer with CCD plate detector using graphite monochromatic Cu Kα radiation (1.54184 Å). Absorption correction of multiscan type was applied and the data was processed using CrysAlisPro, Agilent Technologies, Version 1.171.37.33. Empirical absorption corrections were applied to the complex using spherical harmonics, implemented in SCALE3 ABSPACK scaling algorithm. The crystal was kept at 293(2) K during data collection. The cell refinement, data collection and reduction were computed by CrysAlisPro, Agilent Technologies, Version 1.171.37.33. Olex2[90] was used to solve the structure by Direct Methods with SHELXS[91,92] structure solution program and refined by full matrix least squares method based on F2 with all observed reflections with the SHELXL[91,92] refinement package. Graphics were generated using MERCURY (version 4.3.1). All non-hydrogen atoms were refined with anisotropic thermal parameters. The hydrogen atoms attached to carbon atoms were constrained to 'ride' on the atom attached to it. In all the cases, non-hydrogen atoms were treated anisotropically. Whenever possible, the hydrogen atoms were refined by locating on a difference Fourier map. In other cases, hydrogen atoms were geometrically fixed.

2.2.7.10 Molecular modelling studies

The complexes have been theoretically modelled by using GAUSSIAN 16 software program[93]. Molecular geometries of the ground state of the complexes were optimized by using B3LYP method[94] with 6-31G and LANL2DZ basis set[95,96]. Frontier molecular orbitals HOMO (highest occupied molecular orbital) and LUMO (lowest unoccupied molecular orbital) in the optimized structures of the molecule are visualized in Gauss View 6[97] and their energy has been calculated.

2.3. Results and Discussion

2.3.1 Characterization of ligands

2.3.1.1 IR spectra

The IR spectra of ligands, **L^2** and **L^3**, consist of all important bands expected for these molecules. The $\nu_{C=N}$ stretching in appears at around 1695 and 1682 cm^{-1} for ligands **L^2** and **L^3**, respectively. The N–H stretching frequency of indole in the free ligand **L^2** appears at 3407 cm^{-1}. The medium/strong band due to =C-H bending vibrations of indole ring has been observed at ~ 741 cm^{-1} (see **SI†: Fig. S2.5**). The N–H stretching frequency of imidazole appears as a weak band at 3103 cm^{-1} in the IR spectrum of the ligand **L^3**. A medium/strong band due to out of plane bending of imidazole ring is observed at 622 cm^{-1} in the free ligand **L^3** (see **SI†: Fig. S2.6**).

2.3.1.2 NMR Spectra

The chemical shift values observed in the NMR spectra corresponding to various types of H atoms / C atoms in the ligands along with their splitting patterns are listed below. They are in agreement with the structures of the ligands suggested in **scheme 2.1.1**.

2,6-Diformyl-4-methylphenol (dfc): ^{1}H NMR (δ ppm in $CDCl_3$): 2.397 (s, 3H, -CH_3), 7.782 (s, 2H, aromatic H), 10.227 (s, 2H, -CHO), 11.470 (s, 1H, -OH) (see **SI†: Fig. S2.1**).

L^2: ^{1}H NMR (δ ppm in DMSO-*d*6): 10.796 (s, 1H NH protons), 8.529 (s, 1H, H-C=N), 7.583,7.564 (d, 1H, indole ring), 7.487 (s, 1H, aromatic ring), 7.341, 7.321 (d, 1H, indole ring), 7.146,7.141 (d, 1H, indole ring), 7.081, 7.063, 7.045 (t, 1H, indole ring), 6.992, 6.972, 6.954 (t, 1H, indole ring), 3.897, 3.880, 3.863 (t, 2H, methylene protons attached to C=N), 3.065, 3.045, 30027 (t, 2H, methylene protons attached to indole ring), 2.25 (s, 3H, CH_3) (see **SI†: Fig. S2.2**).

^{13}C NMR (δ ppm in DMSO-*d*6): 160.45 (C=N), 136.64 (C of indole ring), 132.64 (C of aromatic ring), 127.63 (C of indole ring), 126.57 (C of indole ring), 123.36 (C of indole ring), 121.36 (C of indole ring), 118.84 (C of indole ring), 118.67 (C of indole ring), 112.30 (C of indole ring), 111.81 (C of indole ring), 60.37 (methylene carbon attached to C=N), 27.06 (methylene carbon attached to indole ring), 20.35 (CH_3) (see **SI†: Fig. S2.2**).

L^3: ^{1}H NMR (δ ppm in DMSO-*d*6): 11.419 (s, 1H, OH protons), 10.236 (s, 2H, H-C=N), 9.105 (s, 1H, N–H of imidazole), 8.263 (s, 1H, imidazole C-H), 7.859 (s, 2H, aromatic protons) 7.540 (s, 1H, imidazole C-H), 3.164 (t, 2H, methylene protons attached to C=N), 2.55 (t, 2H, methylene protons attached to imidazole ring), 2.333 (s, 3H, CH_3) (see **SI†: Fig. S2.3**).

^{13}C NMR (δ ppm in DMSO-*d*6): 192.80 (C attached to OH group), 160.78 (C=N), 137.84 (C of imidazole ring), 134.50 (C of aromatic region), 129.780 (C of imidazole ring), 129.260 (aromatic carbon attached to CH_3 group), 123.694 (aromatic carbon attached to C=N), 117.332 (C of imidazole), 37.77 (methylene carbon attached to C=N), 31.14 (methylene carbon attached to imidazole ring), 22.71 (CH_3) (see **SI†: Fig. S2.3**).

2.3.1.3 Mass spectra

In the mass spectrum of ligand **L^2**, a peak is observed at *m*/*z* = 494. However, in the chemical ionization, it undergoes extensive fragmentation to give more stable fragments with lower mass numbers (see **SI†: Fig. S2.8**). The ligand **L^3** was isolated as dihydrochloride salt, L^3.2HCl. In the mass spectrum of the ligand **L^3**, a peak is observed at *m*/*z* = 386, corresponding to the di-protonated monohydrochloride i.e. (L^3. HCl + H^+) formed on loss of chloride. Further loss of the second chloride with capture of an electron can result in the formation of (M^++2) species which is observed at 352 (see **SI†: Fig. S2.9**).

2.3.1.4 Electronic spectra

The electronic absorption spectra of all synthesized ligands have been recorded. In the ligands **L^2** and **L^3**, the π-π* and n-π* transitions are observed in the 200-300 nm and 300-500nm regions, respectively (**Figure 2.3.2.4.1**). Electronic spectra of all synthesized ligands have been listed in **Table 2.3.1.4.1** along with their ε_{max} values.

Table 2.3.1.4.1 *Electronic spectra of ligands (**L^2-L^3**)*

Complexes	λ_{max}/nm (ε_{max}/dm^{3}mol^{-1}cm^{-1})
	Intra-ligand transitions
L^2	**222(133333), 270(46333), 452(18067)**
L^3	**223(30236), 261(13858), 287(7669), 337(5338)**

2.3.1.5 Photoluminescence spectra

When solutions of ligands **L^2** and **L^3** were excited at 400nm, fluorescent emission at λ_{max} = 480nm and another weak overlapping emission at λ_{max} = 523nm was observed. Both **L^2** and **L^3** ligands showed fluorescence on excitation at 400nm (**Figure 2.3.2.5.1**).

2.3.2 Characterization of complexes

2.3.2.1 Elemental analysis

All six homonuclear and heteronuclear complexes were characterized by elemental analysis. The observed and calculated values of %C, %H and %N in the complexes are listed in**Table 2.3.2.1.1**. The observed values and the values calculated from the suggested empirical formulae are in agreement within the permissible error limits supporting the formulae of the complexes.

Table 2.3.2.1.1** Elemental analysis of complexes (**C1-C3)

Complex	Empirical formula (M.W.)	%C	%H	%N
C1a	$Cu_2C_{25}H_{25}O_5N_4Cl_3.3H_2O$	40.445	3.914	6.780
	(M.W.=748.5)	(40.080)	(4.408)	(7.481)
C1b	$CuZnC_{25}H_{25}O_5N_4Cl_3.3H_2O$	38.479	4.319	7.518
	(M.W.=750.38)	(39.980)	(4.131)	(7.462)
C2a	$Cu_2C_{62}H_{60}O_6N_8.2H_2O$	61.854	5.024	8.829
	(M.W.=1175)	(61.462)	(5.617)	(9.252)
C2b	$CuZnC_{62}H_{60}O_6N_8.2H_2O$	62.985	5.061	9.015
	(M.W.=1176)	(63.218)	(5.438)	(9.517)
C3a	$Cu_2C_{19}H_{20}O_1N_6Cl_2$	41.593	4.380	15.026
	(M.W.=546)	(41.758)	(3.660)	(15.380)
C3b	$CuZnC_{19}H_{21}O_1N_6Cl_3.0.5H_2O$	38.043	3.934	13.952
	(M.W.=627)	(38.449)	(3.710)	(14.165)

**The* values in parenthesis are calculated from the empirical formulae in column 2 of the table.

2.3.2.2 IR spectra

The IR spectra of the complexes have all important frequencies corresponding to the ligands. The most important frequencies are listed in **Table 2.3.2.2.1**.

Table 2.3.2.2.1 *IR frequencies of all synthesized complexes and ligands*

Complex	$\nu_{C=N}$ (cm^{-1})	ν_{N-H} (cm^{-1})	ν_{O-H} (cm^{-1})
C1a	1630	-	3406
C1b	1631	-	3431
L^2	1695	3407	-
C2a	1637	3397	-
C2b	1655, 1622	3395	-
L^3	1682	3103	-
C3a	1636	3201	-
C3b	1661, 1631	3245, 3395	-

The $\nu_{C=N}$ stretching frequency in the complexes, **C1-C3**, appears at ~1620-1660 cm^{-1}. These are shifted to lower frequencies as compared to that in the corresponding free ligand clearly indicating the participation of imine N in coordination with the metal ion. In case of heterometallic complexes, two separate bands corresponding to the $\nu_{C=N}$ has been observed due to the difference in the strength of interaction with two different metal ions resulting in different strength of the corresponding >C=N- bonds.

In the IR spectra of **C1a** and **C1b**, $\nu_{C=N}$ appears at 1630 and 1631 cm^{-1} and ν_{O-H} frequency is observed at 3406 and 3431 cm^{-1} for complex (see **SI†: Fig. S2.4**). In the IR spectra of **C2a** and **C2b**, $\nu_{C=N}$ appears at 1637 and 1655, 1622 cm^{-1} (see **SI†: Fig. S2.5**). The $\nu_{C=N}$ stretching in the complex has shifted to a lower frequency as compared to that of free ligand **L^2** (see **SI†: Fig. S2.5**), due to the participation of imine N in coordination with the copper ion in complex **C2a** but in case complex **C2b**, $\nu_{C=N}$ stretching appears at two different frequencies, clearly indicating the coordination of imine N to different metal centers, *viz.* copper and zinc. The N–H stretching frequency of indole appears as a weak band at 3397 cm^{-1} in complex **C2a** and 3395 cm^{-1} in complex **C2b**, while in the free ligand **L^2** it appears at 3407 cm^{-1}. This confirms the presence N-H in the complex and that there is no co-ordination of indole N-H to the metal center. The medium/strong band due to =C-H bending

vibrations of indole ring are observed at ~ 741 cm^{-1} in complex **C2a,** 743 cm^{-1} in complex **C2b** and at 741 cm^{-1} for the ligand $\mathbf{L^2}$.

In the IR spectra of complexes **C3a** and **C3b**, $\nu_{C=N}$ appears at 1636 and 1661, 1631 cm^{-1} (see **SI†: Fig. S2.6**). The $\nu_{C=N}$ stretching in the complex has shifted to a lower frequency as compared to that of free ligand $\mathbf{L^3}$ (see **SI†: Fig. S2.6**), indicating the participation of imine N in coordination with the copper ion in complex **C3a.** In **C3b**, $\nu_{C=N}$ stretching appears at two different frequencies, which supports the coordination of imine N to different metal centers, *viz.* copper and zinc. The N–H stretching frequency of imidazole in the complexes appears as a weak band at 3201 cm^{-1} in **C3a** and at 3245 cm^{-1} in **C3b**, while in the free ligand $\mathbf{L^3}$ it appears at 3103 cm^{-1}. The medium/strong band due to out of plane bending of imidazole ring is observed at 618 cm^{-1} in complex **C3b** while at 622 cm^{-1} in complex **C3a** and free ligand $\mathbf{L^3}$.

2.3.2.3 Mass spectra

In the mass spectrum of complex C1a, a peak is observed at *m/z*= 662.01 and 664.09, corresponding to $[Cu_2L_1]^+$ where as in complex C1b, a peak is observed at *m/z*= 665 corresponding to $[CuZnL_1]^+$ (see **SI†: Fig. S2.7**).

In complex C2a, the complex ion $[Cu_2(L^2)_2]^{2+}$ carries +2 charge which is compensated by acetate anions when it crystallizes. During ionization, the complex ion and the anion gets separated. The mass of complex cation $[Cu_2(L^2)_2]^{2+}$is 1020 and hence in the mass spectrum, the molecular ion peak appears at *m/z* = 510.31 (calcd. for $[Cu_2(L_2)_2]^{2+}/2$ = 510.5) (see **SI†: Fig. S2.8**).

In complex 2b, the mass of complex cation $[CuZn(L^2)_2]^{+2}$ is 1022. In the mass spectrum molecular ion peak appears at *m/z* = 694 (calcd. for $[CuZnL^2(OAc)_2]^+$ =693) (see **SI†: Fig. S2.8**).

In complex C3a, the monomeric complex ion $[Cu_2L^3]^{2+}$carries +2 charge which is compensated by chloride anions when it crystallizes. During ionization, the complex ion and the anions get separated. The mass of the complex cation, $[Cu_2L^3]^{2+}$ is 475 and hence in the mass spectrum, the molecular ion peak appears at *m*/*z* = 237.7 (calcd. for $([Cu_2L^3]^{2+})/2$ = 237.5) (see **SI†: Fig. S2.9**).

In complex C3b, the complex ion $[CuZn(L^3)Cl_2]^+$ carries +1 charge which is compensated by chloride anions when it crystallizes. During ionization, the complex ion and the anion gets separated. The mass complex cation $[CuZn(L^3)Cl_2]^+$ is 545 and hence the molecular ion peak appears at *m/z* = 545 (see **SI†: Fig. S2.9**).

2.3.2.4 Electronic spectra

The electronic absorption spectra of all homometallic complexes have a charge transfer band appearing at λ_{max} = 363 - 368 nm and that in heterometallic complexes appears at λ_{max} = 373 - 376 nm. This can be assigned to the metal to ligand charge transfer transitions. All complexes have a very broad and weak ligand field band in the range of 550–900 nm which is characteristic of highly distorted geometry around copper centres.

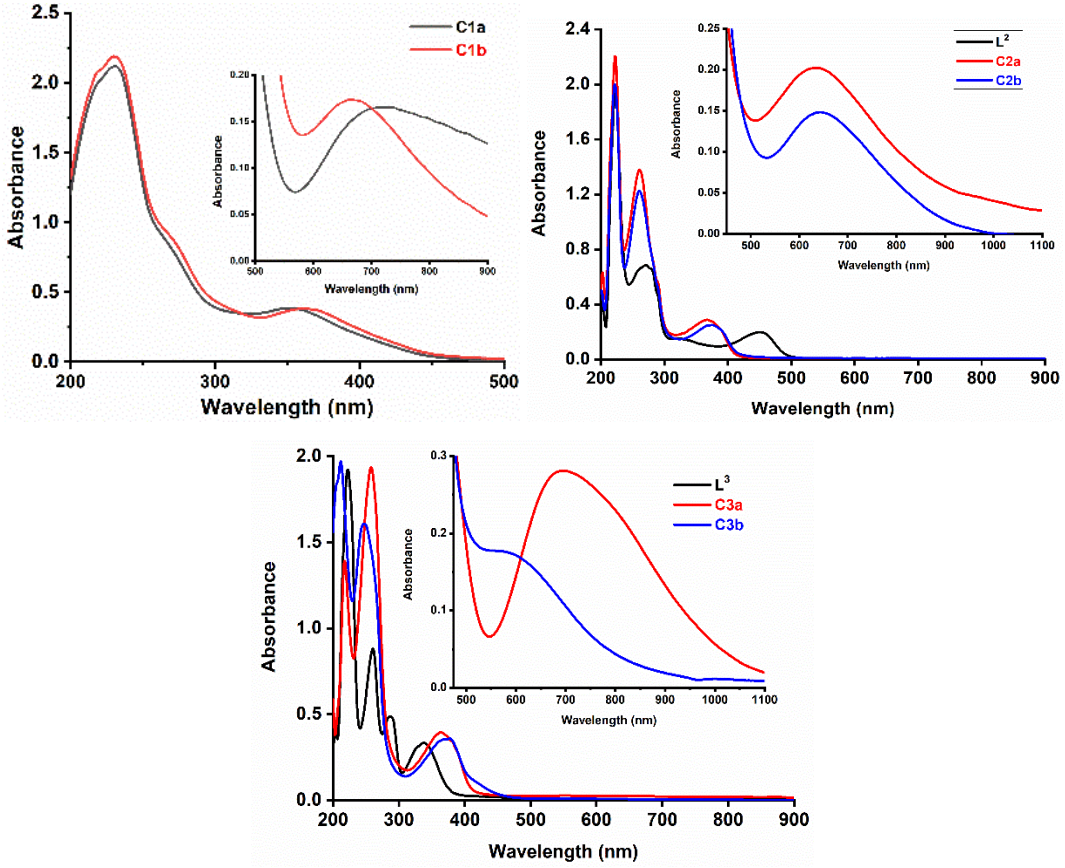

Figure 2.3.2.4.1 *Electronic spectra of (a)* ***C1a*** *&* ***C1b****, (b)* ***L²****,* ***C2a*** *&* ***C2b*** *and (c)* ***L³****,* ***C3a*** *&* ***C3b***

The intense bands observed at higher energy, in the range of 200-300 nm and 300-460nm are due to the intra ligand π-π* and n-π* transitions, respectively (**Figure 2.3.2.4.1**). The latter disappears in the complexes and is replaced by the MLCT

transitions. It is known that for a d^9 system in octahedral geometry, $^2T_{2g} \leftarrow {}^2E_g$ transition has energy between 600 and 700 nm. On distortion, this band undergoes a significant shift and broadening due to splitting of the spectral states and multiple transitions merging to form a broad band. The bands observed in the electronic spectra of all the ligands and complexes with their λ_{max} and ε_{max} values have been listed in **Table 2.3.2.4.1**.

Table 2.3.2.4.1 *Electronic spectra of ligands (**L^2-L^3**) and complexes **(C1-C3)***

Complexes	**λ_{max}/nm (ε_{max}/dm^{3}mol^{-1}cm^{-1})**		
	Intra-ligand transitions	**Charge transfer**	**d-d transitions**
C1a	231(52925), 267(21375)	352(9631)	718(165)
C1b	231(54700), 270(22200)	363(9530)	670(173)
L^2	222(133333), 270(46333), 452(18067)	-	-
C2a	222(66667), 261(41818)	368(8788)	635(200)
C2b	222(108108), 259(65946)	373(13405)	644(148)
L^3	223(30236), 261(13858), 287(7669),	-	-
C3a	337(5338)	363(14203)	695(178)
C3b	217(49285), 258(69107) 211(59848), 247(48393)	376(11030)	561(177)

2.3.2.5 Photoluminescence spectra

The homonuclear complex, **C1a** and all 3 heteronuclear complexes are found to emit fluorescent radiation when excited in their charge transfer bands. When solutions of **C1a** and **C1b** were excited at 350nm and 360nm, respectively, the emission band was observed at λ_{max} = 430nm (**C1a**) and λ_{max} = 428nm (**C1b**).

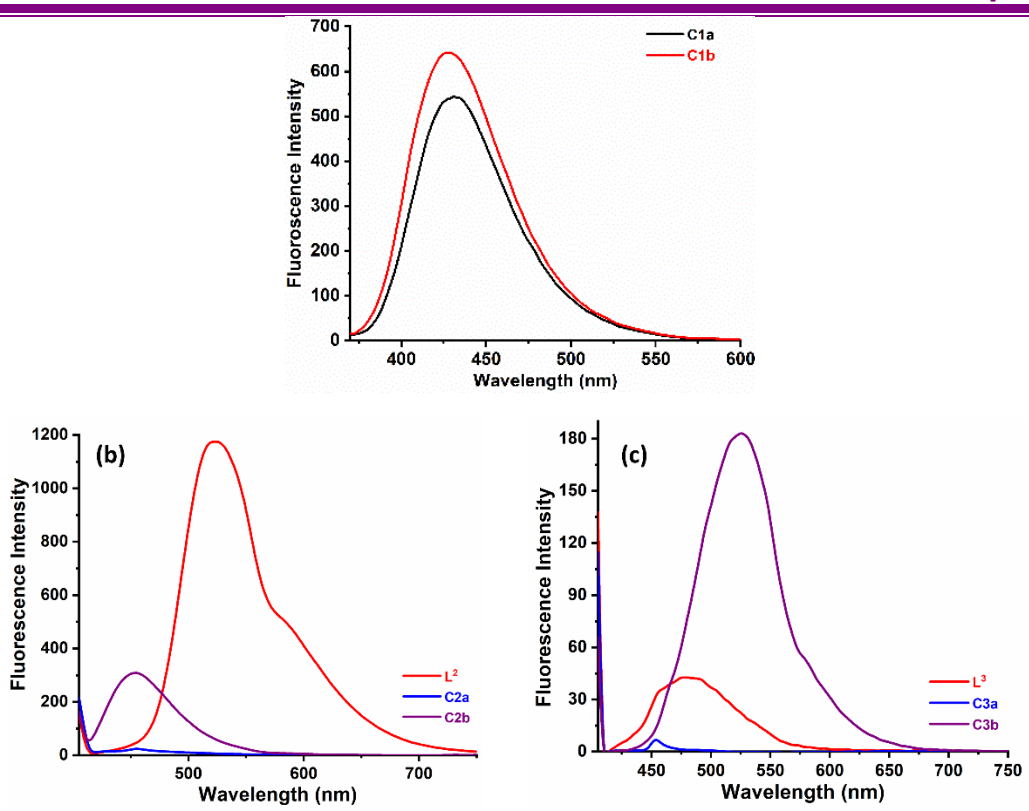

Figure 2.3.2.5.1 *Emission spectra of (a)* ***C1a*** *&* ***C1b*** *(b)* ***L²****,* ***C2a*** *&* ***C2b*** *and (c)* ***L³****,* ***C3a*** *&* ***C3b****.*

The ligand **L²** had emission at λ_{max} = 523nm when it was excited at 400nm. When the solutions of corresponding complexes, **C2a** and **C2b** were excited at 400nm, no emission peak was observed for complex **C2a** whereas **C2b** has an emission peak at λ_{max} = 454nm. Similarly, when ligand **L³**, complex **C3a** and **C3b** were excited at 400nm, the emission peak was observed at λ_{max} = 480nm for ligand **L³**, λ_{max} = 525nm for complex **C3b**. No emission was observed for complex **C3a**. That is the fluorescence of ligands **L²** and **L³** is quenched by the dicopper(II) complexes while in presence of the heteronuclear copper zinc complexes, give an emission peak on excitation at the same wavelength. The difference in the fluorescent emission is another evidence for the formation of heteronuclear copper zinc complexes (**Figure 2.3.2.5.1**).

2.3.2.6 Crystal Structure of complex ***C3a***

Green plate like crystals were obtained by vapour diffusion of diethyl ether into the methanolic solution of the complex **C3a**. The crystal structure of complex **C3a** was determined and is shown in **Figure 2.3.2.6.1**.

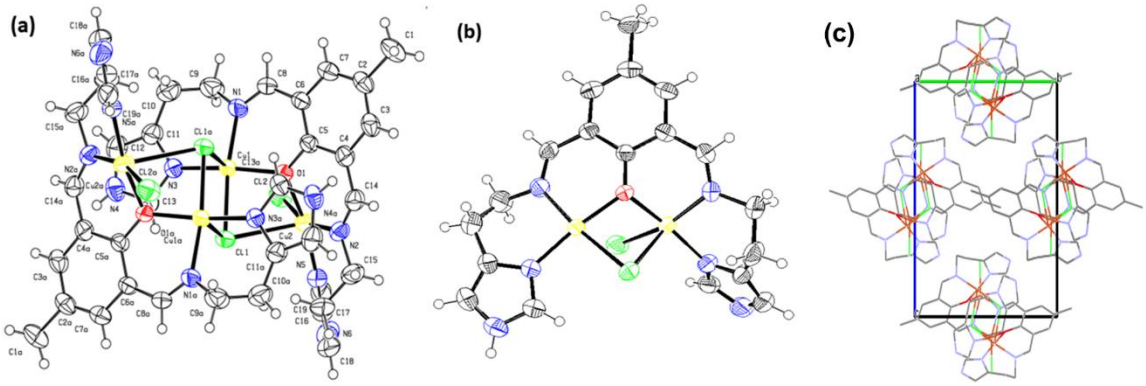

Figure 2.3.2.6.1 *ORTEP representation of (a) dimer of complex* ***C3a*** *(50% thermal ellipsoids) and (b) asymmetric unit of dimer of complex* ***C3a*** *(50% thermal ellipsoids); (c) projection of unit cell along a axis of complex* ***C3a***

The crystal data and structure refinement parameters of complex **C3a** are given in **Table 2.3.2.6.1**. Bond distances and bond angles relevant to metal coordination sphere of complex **C3a** are given in **Table 2.3.2.6.2**.

The complex forms a centrosymmetric dimer with two unshared chlorides, forming bridges between two binuclear moieties. The stereochemistry around copper(II) center is best described as distorted octahedral. The equatorial positions are occupied by the phenoxo oxygen O1, imine nitrogen N1, nitrogen of imidazole N3 and chlorine Cl1. The two axial positions are occupied by the chlorine Cl2 and chlorine Cl1a of the adjacent molecule forming a dimer. The Cu–O (phenoxo) distances Cu1-O1 and Cu2-O1 are 1.934(2) and 1.941(2) Å, respectively, which shows that the bridging by phenolic oxygens is almost symmetrical. The intradimer Cu1···Cu2 non-bonding distance between the two metal ions is 3.129 Å and the interdimer Cu1···Cu1a nonbonding distance between two metal ions is 3.718 Å.

Table 2.3.2.6.1 *Crystal data and structure refinement for complex* ***C3a***

Identification code	C3a
Empirical formula	$C_{38}H_{40}Cl_4Cu_4N_{12}O_2$
Formula weight	1092.82
Temperature/K	293(2)
Crystal system	monoclinic
Space group	$P2_1/c$
a/Å	14.01249(17)
b/Å	11.52420(10)
c/Å	14.94819(17)
α/°	90.00
β/°	99.7700(12)
γ/°	90.00
Volume/Å^3	2378.87(5)
Z	2
ρ_{calc}g/cm^3	1.526
μ/mm^{-1}	4.453
F(000)	1104.0
Crystal size/mm^3	0.3 × 0.2× 0.02
Radiation	CuK_α (λ = 1.54184)
2θ range for data collection/°	6.4 to 146.58
Index ranges	-17 ≤ h ≤ 17, -14 ≤ k ≤ 14, -13 ≤ l ≤ 18
Reflections collected	27465
Independent reflections	4777 [R_{int} = 0.0690, R_{sigma} = 0.0333]
Data/restraints/parameters	4790/0/276
Goodness-of-fit on F^2	1.116
Final R indexes [I>=2σ (I)]	R_1 = 0.0532, wR_2 = 0.1611
Final R indexes [all data]	R_1 = 0.0578, wR_2 = 0.1672
Largest diff. peak/hole / e Å^{-3}	0.84/-0.75

One of the imidazoles in the binucleating ligand gets deprotonated and coordinates as imidazolate ligand thus balancing the charge over the complex. It is known that the deprotonation of imidazole N–H is facilitated in presence of a coordinated metal ion in various complexes. The number of anions present in the complex suggested the deprotonation of one of the imidazolates. This chemical inference has been confirmed by considering 3 different possibilities both imidazole N–H intact, both deprotonated and one deprotonated. The R values for structure refinement were found to be substantially higher in the earlier two cases and it was minimum when one of the two imidazole N–H was considered deprotonated. The C–N bond distances in the two imidazole rings are accordingly different and are consistent with 1 N–H deprotonation (**Table 2.3.2.6.3**).

Table 2.3.2.6.2 *Bond Lengths and Angles related to metal coordination in complex* ***C3a****.*

Atom	C3a
Cu1-Cl1	2.3386(8)
Cu1-O1	1.934(2)
Cu1-N3	1.959(3)
Cu1-N1	1.988(3)
Cu2-Cl2	2.3004(10)
Cu2-O1	1.941(2)
Cu2-N5	1.939(3)
Cu2-N2	2.001(3)
O1-Cu1-Cl1	84.12(7)
O1-Cu1-N3	169.46(11)
O1-Cu1-N1	88.31(10)
N3-Cu1-Cl1	93.33(8)
N3-Cu1-N1	93.79(11)
N1-Cu1-Cl1	172.21(9)
O1-Cu2-Cl2	88.16(7)
O1-Cu2-N2	86.84(11)
N5-Cu2-Cl2	95.54(10)
N5-Cu2-O1	168.54(12)
N5-Cu2-N2	92.83(13)
N2-Cu2-Cl2	161.46(9)
Cu1-O1-Cu2	107.67(10)

Table 2.3.2.6.3 *Bond Lengths of both imidazole ring in complex C3a.*

Atom	Imidazole ring C1	Atom	Imidazolate ring C2
N3-C11	1.371(9)	N5-C17	1.358(8)
N3-C13	1.336(10)	N5-C19	1.327(7)
N4-C13	1.305(10)	N6-C18	1.346(10)
N4-C12	1.344(13)	N6-C19	1.340(8)
C11-C12	1.369(11)	C18-C17	1.345(10)

Both copper nuclei are coordinated by two nitrogen containing groups. Cu1 and Cu2 are coordinated by two sp^2 nitrogens, one imine nitrogen (N1 for Cu1 and N2 for Cu2) and one histamine nitrogen (N3 for Cu1 and N5 for Cu2). It should be noted that all the Cu–N distances fall in the range 1.96–2.04 Å. The N1-Cu1-N3 angle and N2-Cu2-N5 are 93.79(11) and 92.83(13). The projection of unit cell along *a*-axis of complex **C3a** (**Figure 2.3.1.7.1(c)**) shows discrete dimers of the binuclear complex containing four copper ions, occupying the lattice positions.

Similar complexes have been studied earlier by Grzybowski *et al*[98] and Lorosch *et al*[99] and have reported matching magnetic properties. In their study, the use of cupric chloride and cupric perchlorate with the same ligand yielded different complexes with chloride or hydroxo bridges, respectively.

While the use of cupric acetate monohydrate in the preparation of the present case yielded an altogether different complex with metal ions in different environment. In the present study, it is observed that one of the imidazoles undergoes deprotonation and binds as imidazolate with metal ions. This is unlike the earlier reports[98,99] where both imidazoles remain H-bound. The use of acetate in the reaction which provides slightly higher pH as compared to the solutions containing chloride or perchlorate salts appears to have played a key role in affecting the deprotonation of an imidazole. As a result of this, an entirely different molecule and crystals are obtained. Lorosch *et al*[99] obtained one dimensional infinite chains as against discrete chlorido bridged dimers, i.e. tetranuclear units, in the present case.

2.3.2.7. Magnetic measurements

Variable temperature magnetic study of the complexes was carried out in the temperature range of 90–295 K and the experimental magnetic susceptibility values were fitted to the modified Bleany-Bowers equation[100] (**equation 2.2**) in which the value of Nα has been fixed as 120×10^{-6} cm^3M^{-1}.

$$\boldsymbol{\chi_m = \left(\frac{Ng^2\beta^2}{3kT}\right)\left[3 + exp\left(\frac{-2J}{kT}\right)^{-1}\right](1-\rho) + 0.45\left(\frac{\rho}{T}\right) + N_\alpha} \quad \ldots\ldots\ldots\ldots (2.2)$$

χ_m is the molar magnetic susceptibility after correction for diamagnetism, g is the average g factor and ρ is the percentage of monomeric impurities; the other symbols have their usual meaning. The singlet-triplet energy separation (-2J) has been evaluated for the complexes. The J values were calculated by a nonlinear regression analysis in which - $2J$, ρ, and g are the variables. The least squares parameter R = $\Sigma(\chi_{exp} - \chi_{calcd})^2/\Sigma\,\chi^2_{exp}$ has been minimized. Plots of $\chi_m T$ and χ_m *vs* T (Figure 2.3.2.7.1.) and μ *vs* T (Figure 2.3.2.7.1.) for complex **C3a** clearly indicate antiferromagnetic character.

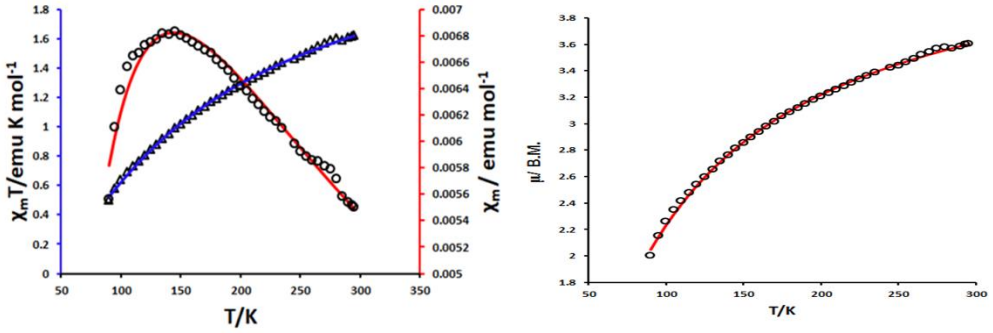

Figure 2.3.2.7.1 *Plot of $\chi_m T$ and χ_m vs T and μ vs T in* **C3a**

It is known that alkoxo- and phenoxido- bridged dicopper(II) species exhibit antiferromagnetic interaction when the Cu-O-Cu bond angle is larger than 97.60◦, the antiferromagnetic character increases with the increase in angle[101]. A very strong antiferromagnetic exchange coupling has also been observed in structurally closely related dicopper(II) centers bridged by phenoxide ligands[102,103] and those of the macrocyclic complexes[104]. The J value observed for the complex **C3a** is -115.663 ± 0.825 with χ_{TIP} = 120×10^{-6} cm^{3}mol^{-1} and ρ = 0.001 (0.1%). The moderately strong antiferromagnetic exchange is a result of Cu1-O-Cu2 bridge angle of 107.67º as observed in the crystal structure. Magneto-structural correlation in phenoxo-bridged dicopper(II) complexes reveals that the dominant pathway for super exchange through the oxygen bridge atoms involves interaction of the two copper (dx^2-y^2) orbitals and s and p orbitals on the oxygen with predominantly σ overlap[105]. Generally, phenoxo-bridged coplanar dicopper complexes with Cu-O_{ph}-Cu bridge angles of greater than 99º can have exchange coupling values as high as 420 cm^{-1} and for the complexes with bridge angles of <99º, the exchange interaction is <70 cm^{-1} [106]. Thus, the antiferromagnetic exchange interaction between the copper centers is likely to be influenced by the degree of planarity of the oxygen bridges, phenoxide bridge angle and the extent of out-of-plane displacement (τ) of the phenyl ring from oxygen atom within Cu_2O_2 core[107,108]. The intra and inter dimer chloride bridges appear to have significant influence besides phenoxides bridges in propagating the spin exchange.

2.3.2.8 ESR spectra

The ESR spectra of all complexes were recorded both in powdered and solution state at liquid nitrogen temperature (LNT). They all are typical axial ESR with most of them showing well resolved hyperfine splitting when recorded in frozen solution form at

77K. The hyperfine structure in the g_{II} region has four discernible lines due to coupling with the nuclear spin, I = 3/2, of the copper nucleus (**Figure 2.3.2.8.1**).

The complexes, C3a and C3b do not exhibit any hyperfine splitting in the ESR spectra recorded in the powder form due to averaging in the polycrystalline samples. The ESR spectra of C2a do not have hyperfine splitting in either of the two, solution and powder, forms. The g values and the hyperfine coupling constants for the complexes are summarized in **Table 2.3.2.8.1**.

Table 2.3.2.8.1 *g_{II}, $g_{\perp}$ and A_{II} or $A_{\perp}$ values of all complexes* ***(C1-C3)***

Complex	g_{II}	$g_{\perp}$	A_{II} x 10^{-4} cm^{-1}
C1a	2.41	2.08	135
C1b	2.27	2.04	180
C2a	2.22	2.12	-
C2b	2.29	2.06	171
C3a	2.41	2.08	124
C3b	2.27	2.04	180

It can be seen that the values of hyperfine coupling constants are similar to those observed in the normal copper sites in proteins and those corresponding to copper(II) ion in near square planar environment with moderately soft ligands providing N3O or N2O2 coordination environment. Further it is observed that the A_{II} values in the dicopper(II) complexes are significantly lower than those in Cu(II)Zn(II) heteronuclear complexes. This must be due to the presence of zinc ion which being hard may not allow delocalization of unpaired electron density. Hence, the unpaired electron density must be more near the copper nucleus resulting in stronger electron spin -nuclear spin coupling and higher A values.

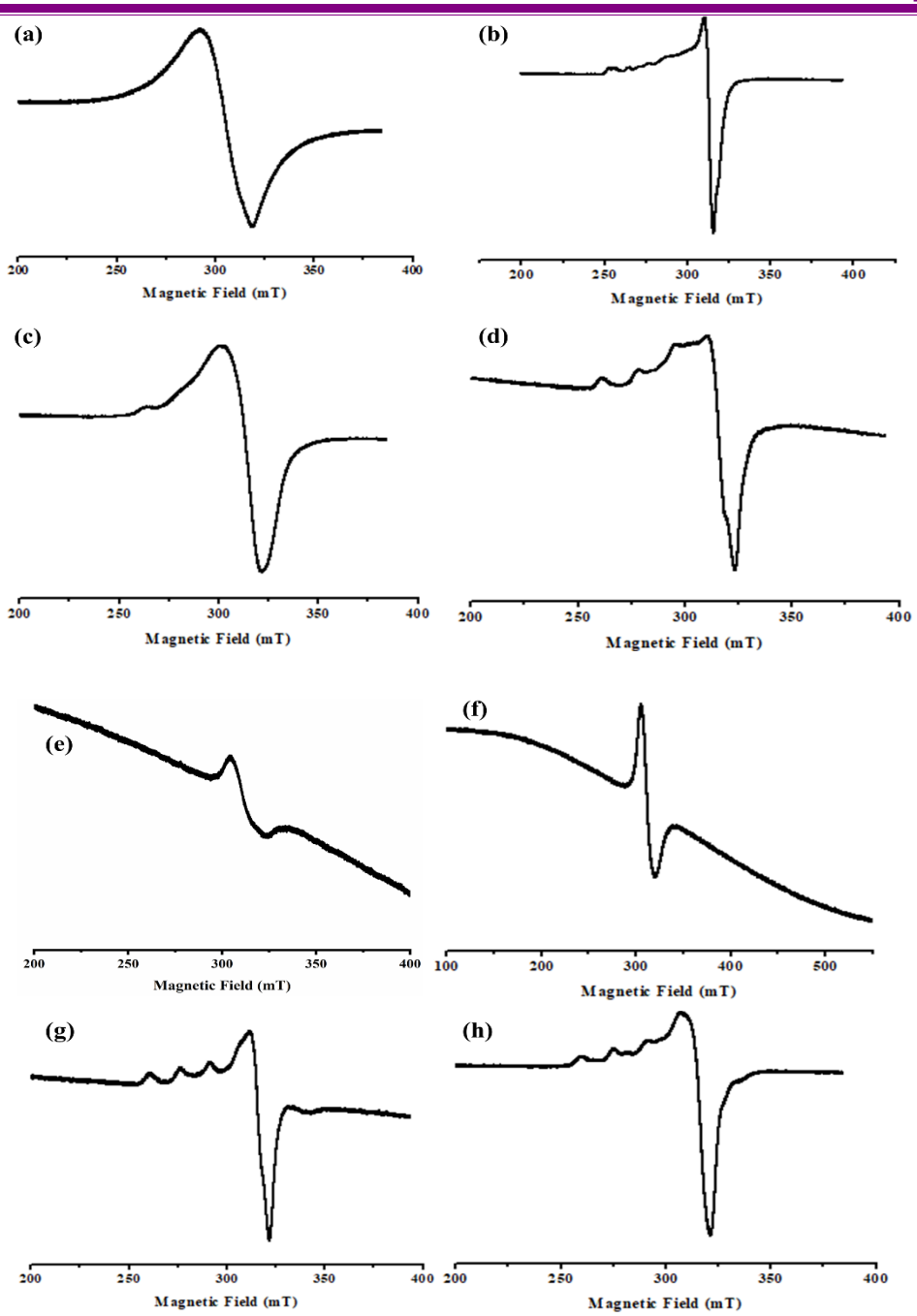

Figure 2.3.2.8.1 *ESR spectra of complexes at LNT (a)* ***C1a*** *(DMSO) (b)* ***C1a*** *(powder) (c)* ***C1b*** *(DMSO) (d)* ***C1b*** *(powder) (e)* ***C2a*** *(DMSO) (f)* ***C2a*** *(powder) (g)* ***C2b*** *(DMSO) (h)* ***C2b*** *(powder)*

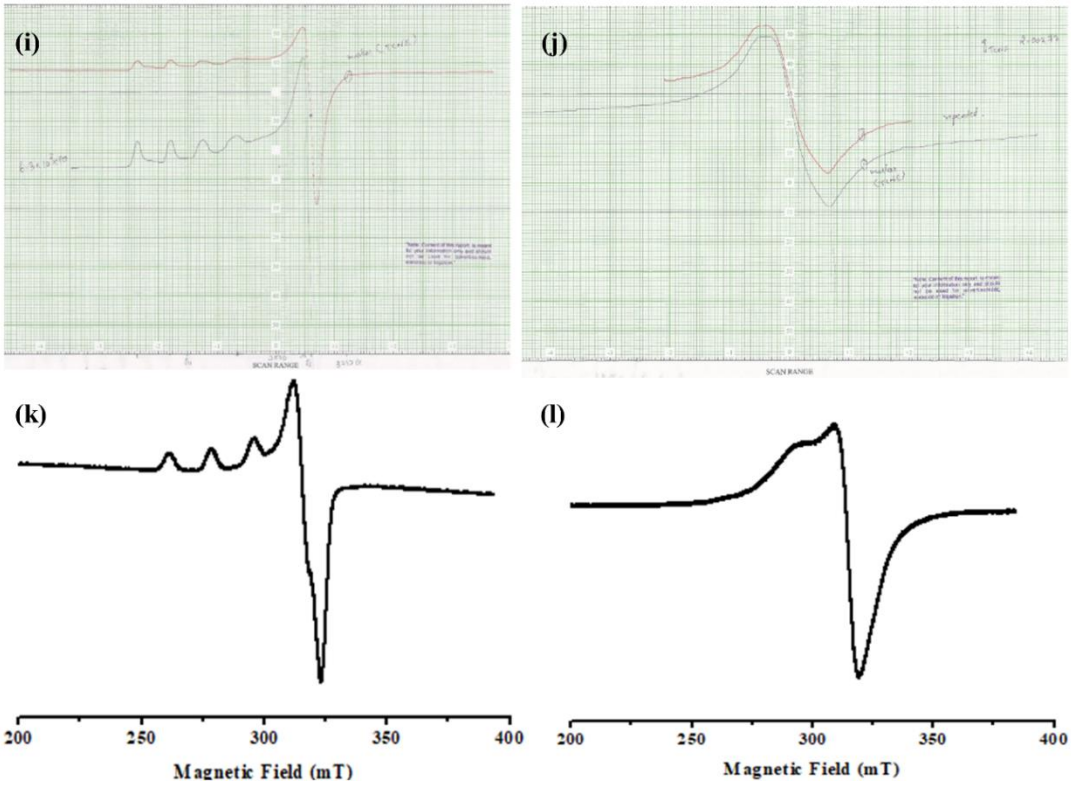

Figure 2.3.2.8.1 *(Contd….) ESR spectra of complexes at LNT (i)* ***C3a*** *(Methanol) (j)* ***C3a*** *(powder) (k)* ***C3b*** *(DMSO) (l)* ***C3b*** *(powder)*

2.3.2.9 Molecular Modelling

Computational studies for understanding the electronic structure of complexes **C1-C3** were performed by optimizing the theoretical geometrical parameters to get ground state structures in the gas phase using GAUSSIAN 16 program[93,95–97]. The calculated bond parameters are summarized (see **SI† in Table. S2.1**). The geometries of the complexes were optimized by B3LYP and LANL2DZ basis set (**figure 2.3.2.9.1**). Contour plots of HOMO and LUMO and their energy gap ΔE_g is shown in f**igure 2.3.2.9.2**. These energy gap ΔE_g plays an essential role in deciding their enzyme mimic and other biological activity[109]. This energy gap gives an idea about the chemical interaction of a molecule with other species. Hence, they are called frontier molecular orbitals. LUMO and HOMO acts as electron acceptor and electron donor[110], respectively. Theoretical transition energy between HOMO and LUMO frontier molecular orbitals were calculated by B3LYP and LANL2DZ methods in complexes **C1-C3** and are listed in **table 2.3.2.9.1**. This ΔE_g value reflects upon its catalytic activity[111,112]. The ΔE_g value for complex **C1a** is lowest which reflects the relationship with SOD mimic activity and could be considered as an active centre for SOD mimics[111,112]. **Figure 2.3.2.9.3** shows the graphical representations of ESP for

complexes **C1-C3**. The energy gap (ΔE_g) of the complexes were observed to have following order: **C1a** < **C3a** < **C1b** < **C2a** < **C2b** < **C3b**.

Table 2.3.2.9.1 *Global reactivity descriptors of complexes in eV calculated by DFT/B3LYP/LANL2DZ basis set*

Molecular Properties	Mathematical Description	C1a	C1b	C2a	C2b	C3a	C3b
E_{HOMO}	Energy of HOMO	-5.6034	-5.0069	-4.9598	-5.0997	-4.9138	-8.6543
E_{LUMO}	Energy of LUMO	-5.2945	-3.7748	-3.3201	-1.8803	-3.9886	-4.8561
Energy gap	$\Delta E_g = E_{LUMO} - E_{HOMO}$	0.3089	1.2321	1.6397	3.2194	0.9252	3.7982
Ionization potential (IP)	$IP = -E_{HOMO}$	5.6034	5.0069	4.9598	5.0997	4.9138	8.6543
Electron Affinity (EA)	$EA = -E_{LUMO}$	5.2945	3.7748	3.3201	1.8803	3.9886	4.8561
Electronegativity (χ)	$\chi = -\frac{1}{2}(E_{HOMO} + E_{LUMO})$	5.4490	4.3909	4.1400	3.4900	4.4512	6.7552
Chemical Potential (μ)	$\mu = \frac{1}{2}(E_{HOMO} + E_{LUMO})$	-5.4490	-4.3909	-4.1400	-3.490	-4.451	-6.755
Global Hardness (η)	$\eta = -\frac{1}{2}(E_{LUMO} - E_{HOMO})$	0.1545	0.6161	0.8199	1.6097	0.4626	1.8991
Softness (S)	$S = 1/2\eta$	3.2362	0.8116	0.6099	0.3106	1.0808	0.2633
Electrophilicity index (ω)	$\omega = \mu^2/2\eta$	96.089	15.6468	10.452	3.7840	21.415	12.014

The energy gap (ΔE_g), E_{HOMO} and E_{LUMO} values are important for the prediction of global reactivity descriptors, which in details explains the internal charge transfer, stability and reactivity of the molecule[112]. Global reactivity descriptors such as electronegativity (χ), global hardness (η), global electrophilicity (ω) and global softness (σ) are calculated using the formulas based on Koopmans theorem[113] (**equations 2.3 to 2.7**) as mentioned earlier and are listed in **table 2.3.2.9.1**.

$$\textit{Electronegativity}\ (\chi) = -\frac{1}{2}(I + A) \quad \ldots\ldots\ldots\ldots (2.3)$$

$$\textbf{Global Hardness}\ (\eta) = {}^{1}/_{2}\,(I - A)\ \ldots\ldots\ldots\ldots (2.4)$$

$$\textbf{Chemical Potential}\ (\mu) = {}^{1}/_{2}\ (E_{HOMO} + E_{LUMO})\ \ldots\ldots\ldots\ldots (2.5)$$

$$\textbf{Global Softness}\ (S) = 1/2\eta\ \ldots\ldots\ldots\ldots (2.6)$$

$$\textbf{Electrophilicity}\ (\omega) = {}^{\mu^2}/_{2\eta}\ \ldots\ldots\ldots\ldots (2.7)$$

The optimized structures of all synthesized complexes (**C1a,b-C3a,b**) are depicted in **figure 2.3.2.9.1**. Each copper(II) ion in homo nuclear copper(II) complexes, **C1a**, **C2a** and **C3a**, is four, six and five coordinated, respectively. Whereas in heteronuclear copper zinc complexes, each copper and zinc ion are four coordinated in complex **C1b**, six coordinated in complex **C2b** and five & six coordinated in complex **C3b**. In complex **C1a** and **C1b**, the copper-copper and copper-zinc centres are coordinated by phenolic oxygen, azomethine nitrogen, chloride bridge and phenolic oxygen of pyridoxamine and pyridine N is in salt form. In complex **C2a** and **C2b**, the copper-copper and copper-zinc centres are coordinated by phenolic oxygen, azomethine nitrogen (endogenous) and oxygen of acetate. In complex **C3a** and **C3b**, the copper-copper and copper-zinc centres are coordinated by phenolic oxygen, azomethine nitrogen, chloride bridge and nitrogen of imidazole ring. Besides these, some important geometrical parameters such as bond angles, bond lengths, torsion angles related to the coordination sphere of the complexes are listed in **Table S2.1**. The calculated bond lengths of Cu-N and Cu-O of these complexes are comparable to those reported for four and five coordinated complexes obtained from single crystal X-ray data.

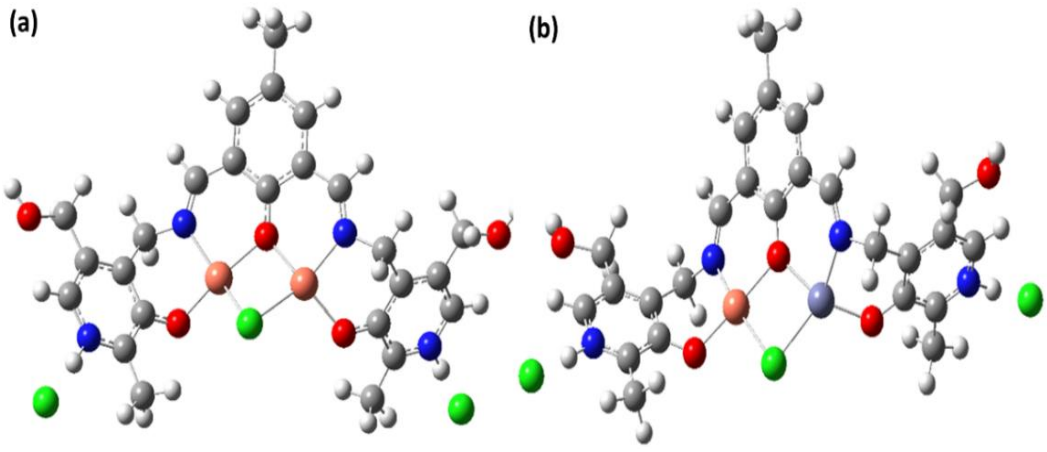

Figure 2.3.2.9.1 *DFT optimized structure of complexes (a)**C1a** (b) **C1b***

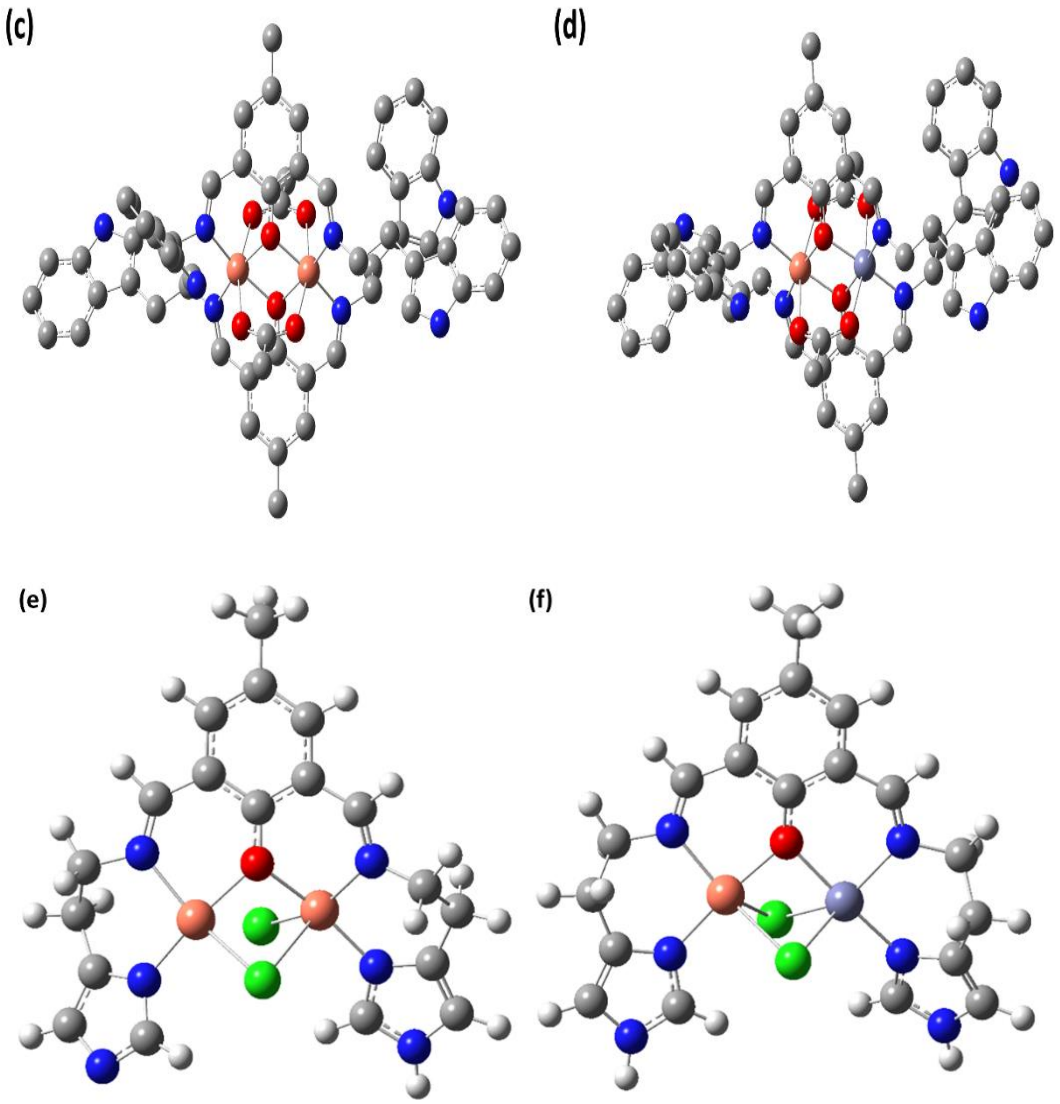

Figure 2.3.2.9.1 *DFT optimized structure of complexes (c)* ***C2a*** *(d)* ***C2b*** *(e)* ***C3a*** *and (f)* ***C3b***

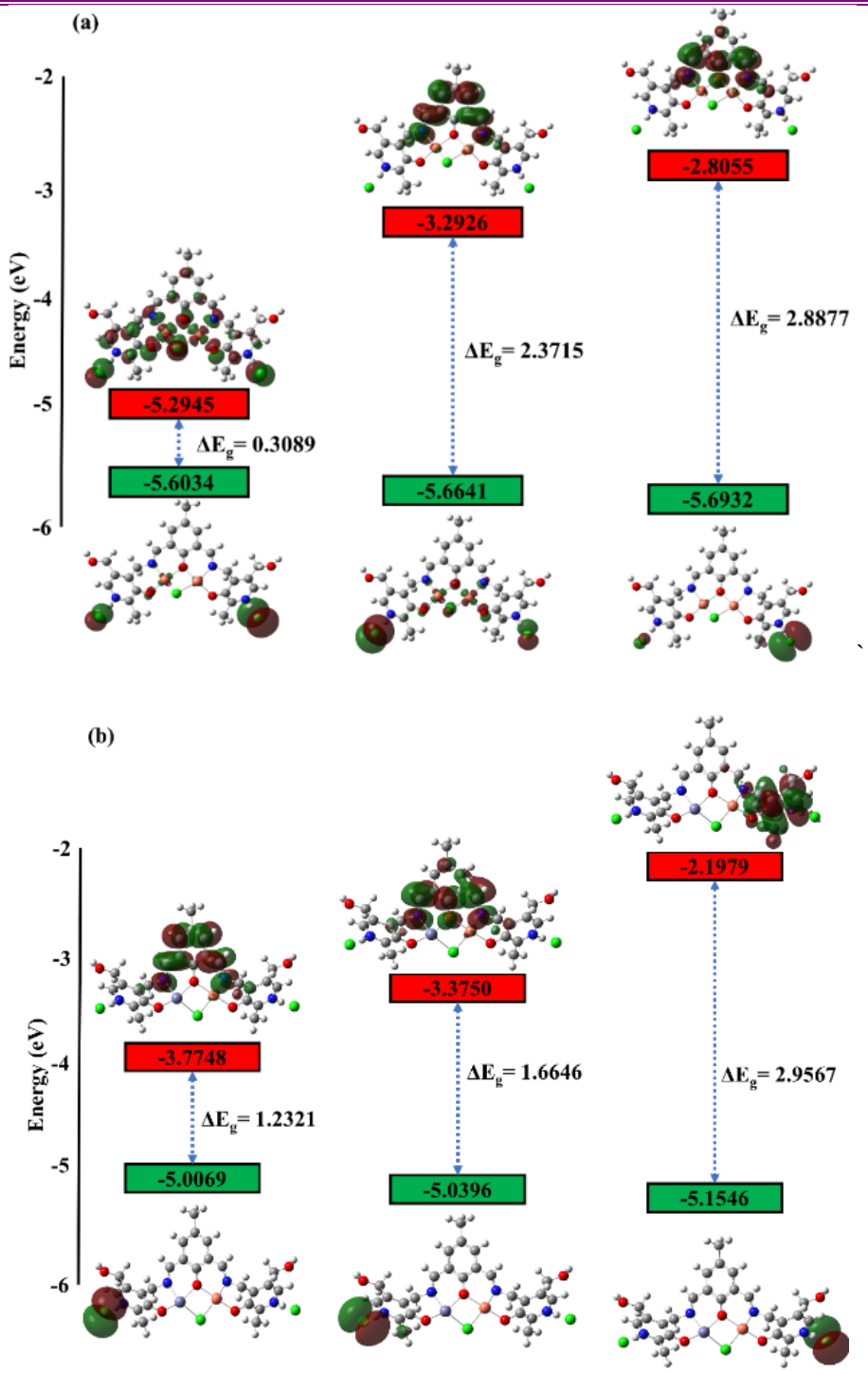

Figure 2.3.2.9.2 *Frontier molecular orbitals of complexes (a)* ***C1a*** *and (b)* ***C1b***

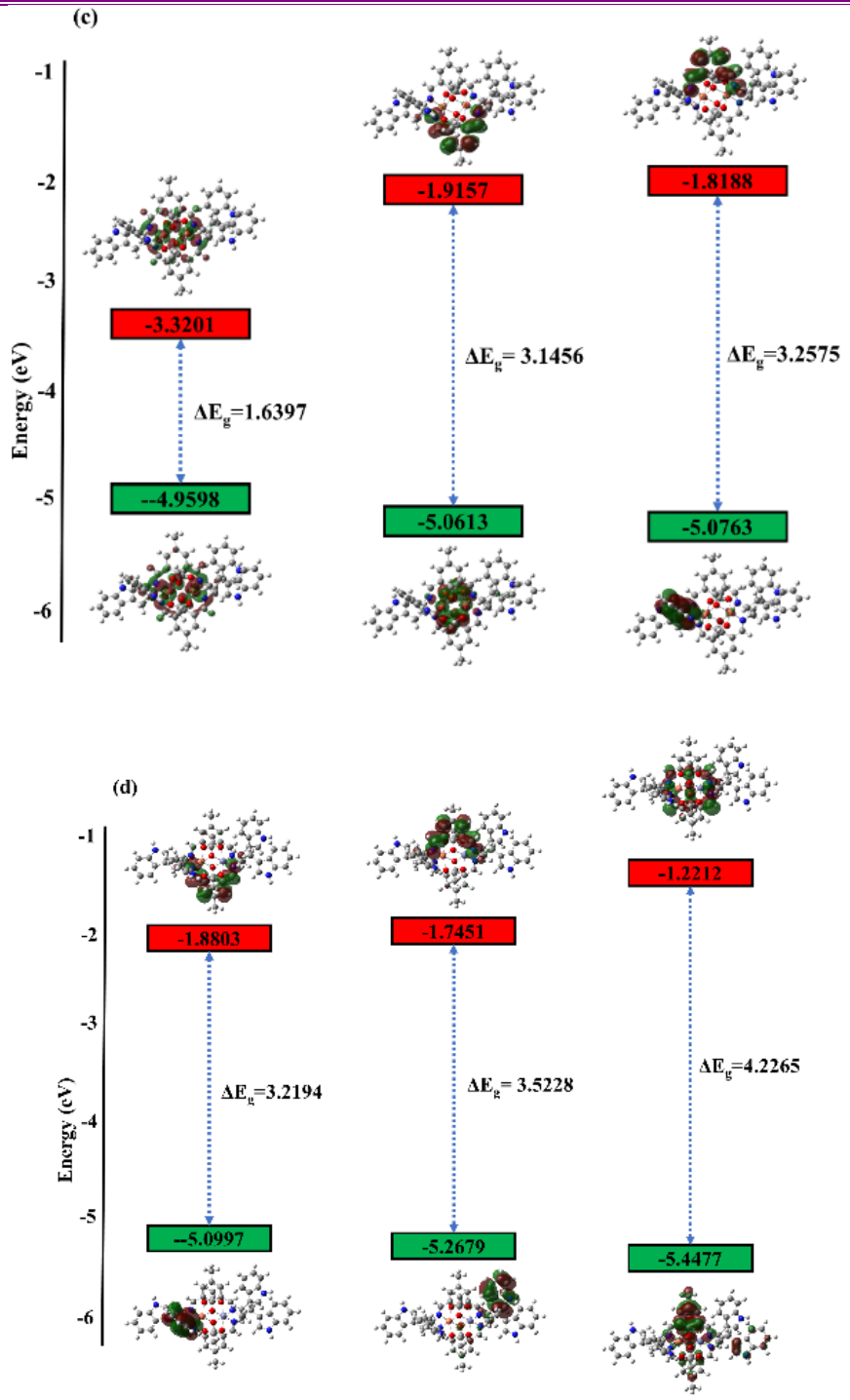

Figure 2.3.2.9.2 *(Contd…) Frontier molecular orbitals of complexes (c)* ***C2a*** *and (d)* ***C2b***

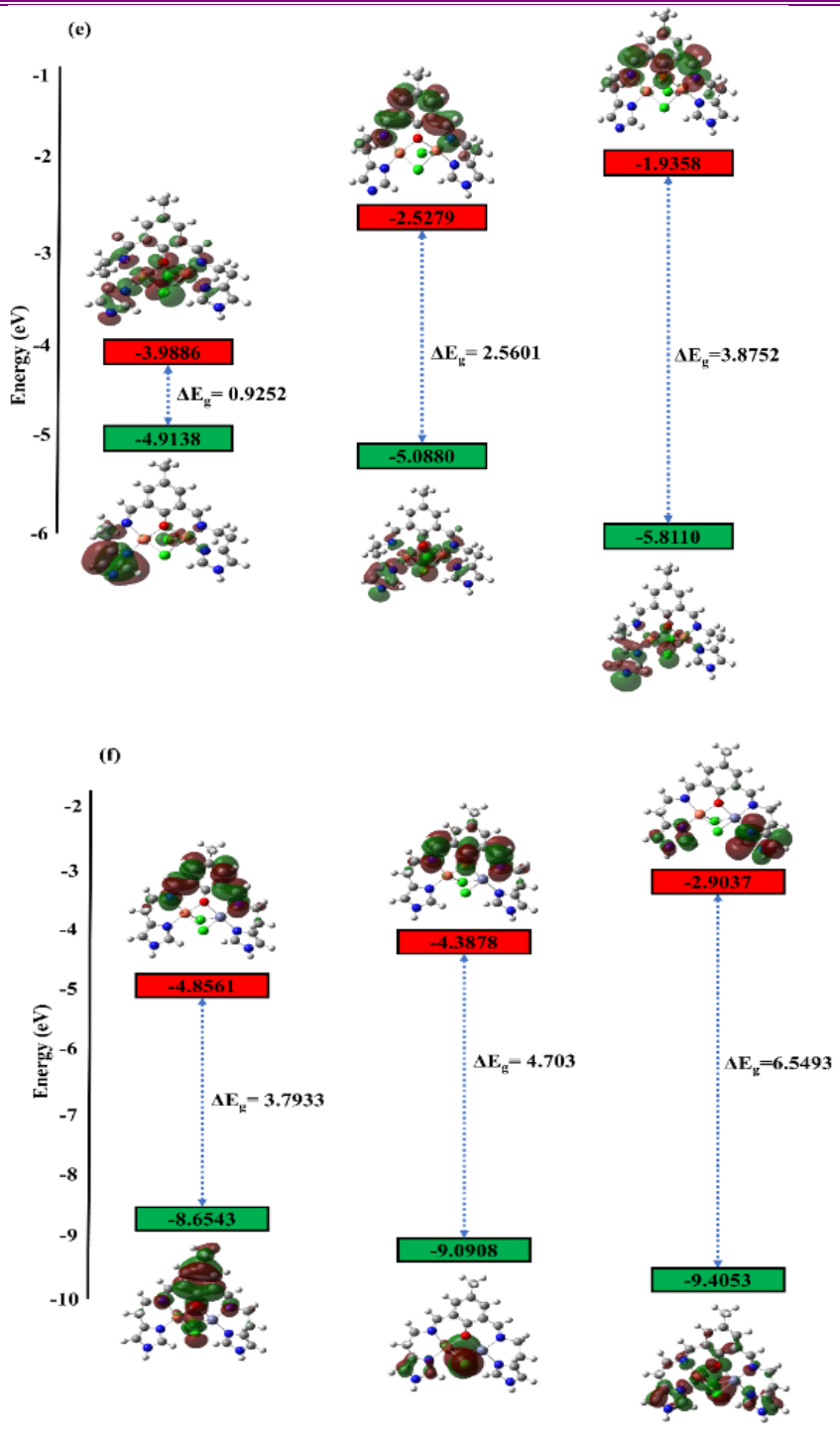

Figure 2.3.2.9.2 *(Contd…) Frontier molecular orbitals of complexes (e)* ***C2b*** *and (f)* ***C3a***

Yang and co-workers proposed four coordinated geometry parameters (FCGP), which is ascertained by the value of τ-index (τ_4 = 360- (α+β)/141°), where α and β are two largest angles[114]. The value of the geometry index (τ_4) ranges from 1.00 for a perfect tetrahedral geometry to 0 (zero) for a perfect square planar geometry. The geometry index value for each copper(II) ion and zinc(II) ion is different, but on the persual of

these index values, both metal centres appear to be in distorded square planar environment in all complexes. (**Table 2.3.2.9.2**).

Table 2.3.2.9.2 *Geometry Index (τ_4) parameters of complexes* ***C1*** *and* ***C3***

Complexes	Geometry index (τ_4)	
	Cu1	Cu2
C1a	0.471	0.333
C1b	0.134	0.573 (Zn)
C3a	0.753	-
C3b	-	-

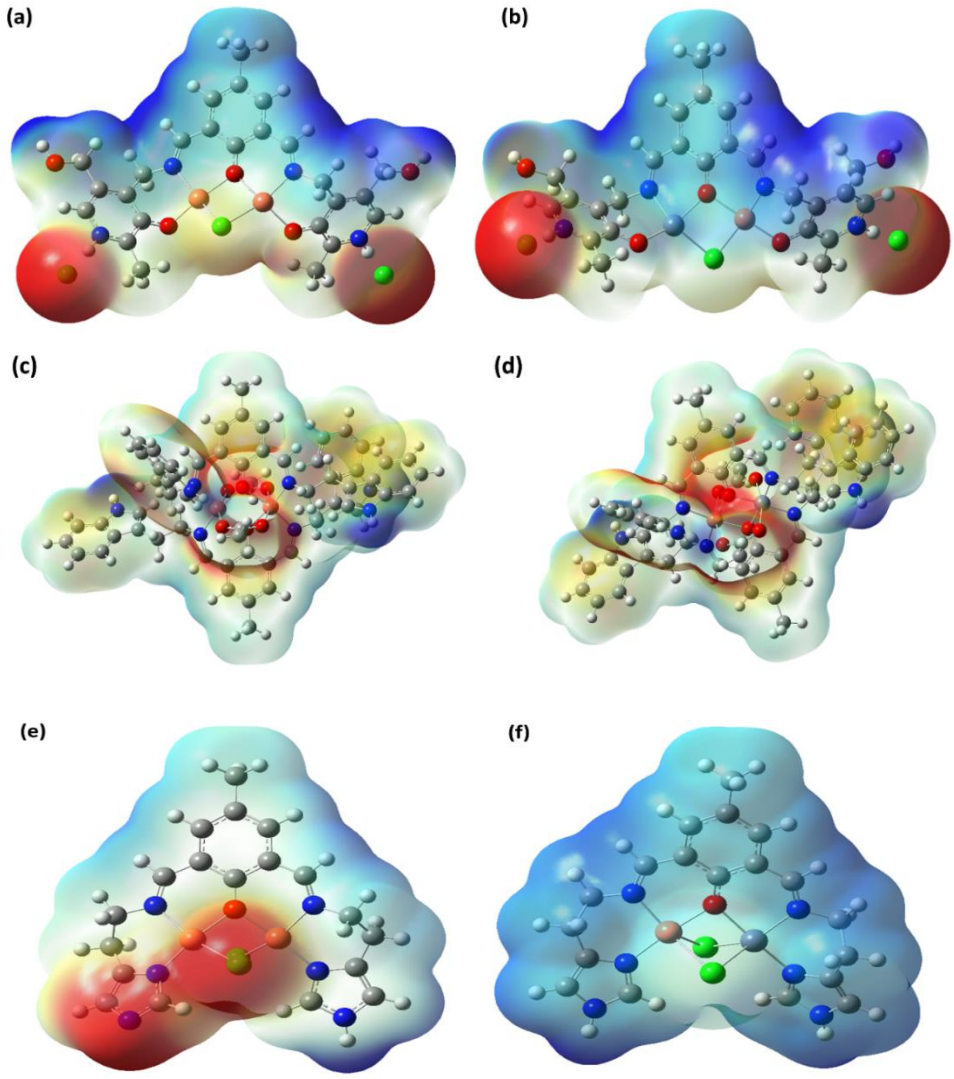

Figure 2.3.2.9.3 *Electrostatic potential of complexes* ***C1-C3***

In all the complexes, HOMO and LUMO along with their two upper and two lower orbitals exhibit different localization indicating intramolecular electron charge transfer within the molecule. The energy gap value (ΔE_g) is directly associated with the stability

and hardness and inversely related to the reactivity and softness of the molecule. A very small energy gap values shows that there is an easy charge transfer within the molecule, which may further increase the biological activity of the complex.

2.3.3. SOD mimic activity

Generation of superoxide anion ($O_2^{\cdot -}$) is responsible for the conversion of NBT to monoformazan complex and its scavenging from the system by synthesized complexes (**scheme 2.2.4.1**) forms the basis of this study. The hydrogen donor NADH reduces PMS. This reduced PMS generates $O_2^{\cdot -}$ from dissolved O_2. NBT gets reduced by $O_2^{\cdot -}$, which results in a linear accumulation of blue formazan with increase in the absorbance at 560nm (**Scheme 2.3.3.1**).

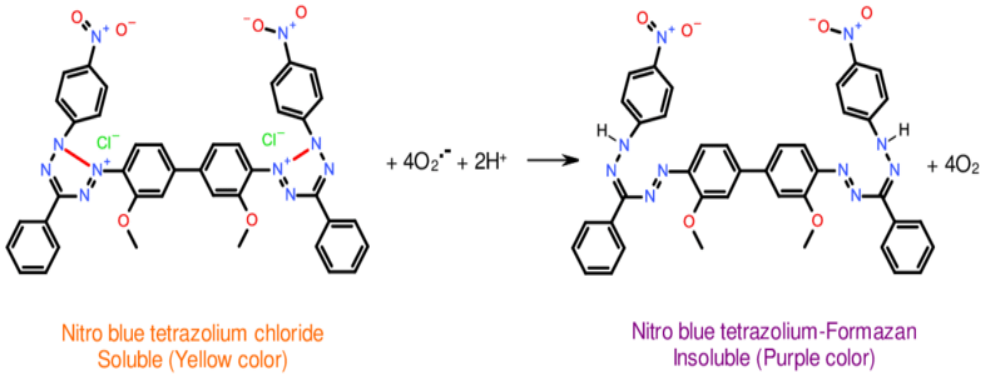

Scheme 2.3.3.1 *Reaction of NBT with $O_2^{\cdot -}$ to form blue formazan*

In the reaction medium, SOD or SOD mimic compounds scavenge $O_2^{\cdot -}$ which results in decrease in the formation of formazan. The % inhibition of NBT reduction at various concentrations of complexes as a function of time was measured by measuring the absorbance at 560nm. **Figure 2.3.3.1** represents the plot of absorbance (A_{560}) against time (t) with varying concentration of complexes required to yield % inhibition of the NBT reduction. The % inhibition values of complexes are higher than exhibited by copper salt.

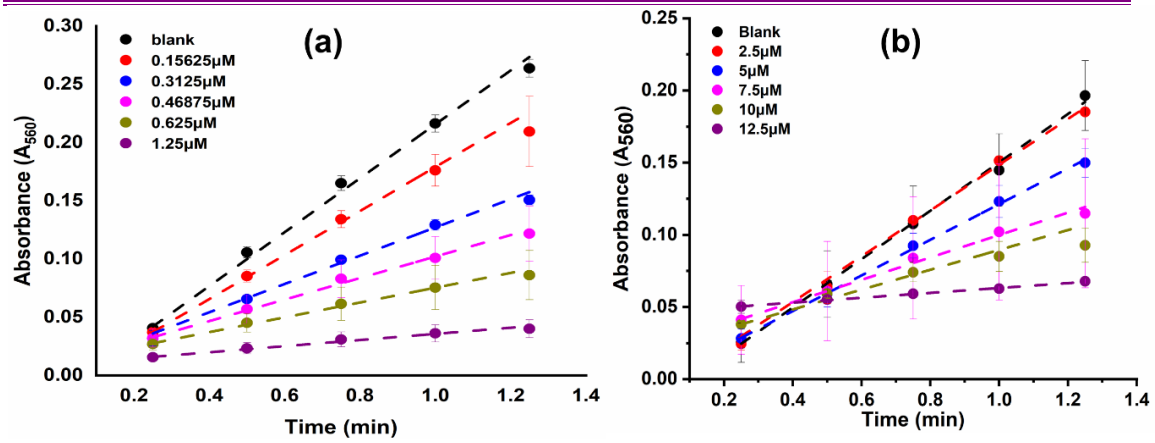

Figure 2.3.3.1 *Plot of Absorbance (A_{560}) as function of time (min) (a)* ***C1a*** *(b)* ***C1b***

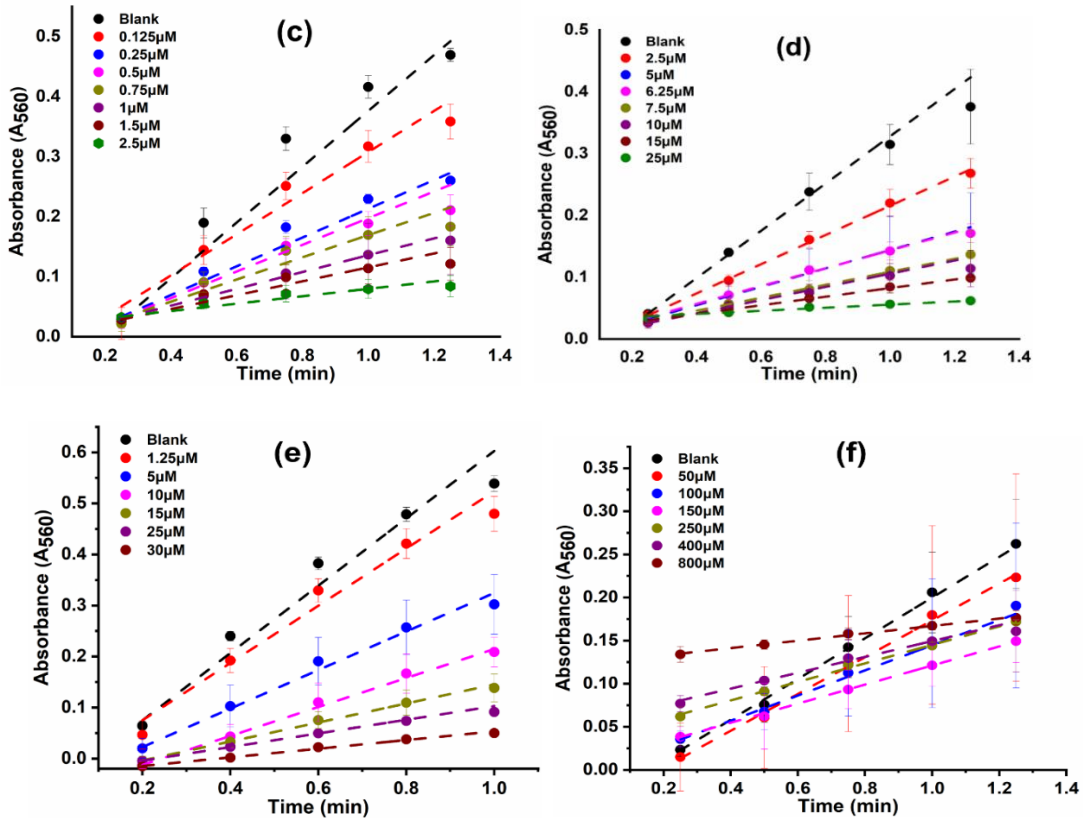

Figure 2.3.3.1 *(Contd…) Plot of Absorbance (A_{560}) as function of time (min) (c)* ***C2a*** *(d)* ***C2b*** *(e)* ***C3a*** *(f)* ***C3b***

Figure 2.3.3.2 represents % inhibition of NBT reduction as a function of increasing concentrations of complexes which yields IC_{50} value of that particular complex.

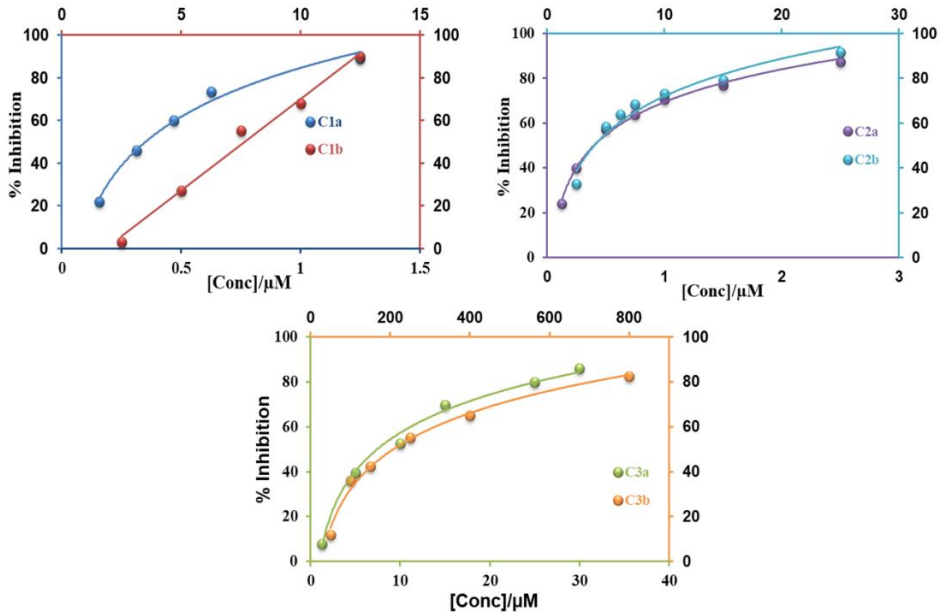

Figure 2.3.3.2 *Plot of % inhibition of NBT reduction vs. concentration of complexes*

The copper(II) complexes showed SOD mimic activity, which was evaluated by the scavenger concentration causing 50% inhibition of reduction of NBT, IC_{50}. The ligands show very low % inhibition at 100μM concentration of ligand. The % inhibition of NBT reduction was found to be 9% and 37% for $\mathbf{L^2}$ and $\mathbf{L^3}$ respectively at that particular concentration. This confirms that ligands $\mathbf{L^2}$ and $\mathbf{L^3}$ do not have good SOD mimicking activity. (**Figure 2.3.3.3**)

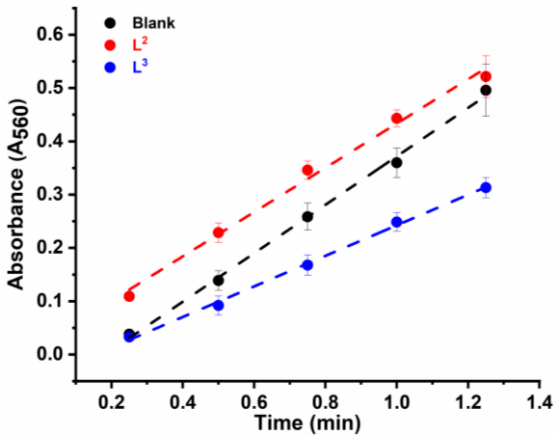

Figure 2.3.3.3 *Plot of Absorbance (A_{560}) as function of time (min) of* $\boldsymbol{L^2}$ *and* $\boldsymbol{L^3}$ *at 100μM concentration*

The complexes under consideration here, exhibit SOD-like activity at the biological pH with IC_{50} values ranging from 0.351-7.45μM for homonuclear copper(II) complexes and 7.66-208.1μM for heteronuclear copper(II) zinc(II) complexes. The complexes have better SOD mimic activity than those reported earlier in the literature[58–62,89,104–

[108]. The catalytic rate constant (k_{cat}) of these complexes was evaluated using the **equation 2.8**.

$$k_{cat} = K_{NBT}[NBT]/IC_{50} \ldots\ldots\ldots\ldots\ldots (2.8)$$

where K_{NBT} = 5.94×10^4 M^{-1}s^{-1} is the second order rate constant for NBT. From the k_{cat} values, it is clear that all complexes can be used as scavengers for superoxide. The results of SOD mimic activity have been summarized in **Table 2.3.3.1**.

The proposed mechanism of the SOD mimic activity of complexes is shown in **scheme 2.2.4.1**. The first step is the electron transfer between the superoxide ($O_2^{\cdot -}$) and the copper(II) centre of the complexes and $O_2^{\cdot -}$ exchanges very fast resulting in the formation of O_2. The second step involves the reoxidation of copper(I) to copper(II) by the second molecule of $O_2^{\cdot -}$ with the generation of H_2O_2 molecule.

Table 2.3.3.1 *IC_{50} values of ligands (**L^2** and **L^3**) and complexes (**C1-C3**) and of native enzyme*

Complexes	IC_{50} (µM)	k_{cat} x 10^4 (M^{-1}s^{-1})
C1a	0.351	1269
C1b	7.66	0.607
L^2	>100	-
C2a	0.396	1125
C2b	4.02	110.8
L^3	>100	-
C3a	7.45	59.798
C3b	208.1	2.141
Native enzyme (SOD)[c 115,116]	0.03-0.15	-
$[Cu_2\mu(SCN)_2L^1_2]$[a 117]	24	13.84
$[Cu(L^2)(NO_3)(\mu$-2-aminopyrazine$)Cu(L^2)(NO_3)_2].2H_2O$[a 118]	15	22.17
$[(L^3)Cu(\mu$-$CH_3COO)_2Cu(L^3)]$[a 119]	35	9.50
[Cu(N-(5-methylthiazol-2-yl)pivalamide)$_2$][b 120]	0.285	1563
$CuCl_2 \cdot 2H_2O$[c 115,116]	0.910	489.56

IC_{50} was determined by a=Alkaline DMSO , b=NADH-PMS-NBT and c= xanthine/xanthine oxidase
L^1 =(Z)-N'-(phenyl(pyridin-2-yl)methylene)acetohydrazide, L^2 = N´-[(E)-phenyl (pyridine-2-yl)methylidene]benzohydrazide, L^3=N'-[phenyl(pyridin-2-yl)methylidene]benzohydrazone)

2.3.4 Ascorbic Acid Oxidase (AAO) activity

The oxidation of AA as catalyzed by complexes using dissolved O_2 as oxidant in presence of acetate buffer (pH 5.5) was monitored by measuring absorbance at λ_{max} = 265nm using UV-Vis spectroscopy. A distinct absorption maximum at λ_{max} = 265nm (marked as 'a') was observed for ascorbic acid (AA) in **figure 2.3.4.1(a)**. However,

when complexes were added to the solution of AA under aerobic conditions, a significant decrease in absorbance (marked as 'b') was noted which demonstrated the fact that AA was consumed in a reaction (**figure 2.3.4.1(a)**).

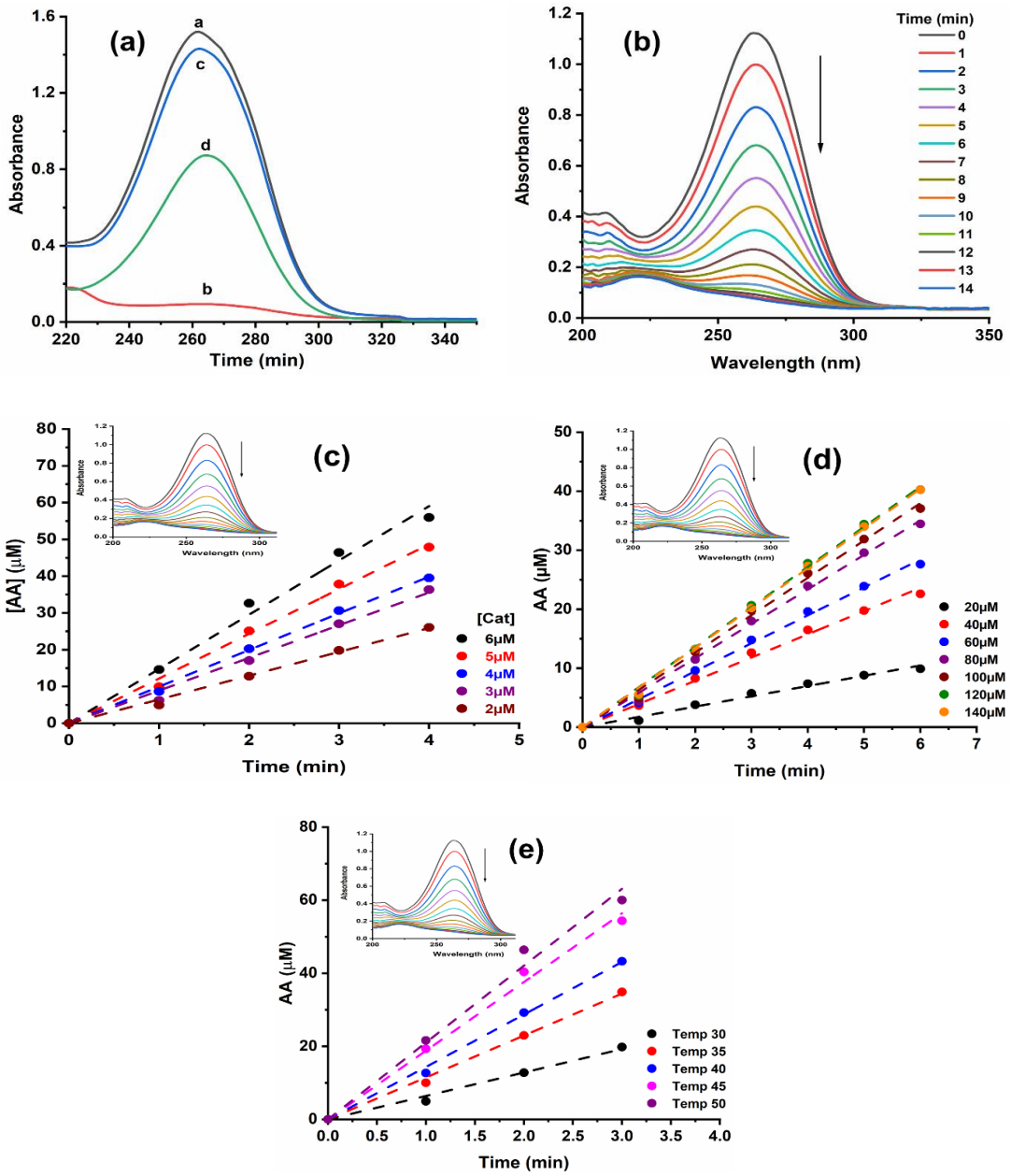

Figure 2.3.4.1*(a) Uv-Vis spectra of a: AA b: AA+**C1a** under aerobic condition c: AA+**C1a** under a N_2 atm. for 20 mins and d: AA+$Cu(OAc)_2$ for 20 mins under aerobic condition, (b) Time dependent spectral changes from 0 to 14 mins of AA corresponding to **C1a** catalyzed oxidation and*

(c-e) Plot of [AA] as function of time with respect to catalyst (c), substrate (d) and temperature (e) (Inset: Plot of absorbance vs wavelength at different time intervals)

But when same experiment was carried out under nitrogen atmosphere, there was no significant decrease in the absorbance at λ_{max} = 265nm (marked as 'c') which confirms the involvement of O_2 in the reaction (**figure 2.3.4.1(a)**).

A similar experiment was carried out in presence of corresponding copper salts, there was a significant decrease in the absorbance at λ_{max} = 265nm (marked as 'd'). However, the reaction was stoichiometric and not catalytic (**figure 2.3.4.1(a)**). The time dependent (0-40 mins) changes in the absorption spectra upon oxidation of AA by O_2 in the presence of complexes was depicted in **figure 2.3.4.1(b)** for complex **C1a** and for other complexes (see **SI†: Fig. S2.10(a,e,i,m,q)**). The absorbance band at λ_{max} = 265nm decreases with time from 0 min to 40 min and completely disappears after 40 min which confirms that complexes quickly catalyze the oxidation of AA to DHAA.

Rate of reaction for all complexes was obtained by initial rate method by plotting [AA] as function of time by using ε = 14500 $dm^3mol^{-1}cm^{-1}$. **Figure 2.3.4.1(c-e)** shows plot of [AA] as function of time for complex **C1a** and for other complexes (see **SI†: Fig. S2.10(b-d,f-h,j-l,n-p,r-t)**).

To obtain the steady-state kinetic parameters, we further studied the catalytic behavior of complexes with AA as substrate, built on enzyme kinetics theory and methods. The most commonly and widely used models and methods to study the enzymatic reaction was Michaelis-Menten model.

In **figure 2.3.4.2**, the solid circles are experimental data and the solid curves fit the Michaelis-Menten model for all complexes. With various concentrations of ascorbic acid (AA), Michaelis-Menten constant (K_m) can be obtained from the following Michaelis Menten equation (**equation 2.9**).

$$\boldsymbol{\upsilon = \frac{V_{max}\,[S]}{K_m + [S]}} \ldots\ldots\ldots\ldots\ldots\ldots (\mathbf{2.9})$$

where υ= rate of reaction, V_{max} = maximum rate achieved by the system, [S] = substrate concentration and K_m = Michaelis constant.

The Michealis-Menten constant (K_m)and maximum rate (V_{max}) can be calculated by Lineweaver-Burk plot. By the help of parameters K_m and catalytic rate (k_{cat}), the kinetic of the enzymatic reactions can be characterized.

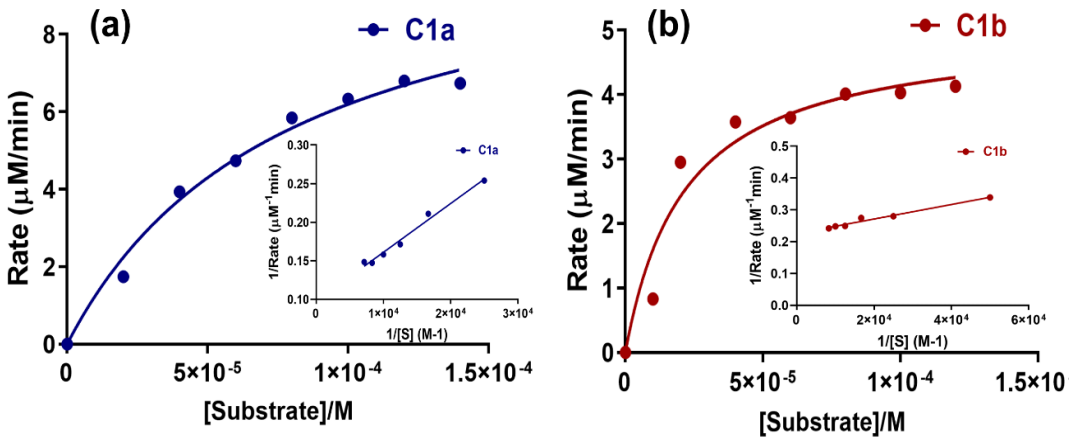

Figure 2.3.4.2 *Rate vs [substrate] plot of Michaelis menten model for complexes (a)* ***C1a*** *(b)* ***C1b*** *(Inset: Lineweaver Burk plot of respective complexes)*

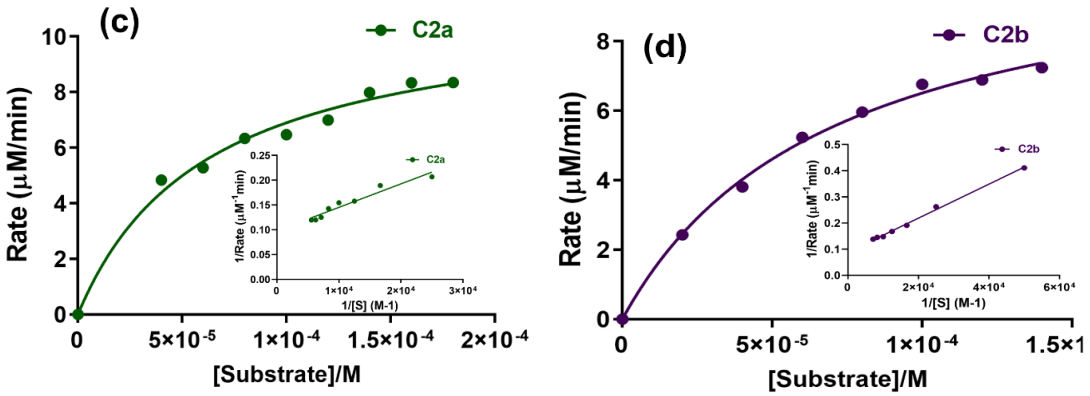

Figure 2.3.4.2 *(Contd…) Rate vs [substrate] plot of Michaelis menten model for complexes c)* ***C2a*** *(d)* ***C2b*** *(Inset: Lineweaver Burk plot of respective complexes)*

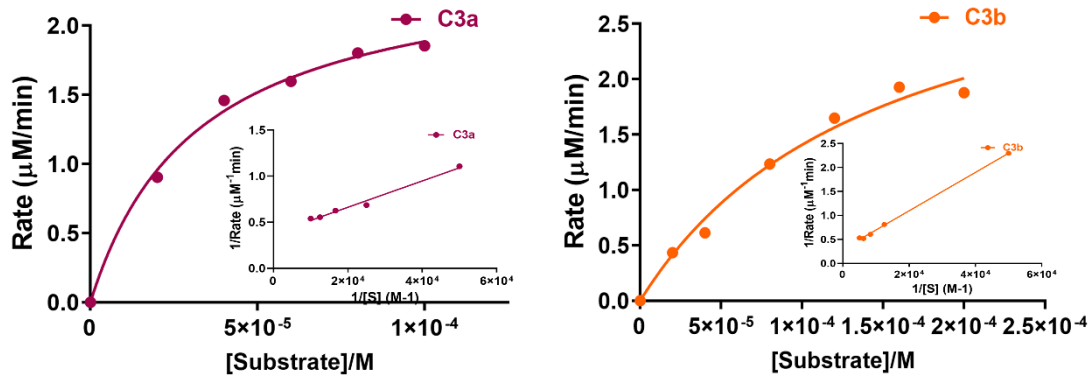

Figure 2.3.4.2 *(Contd…) Rate vs [substrate] plot of Michaelis menten model for complexes (e)* ***C3a*** *and (f)* ***C3b*** *(Inset: Lineweaver Burk plot of respective complexes)*

The order of reaction with respect to the substrate was obtained from slope of the plot of log(rate) as function of log[substrate] (**figure 2.3.4.3**). While order with respect to catalyst was obtained from slope of the plot of log(rate) as function of log[catalyst] (**figure 2.3.4.4**). The order of the reaction was found to be half order with respect to substrate as well as catalyst.

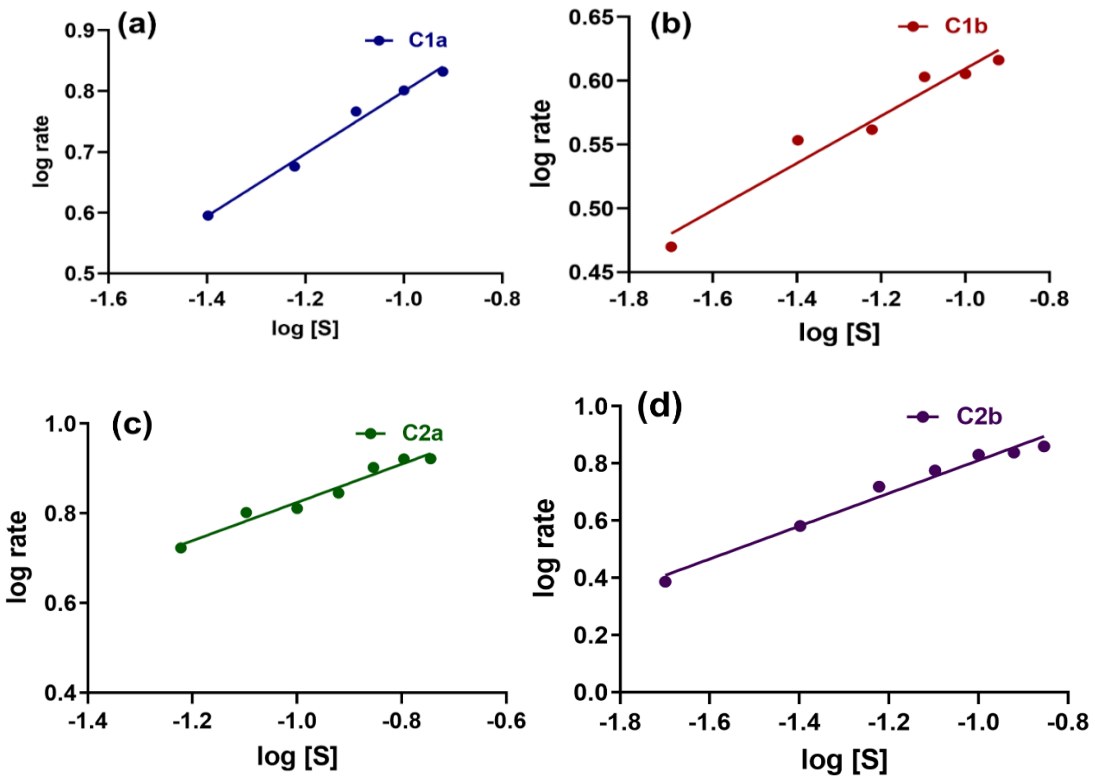

Figure 2.3.4.3 *Plot of log(rate) vs log[S] for complexes (a)* ***C1a*** *(b)* ***C1b*** *(c)* ***C2a*** *(d)* ***C2b***

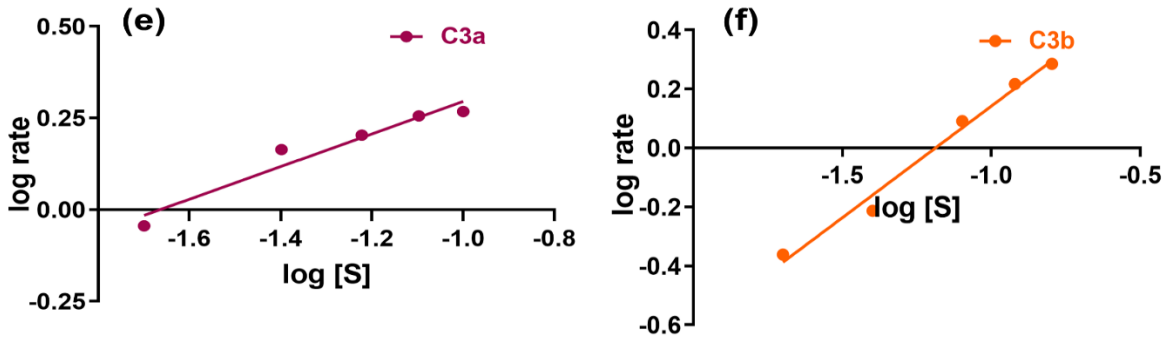

Figure 2.3.4.3 *(Contd…) Plot of log(rate) vs log[S] for complexes (a)* ***C1a*** *(b)* ***C1b*** *(c)* ***C2a*** *(d)* ***C2b*** *(e)* ***C3a*** *and (f)* ***C3b***

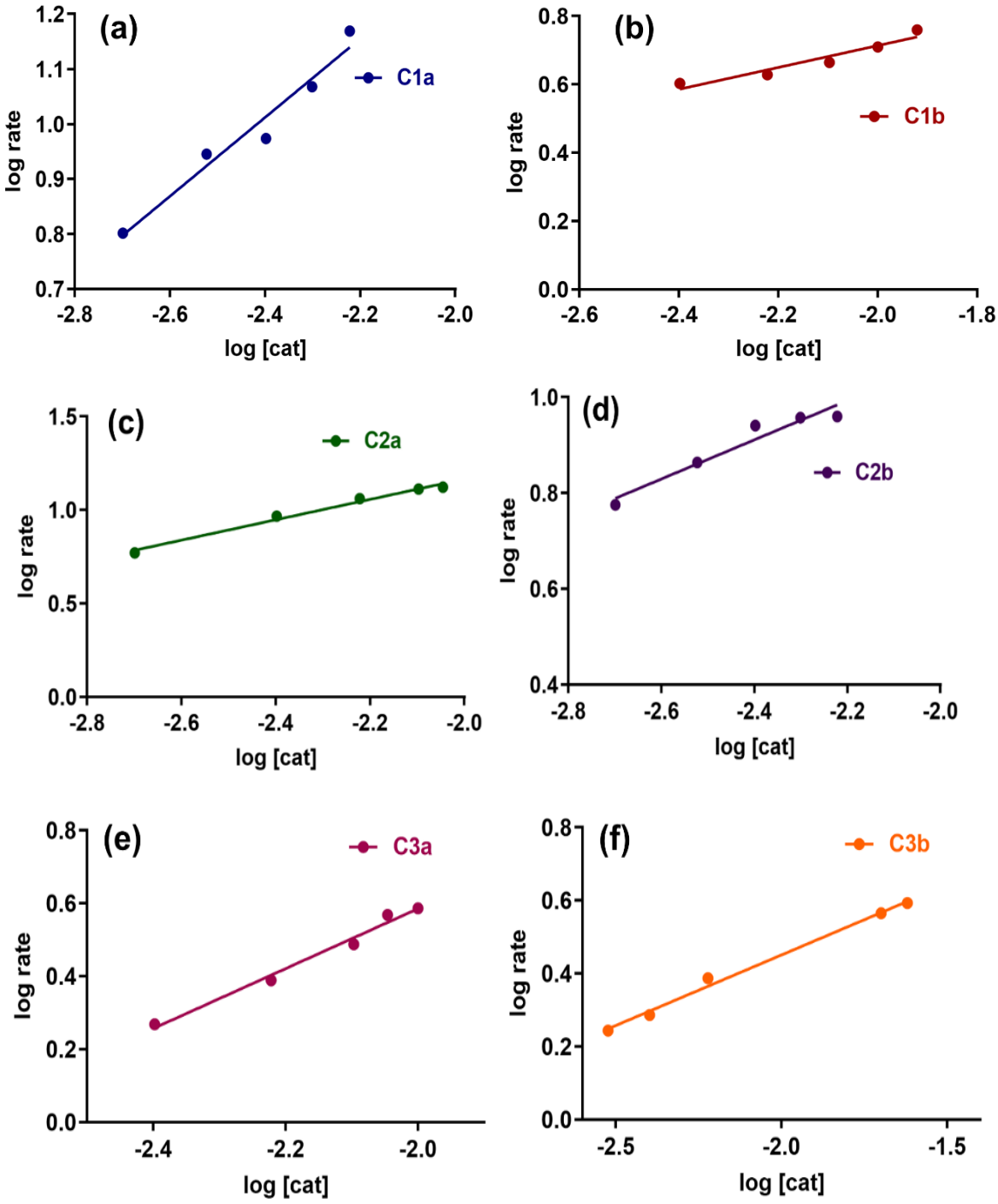

Figure 2.3.4.4 *Plot of log(rate) vs log [Cat] for complexes (a)* ***C1a*** *(b)* ***C1b*** *(c)* ***C2a*** *(d)* ***C2b*** *(e)* ***C3a*** *and (f)* ***C3b***

Activation energy of the reaction was found from the Arrhenius plot (**figure 2.3.4.5**). The kinetic parameters of AA in the presence of complexes, order and activation energy have been summarized in **Table 2.3.4.1**.

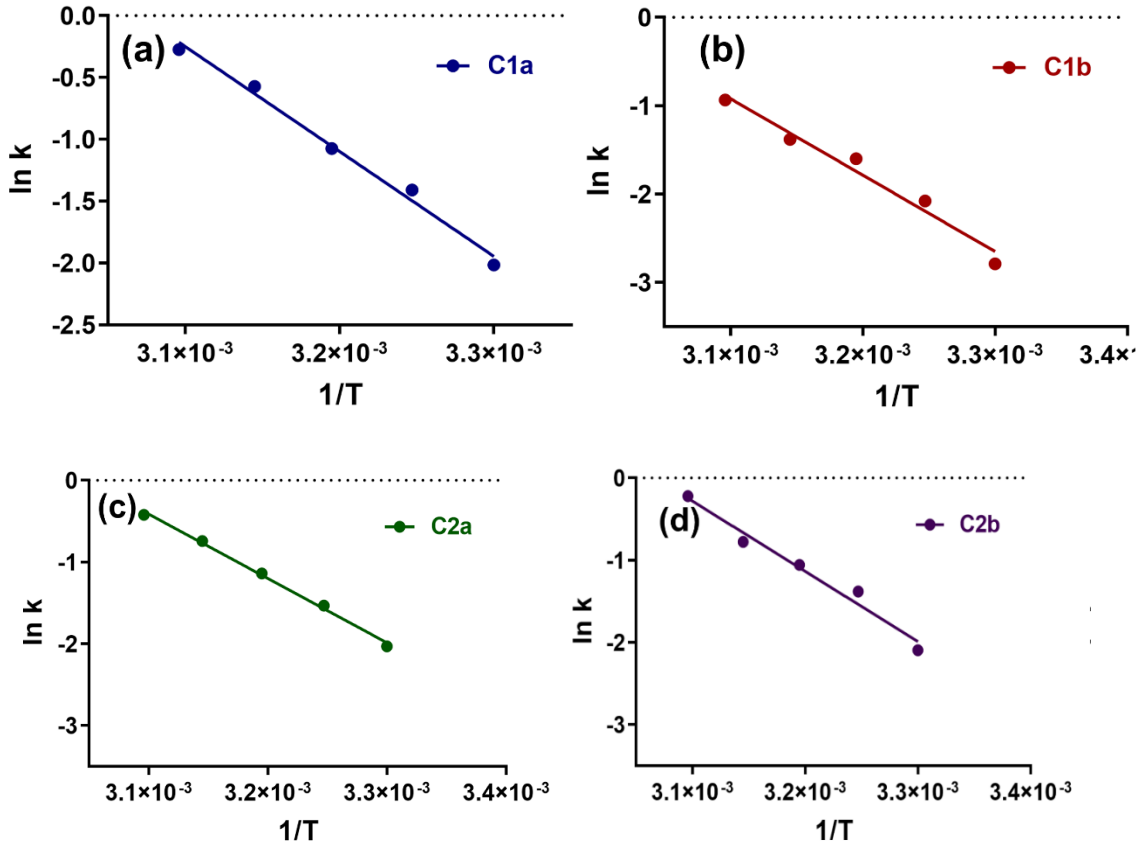

Figure 2.3.4.5 *Arrhenius plot of all complexes (a)* ***C1a*** *(b)* ***C1b*** *(c)* ***C2a*** *(d)* ***C2b***

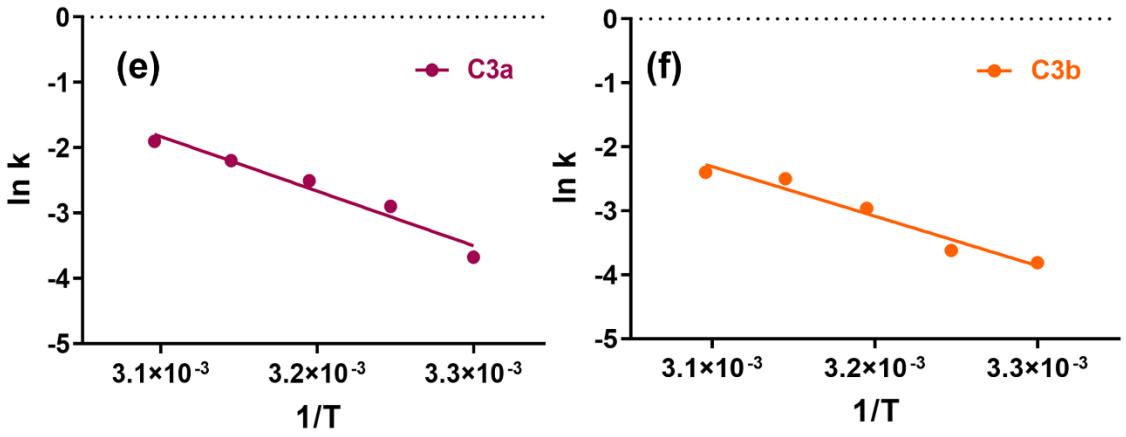

Figure 2.3.4.5 *(Contd…) Arrhenius plot of all complexes (e)* ***C3a*** *and (f)* ***C3b***

The results confirm that the complexes possess good ascorbic acid oxidase mimetic activity that can catalyze the oxidation of AA to DHAA in the presence of O_2 and their activity is better as compared to that of the other complexes reported in the literature[66–68].

Table 2.3.4.1 *Kinetic parameters of AA in presence of complexes (**C1-C3**)*

Complex	K_m (M)	V_{max} (µM/min)	[E] (M)	k_{cat}/h^{-1}	Order		E_a (kJ/mole)
					Cat	Sub	
C1a	11.08	7.89×10^{-5}	2×10^{-6}	332	0.716	0.513	70.4
C1b	5.035	2.16×10^{-5}	4×10^{-6}	75.5	0.32	0.20	71.835
C2a	11.16	6.19×10^{-5}	2×10^{-6}	334.9	0.43	0.545	65.39
C2b	11.07	7.02×10^{-5}	2×10^{-6}	332	0.41	0.574	70.97
C3a	2.49	3.2×10^{-5}	4×10^{-6}	37.3	0.82	0.450	77.58
C3b	3.38	1.35×10^{-4}	4×10^{-6}	50.7	0.39	0.704	78.38
AAO[67]	0.08 (mM)	6.5 (10^4 mM/s)	0.179×10^{-8}	97000	-	-	-
Copper Salt	-	-	-	-	-	-	89.085
No complex	-	-	-	-	-	-	138.99

The presence of any superoxide formed during the reaction was checked spectroscopically and it was found to be absent. The presence of peroxide has also been analyzed spectrophotometrically, using the following method.

Detection of H_2O_2 spectrophotometrically:

The mechanistic pathways of ascorbic acid oxidation involve production of water or hydrogen peroxide. In order to confirm the formation of hydrogen peroxide the reaction mixture was analyzed using a literature procedure[121–123]. The formation of H_2O_2 during the catalytic reaction was detected by following the development of the characteristic band of I_3^- spectrophotometrically (λ_{max}= 353 nm; ε= 26000 $M^{-1}cm^{-1}$), upon reaction with I^-.[1,2] The oxidation reactions of ascorbic acid in the presence of different complexes were carried out in kinetic experiments ([Complex]= 2.0×10^{-5} M and [AA] = 2.4×10^{-2} M). After 1 h of reaction an equal volume of water was added and the quinone formed was extracted three times with dichloromethane. The aqueous layer was acidified with H_2SO_4 to pH= 2 to stop the further oxidation, and 1ml of 10 % KI solution and three drops of 3 % ammonium molybdate solution were added. In the presence of hydrogen peroxide iodide gets oxidized to iodine as per the reaction, $H_2O_2 + I^- + 2H^+ \rightarrow 2H_2O + I_2$, and with an excess of iodide ions, the triiodide ion is formed according to the reaction, $I_{2(aq)} + I^- \rightarrow I^-_3$. The reaction rate is slow but increases with

increasing concentrations of acid, and the addition of ammonium molybdate solution renders the reaction almost instantaneously. The formation of I_3^- could be monitored spectrophotometrically due to the development of the characteristic I_3^-band (λ_{max}= 353 nm; ε= 26000 $M^{-1}cm^{-1}$).[3] In order to prove that I_3^- results from the presence of H_2O_2, control experiments were performed using only H_2O_2 solution. Since atmospheric oxygen can also oxidise I^- , blank experiments without catalyst or ascorbic acid were also performed (See **SI†: Fig. S.2.14**).

As the reaction has partial order with respect to both, the substrate and the catalyst, utilizes molecular oxygen as oxidant and the radical formation is absent, the following mechanism (**Figure 2.3.4.6**) can be suggested for the reaction, wherein one ascorbic acid substrate binds per dicopper(II) unit to transfer two electrons to each copper(II) ion and gets oxidized to the corresponding DHAA. The reduced dicopper(I) species then binds with molecular oxygen and gets oxidized to regenerate the original catalytic species. One molecule of oxygen is consumed and one substrate molecule is oxidized per catalytic cycle. Nonetheless, the peroxide so generated by dioxygen reduction can also participate in the reaction as oxidizing agent, its mode of binding is expected to be similar to that of dioxygen but the number of electrons transferred and the number of catalyst and substrate species reacting per cycle will remain the same. Thus, molecular oxygen in the initial stages and both O_2 and O_2^{2-} can be participating as oxidants in the subsequent stages of the reaction. The presence of peroxide has also been analyzed spectrophotometrically as detailed above.

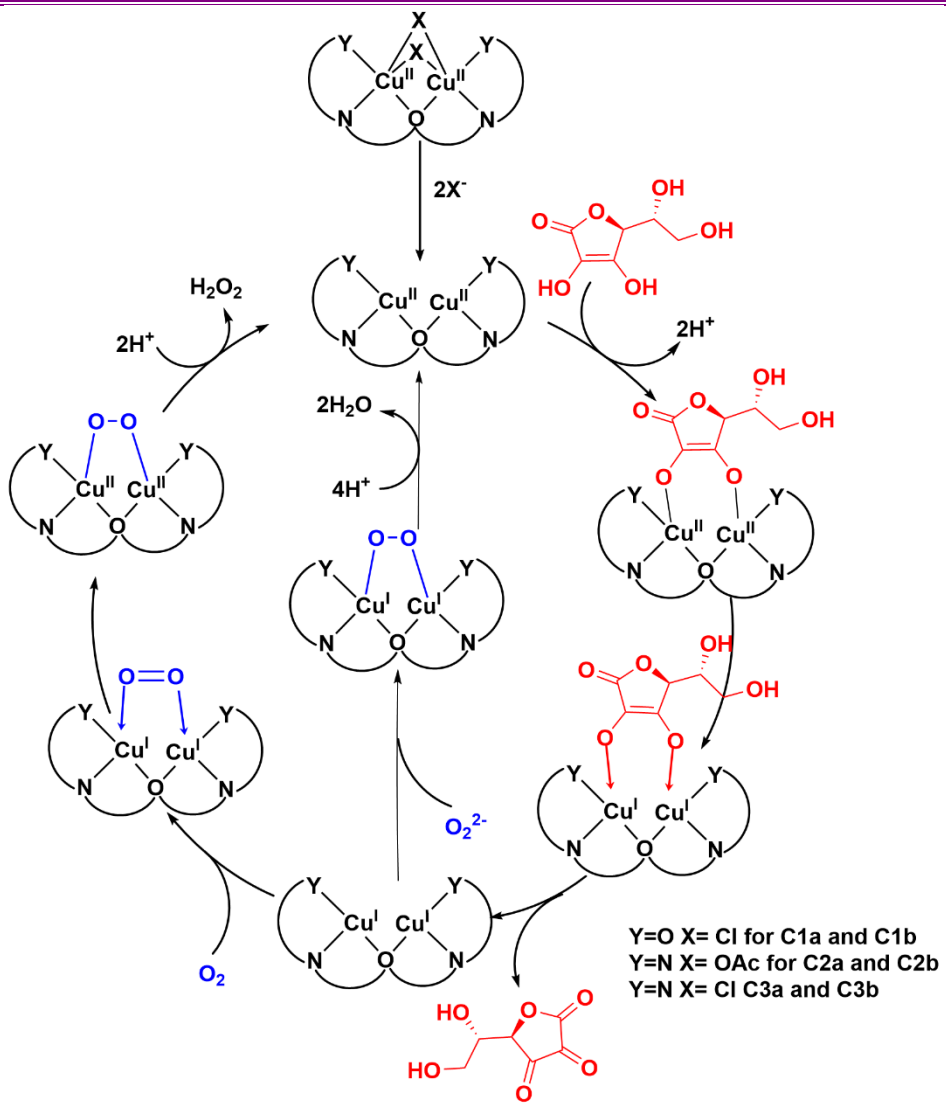

Figure 2.3.4.6 *Possible proposed mechanism of ascorbic acid oxidase activity of ascorbic acid as substrate for all complexes*

2.3.5 Catecholase mimic activity

The studies reported so far on the synthetic tyrosinase and catecholase models typically employ 3,5-DTBC because of its low reduction potential[51,104]. However, there is a lack of literature on the use of other diphenols as substrate and a comparison on the catalytic efficacy of the models with respect to the variations in the nature, electronic character and stereochemistry of the substrates.

In the present study, five substrates, 3,5-DTBC, 4-methyl catechol, dopamine, pyrocatechol and 2,3-dihydroxy naphthalene have been employed to study the catecholase activity of all homonuclear and heteronuclear complexes. The reaction with pyrocatechol, dopamine and 2,3-dihydroxy naphthalene was found to be very slow. The

corresponding quinone band in dopamine, pyro- catechol and 2,3-dihydroxy naphthalene had negligible appearance even after 24 hrs of reaction time indicating negligible catalytic activity of the complex for these three substrates. The reactions in presence of complexes **C1a** and **C1b** was found to be very slow. The corresponding quinone band in both 3,5-DTBC and 4-MC had negligible appearance after 24 hrs of reaction time indicating negligible catalytic activity of these complexes for these two substrates. Complexes **C2a-C2b** and **C3a-C3b** were found to be active for both substrates. Hence, detailed kinetic studies have been carried out with 3,5-DTBC and 4-methylcatechol. Methanolic solutions have been employed to suit the solubility of reactants and products. The products, 3,5-di-*tert*-butyl-o-quinone (3,5-DTBQ) and 4-methylquinone (4-MQ) have strong absorbance band at λ_{max} = 390 – 400 nm (ε =1900 $dm^3mol^{-1}cm^{-1}$) and λ_{max} = 380 – 400 nm (ε =2140 $dm^3mol^{-1}cm^{-1}$) and also they are stable. Hence, the activities and reaction rates, respectively, of model complexes can be determined by following the appearance of absorption maximum of the quinone in the electronic spectra. In order to find the capability of complexes to act as an oxidation catalyst, it was subjected to catecholase mimetic activity (**Scheme 2.3.5.1**) for oxidation of 3,5-DTBC to 3,5-DTBQ and of 4-methyl catechol to 4-methylbenzoquinone.

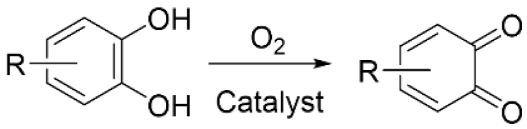

Scheme 2.3.5.1 *Reaction involved in the oxidation of o-diphenols*

The course of a typical reaction has been followed with solution of complex C2a (**Figure 2.3.5.1.(a)**) for 3,5-DTBC and with other complexes for both substrates (see **SI† in Fig 2.11** and **2.12** inset graph). The substrate 3,5-DTBC / 4-methyl catechol was added at once to the solution of the complex and the spectra were recorded. The MLCT bands in the complex disappeared and a new band corresponding to 3,5-DTBQ / 4-methyl quinone started appearing at 380–410 nm.

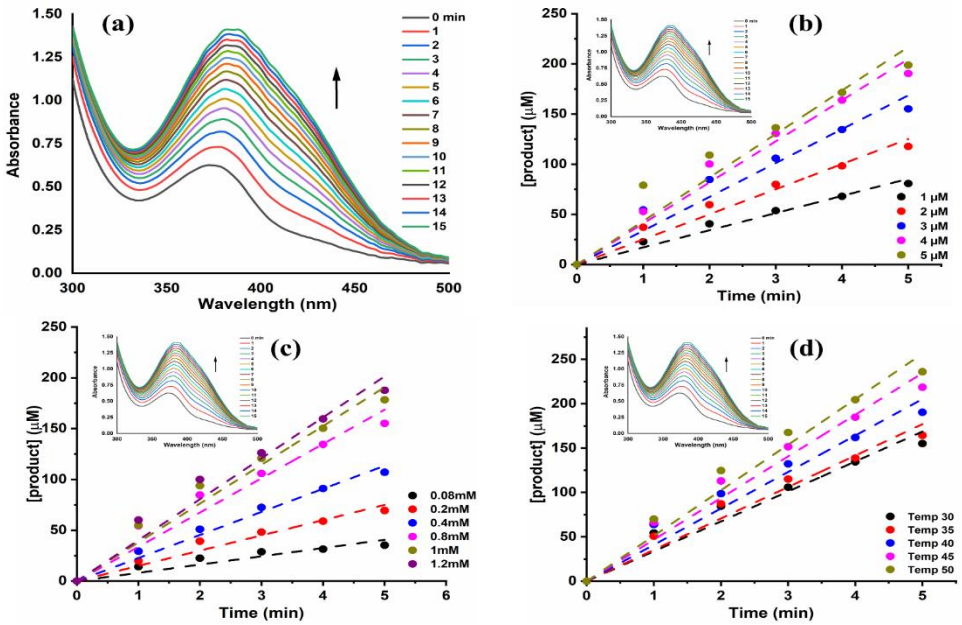

Figure 2.3.5.1*(a) Time dependent spectral changes from 0 to 14 mins of 3,5-DTBC corresponding to* ***C2a*** *catalyzed oxidation and (b-d) Plot of [product] as function of time with respect to catalyst (b), substrate (c) and temperature (d) (Inset: Plot of absorbance vs wavelength at different time interval*

A linear increase in the absorption of this band was observed. The kinetics of oxidation of 3,5-DTBC and 4-methyl catechol was determined by the method of initial rates by monitoring the enhancement of 390–410 nm band of 3,5-DTBQ and 4-methyl quinone as a function of time. Complex **C1a** and **C1b-C3b** showed negligible catecholase activity with 3,5-DTBC and 4-MC, as substrate. There was no appearance of quinone band after 24 h. This shows the selectivity of the substrate with catalyst. Rate of reaction for all complexes was obtained by initial rate method by plot of [product] as function of time. **Figure 2.3.5.1.(b-d)** shows plot of [product] as function of time for complex **C2a** for 3,5-DTBC, for 4-MC (see **SI†: Fig. S2.11.(a-d)**) and for **C3a** complex with both substrates (see **SI†: Fig. S2.12.(a-e)**). Plot of [product] *vs* time for the oxidation of 3,5-DTBC at various temperatures is depicted in **Figure 2.3.5.2.(a)**. The plots of [product] *vs* time are linear and have been used to calculate the rates of the catalysed reaction under different conditions.

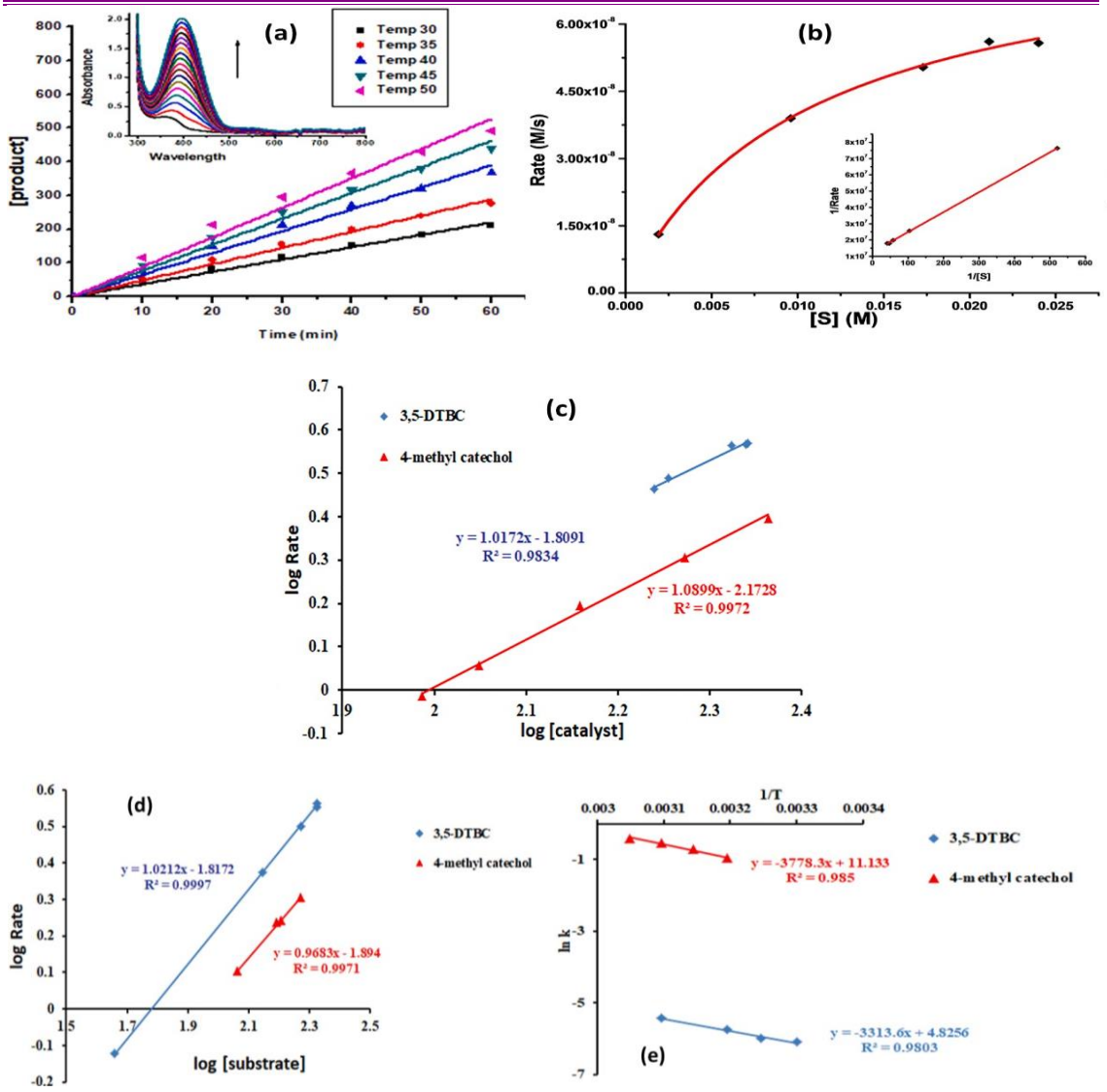

Figure 2.3.5.2 *(a) Plot of [product] vs time of 3,5-DTBC at various temperatures (Inset: Plot of absorbance vs wavelength at 40 °C;*

(b) plot of rate vs [substrate] with 3,5-DTBC as substrate for complex ***C3a****,(Inset: Lineweaver-Burk plot); (c) plot of log rate vs log [catalyst], the blue coloured diamonds represent 3,5-DTBC substrate and red coloured closed diamonds represent 4-methyl catechol;*

(d) plot of log rate versus log [substrate], blue-coloured diamonds represent 3,5-DTBC substrate and red colour closed diamonds represent 4-methyl catechol,

(e) Arrhenius plot for 3,5-DTBC (blue diamonds) and 4-methyl catechol (red triangles)

The analysis of the data based on the Michaelis- Menten model, originally developed for enzyme kinetics, was applied. In **figure 2.3.5.2 (b)**, **figure 2.3.5.3** and **figure 2.3.5.4 (a)**, the solid circles are experimental data and the solid curves are the fits to the Michaelis-Menten model for all complexes. With various concentrations of substrates, Michaelis-Menten constant (K_m) can be obtained from the Michaelis Menten equation. The observed rate versus [substrate] plot and the Lineweaver-Burk plot for complex **C3a** with 3,5-DTBC and for 4-MC are depicted in **Figure 2.3.5.2 (b)** and **Figure 2.3.5.3**, respectively.

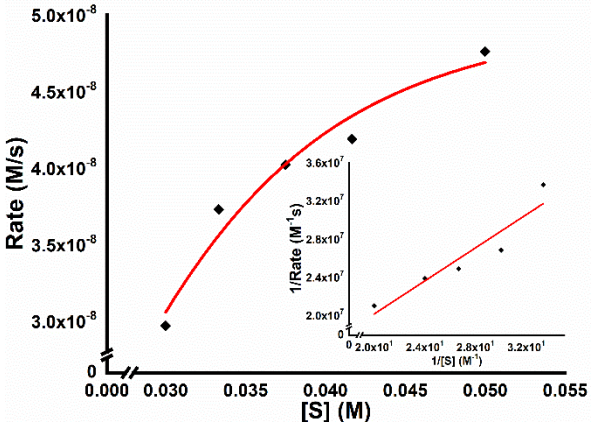

Figure 2.3.5.3 *Plot of rate vs [Substrate] of Michaelis Menten Model of complex* ***C3a*** *for 4-MC as substrate (Inset: Lineweaver Burk plot of complex* ***C3a****)*

The plots of log (rate) versus log[catalyst] (**Figure 2.3.5.2.(c)**) and log (rate) versus log[substrate] (**Figure 2.3.5.2.(d)**) indicate that the complex catalyzed oxidation of both diphenols to the corresponding quinones follow first order kinetics with respect to the substrate and also with respect to the dicopper(II) monomer of the complex **C3a**. The activation energy values for the oxidation of 3,5-DTBC and 4-methyl catechol in presence of all synthesized complexes as catalyst have been calculated from Arrhenius plot (**Figure 2.3.5.2.(e)** for complex **C3a**). The low activation energy values indicate that the complexes are efficient oxidation catalysts. The order of reaction with respect to the substrate was obtained from slope of the plot of log(rate) as function of log[substrate] (**figure 2.3.5.4.(c)**) while order with respect to catalyst was obtained from slope of the plot of log(rate) as function of log[catalyst] (**figure 2.3.5.4.(b)**) for complex **C2a**.

Table 2.3.5.1 *Kinetic parameters of Michaelis Menten model, Order, Activation energy of substrates with complexes (**C1-C3**)*

Complexes	Substrate	V_{max} (M/s)	Km (M)	K_{cat} (h^{-1})	Order		Ea (kJ/mole)
					Cat	Sub	
C1a	3,5-DTBC	Very Slow					
	4-MC	Very Slow					
C1b	3,5-DTBC	Very Slow					
	4-MC	Very Slow					
C2a	3,5-DTBC	1.02×10^{-8}	6.34×10^{-4}	62.4	0.6042	0.593	24.26
	4-MC	4.09×10^{-8}	2.24×10^{-3}	3.86	0.4056	0.4544	30.77
C2b	3,5-DTBC	Very Slow					
	4-MC	Very Slow					
C3a	3,5-DTBC	9.55×10^{-8}	0.013	17.2	1.0712	1.0212	27.55
	4-MC	2.48×10^{-7}	0.285	10.7	1.0899	0.9683	31.41
C3b	3,5-DTBC	Very Slow					
	4-MC	Very Slow					

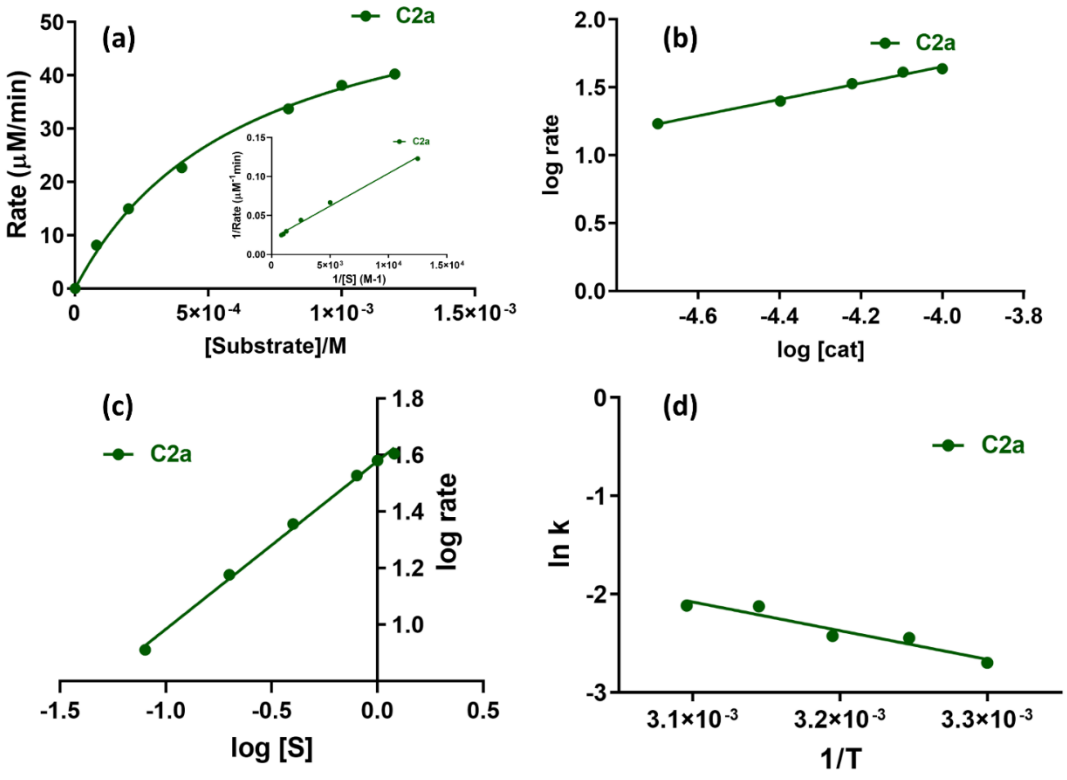

Figure 2.3.5.4 *(a) Plot of Rate vs [Substrate]of Michaelis Menten model for complex **C2a** (Inset: Lineweaver Burk plot); (b) Plot of log(rate) vs log[cat] for complex **C2a**; (c) Plot of log(rate) vs log[S] for complex* C2a *and (d) Arrhenius plot for complex **C2a***

Activation energy of the reaction was found from the Arrhenius plot (**figure 2.3.5.4.(d)**) for complex C2a with 3,5-DTBC and 4-MC as substrates (see **SI†: Fig. S2.13.(a-d)**). The kinetic parameters, order with respect to the catalyst & substrate and activation energy are summarized in **table 2.3.5.1**.

The presence of any superoxide formed during the reaction was checked spectroscopically and it was found to be absent. As the reaction is first order with respect to both, the substrate and the catalyst, utilizes molecular oxygen as oxidant and the radical formation is absent, the following mechanism (**Figure 2.3.5.5**) can be suggested for the reaction, wherein one o-diphenol substrate binds per dicopper(II) unit to transfer two electrons to each copper(II) ion and gets oxidised to the corresponding quinone. The reduced dicopper(I) species then binds with molecular oxygen and gets oxidised to regenerate the original catalytic species. One molecule of oxygen is consumed and one substrate molecule is oxidised per catalytic cycle.

Nonetheless, the so generated by dioxygen reduction during oxidation of o-diphenols, can also participate in the reaction as oxidizing agent, its mode of binding is expected to be similar to that of dioxygen but the number of electrons transferred and the number of catalyst and substrate species reacting per cycle will remain the same. Thus, molecular oxygen in the initial stages and both O_2 and O_2^{2-} can be participating as oxidants in the subsequent stages of the reaction. The presence of peroxide has also been analysed spectrophotometrically. It was found to be present in case of 4-methyl catechol as substrate unlike 3,5-DTBC where it could not be detected, confirming that it is completely consumed during the reaction in the latter case.

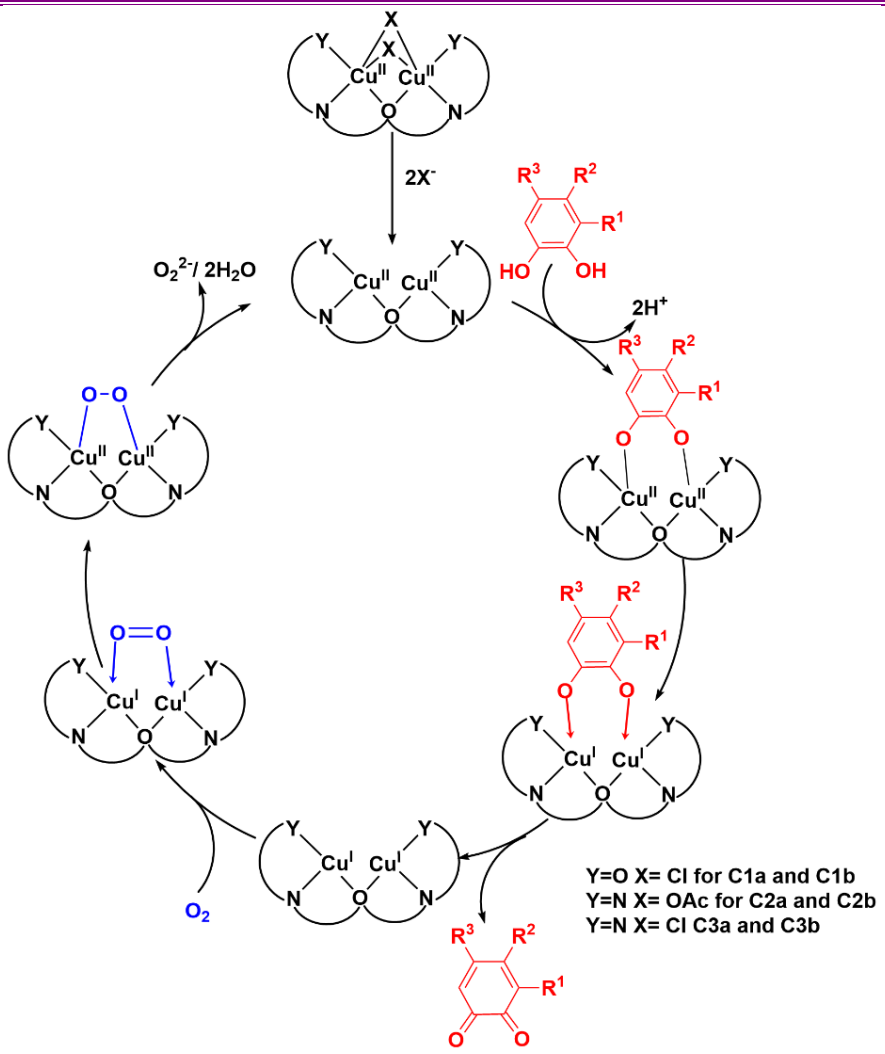

Figure 2.3.5.5 *Possible proposed mechanism of catecholase activity with 3,5-DTBC and 4-MC as substrate for complex* ***C2a*** *and* ***C3a***

In order to confirm the formation of peroxide, the following experiments have been performed using literature procedure[121–123].

Spectrophotometric Detection of H_2O_2:

The mechanistic pathways of catechol oxidation may involve production of water or hydrogen peroxide. The formation of H_2O_2 during the catalytic reaction was detected by following the development of the characteristic band of I_3^- , spectrophotometrically (λ_{max}= 353 nm; ε= 26000 $M^{-1}cm^{-1}$), upon reaction with I^-.[121,123] The oxidation reactions of 3,5-DTBC and 4-MC in the presence of complexes C2a and C3a were carried out in kinetic experiments ([C2a]= 2.0 x 10^{-5} M , [3,5-DTBC] = 2.4 x 10^{-2} ; [C3a]= 2.0 x 10^{-5} M, [3,5-DTBC] = 2.4 x 10^{-2} M; [C2a]= 10 x 10^{-5} M, [4-MC]= 2.5 x 10^{-2} M and [C3a]= 10 x 10^{-5} M, [4-MC]= 2.5 x 10^{-2} M). After 1 h of reaction an equal volume of water

was added and the quinone formed was extracted three times with dichloromethane. The aqueous layer was acidified with H_2SO_4 to pH= 2 to stop the further oxidation, and 1ml of 10 % KI solution and three drops of 3 % ammonium molybdate solution were added. In the presence of hydrogen peroxide, iodide gets oxidized to iodine, $H_2O_2 + I^- + 2H^+ \rightarrow 2H_2O + I_2$, and with an excess of iodide ions, the triiodide ion is formed according to the reaction $I_{2(aq)} + I^- \rightarrow I_3^-$. The reaction rate is slow but increases with increasing concentrations of acid, and the addition of ammonium molybdate solution renders the reaction almost instantaneously. The formation of I_3^- was monitored spectrophotometrically by the development of the characteristic I_3^- band (λ_{max}= 353 nm; ε= 26000 $M^{-1}cm^{-1}$).[3] In order to prove that I_3^- results from the presence of H_2O_2, control experiments were performed using only H_2O_2 solution. Since atmospheric oxygen can also oxidise I^- blank experiments without catalyst or DTBC / 4-MC were also performed (See SI†: Fig. S2.14.). When 4-methyl catechol was used as substrate, dioxygen was converted to hydrogen peroxide which is evident from the UV-Vis spectral study of solution where as in case of 3,5-DTBC, dioxygen was converted to water and the peroxide could not be detected.

2.4 Conclusion

- The homonuclear $Cu^{II}Cu^{II}$ and heteronuclear $Cu^{II}Zn^{II}$ complexes were synthesized by using copper and Zinc acetate and Schiff bases formed by condensation of biogenic amines with 2,6-diformyl-4-methylphenol.
- All synthesized ligands and complexes were spectrophotometrically characterized.
- The complex **C3a** crystallizes as a dimeric unit with the Cu⋯Cu separation within 2.9-3.2Å in complex **C3a**. This distance is in a similar range for all complexes which facilitates binding with diphenol and ascorbic acid substrates as well as molecular oxygen.
- The moderate spin exchange also indicates electron delocalization, facilitates dioxygen activation and catalytic substrate oxidation.
- Quantum chemical calculations were carried out to investigate reactivity parameters.
- All homonuclear copper complexes exhibit better ascorbate activity than that of heteronuclear copper zinc complexes.
- The complexes **C1a** and **C1b-C3b** were found to be very slow and Complexes **C2a** and **C3a** exhibits better catecholase activity. They are more selective towards 3,5-DTBC and 4-methyl catechol, whereas selectivity towards other diphenol substrates is much less.
- SOD mimic activity of homonuclear copper complexes was found to be better as compared to that of heteronuclear copper zinc complexes. Complex **C2a** was found to have better SOD mimic activity with low IC_{50} value than other homonuclear copper complexes.
- Typically, the complexes **C2a** and **C3a** having the lowest ionization potential as calculated on the basis of DFT calculations, are found to have overall better activity as compared to the other complexes.
- The complexes act as good functional models for copper active site in SOD, ascorbate oxidase and catecholase enzymes and have reasonably good K_m and k_{cat} values in ascorbate acid oxidase and catecholase activity. They also have very low IC_{50} values making them a better SOD mimics.

Supplementary Information

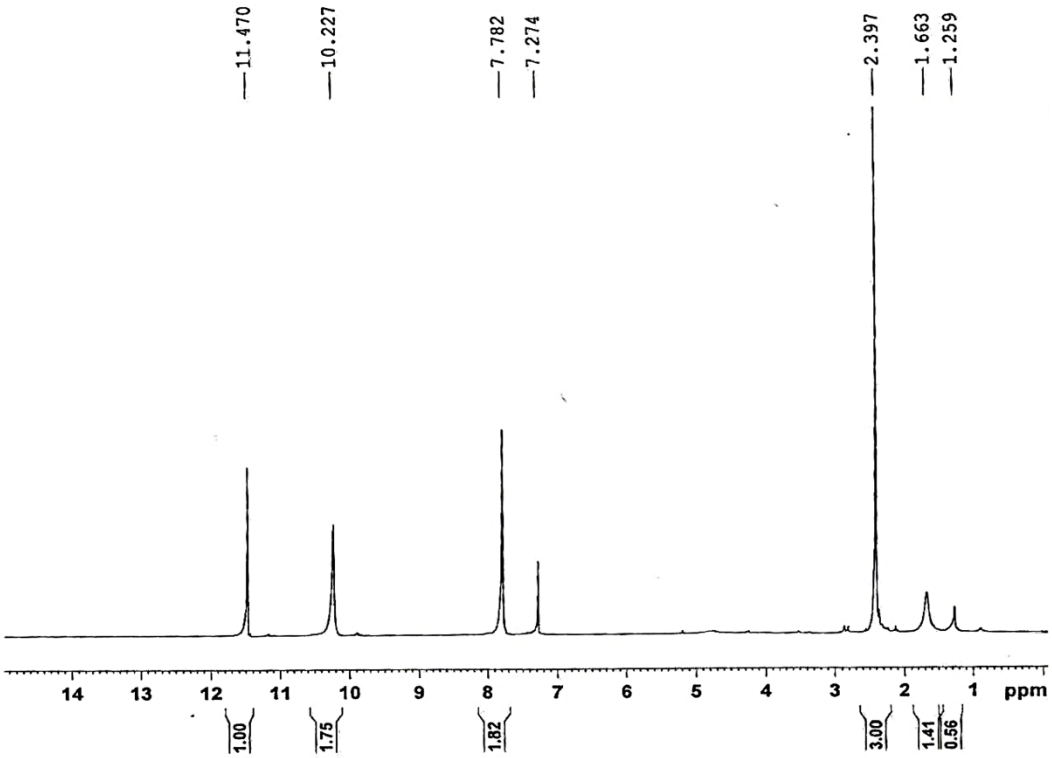

Fig. S2.1 *^{1}H NMR spectrum of dfc in $CDCl_3$*

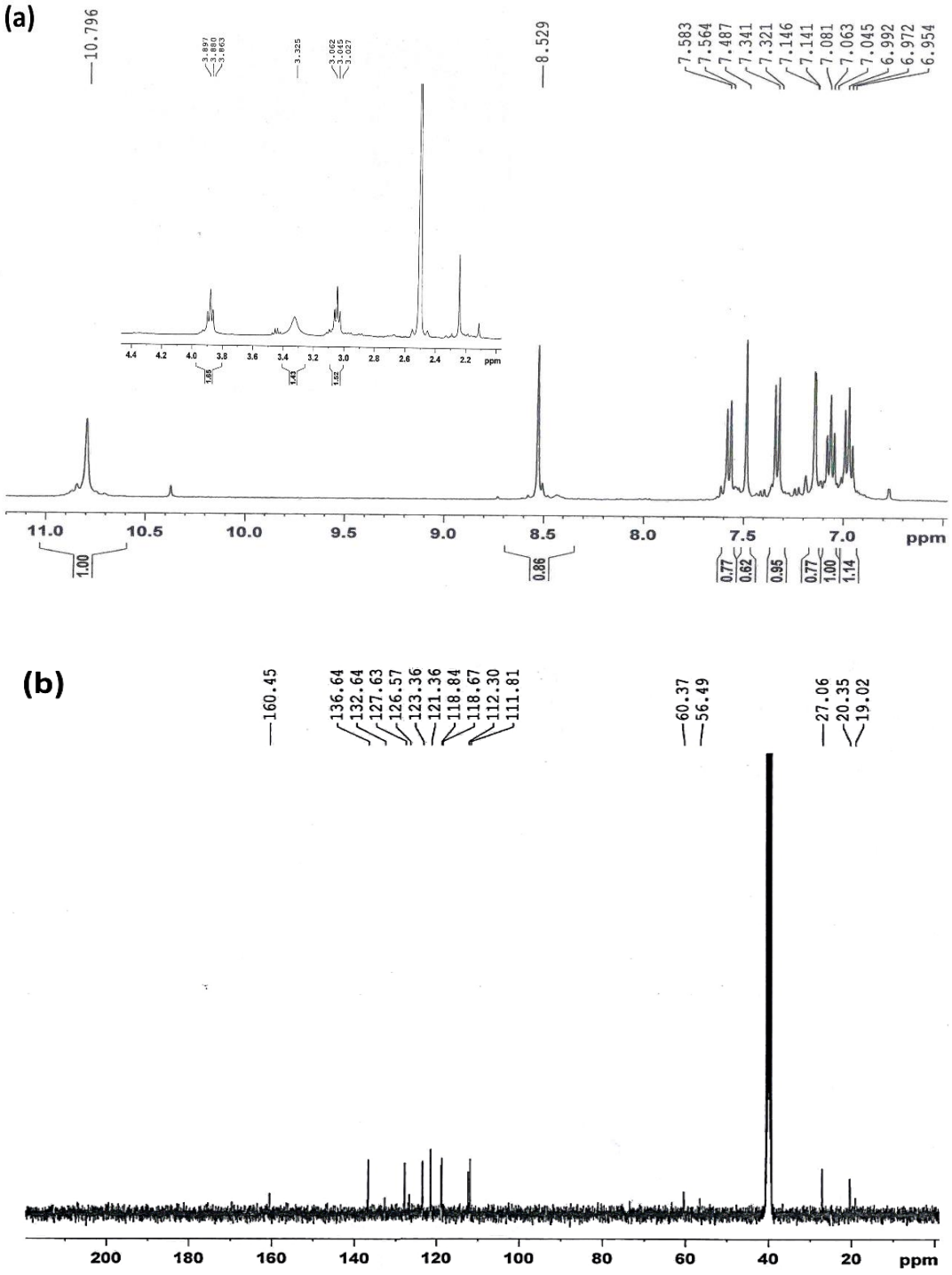

Fig. S2.2 *NMR spectra of* $\boldsymbol{L^2}$ *in* $CDCl_3$ *(a)* ^1H *(b)* ^{13}C

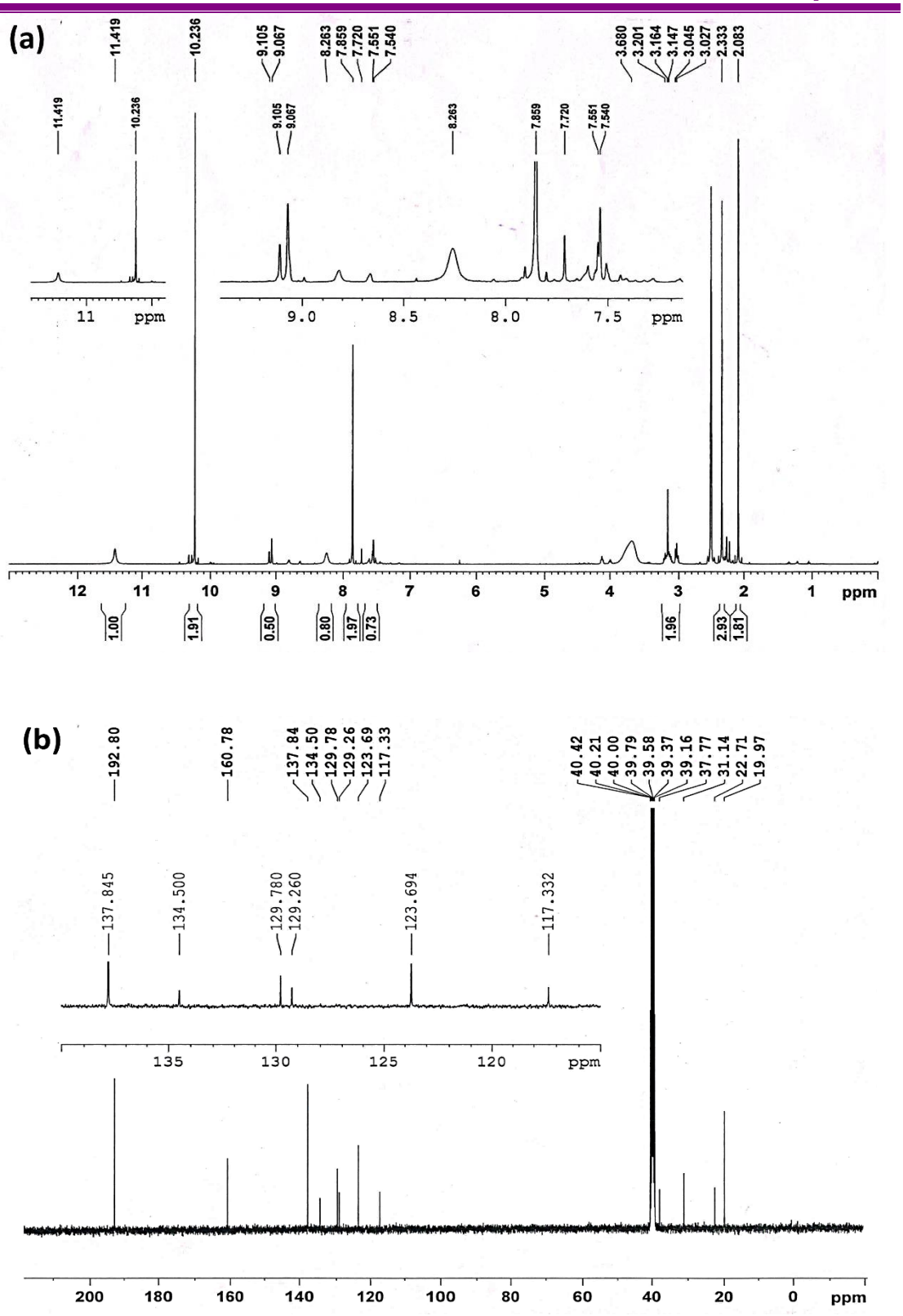

Fig. S2.3 *NMR spectra of* L^3 *in DMSO-*d_6 *(a)* ^1H *(b)* ^{13}C

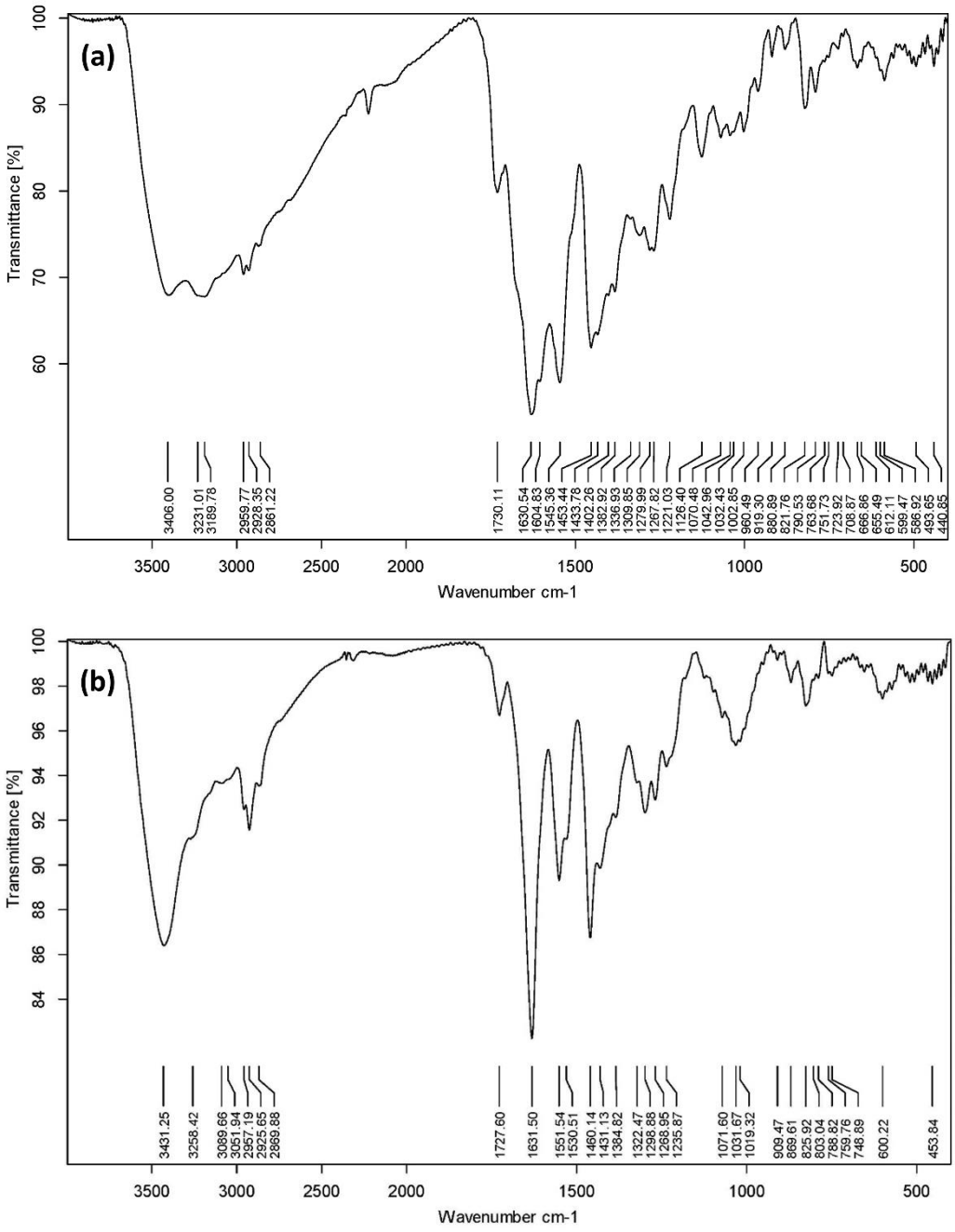

Fig. S2.4 *IR spectra of (a)* ***C1a*** *and (b)* ***C1b***

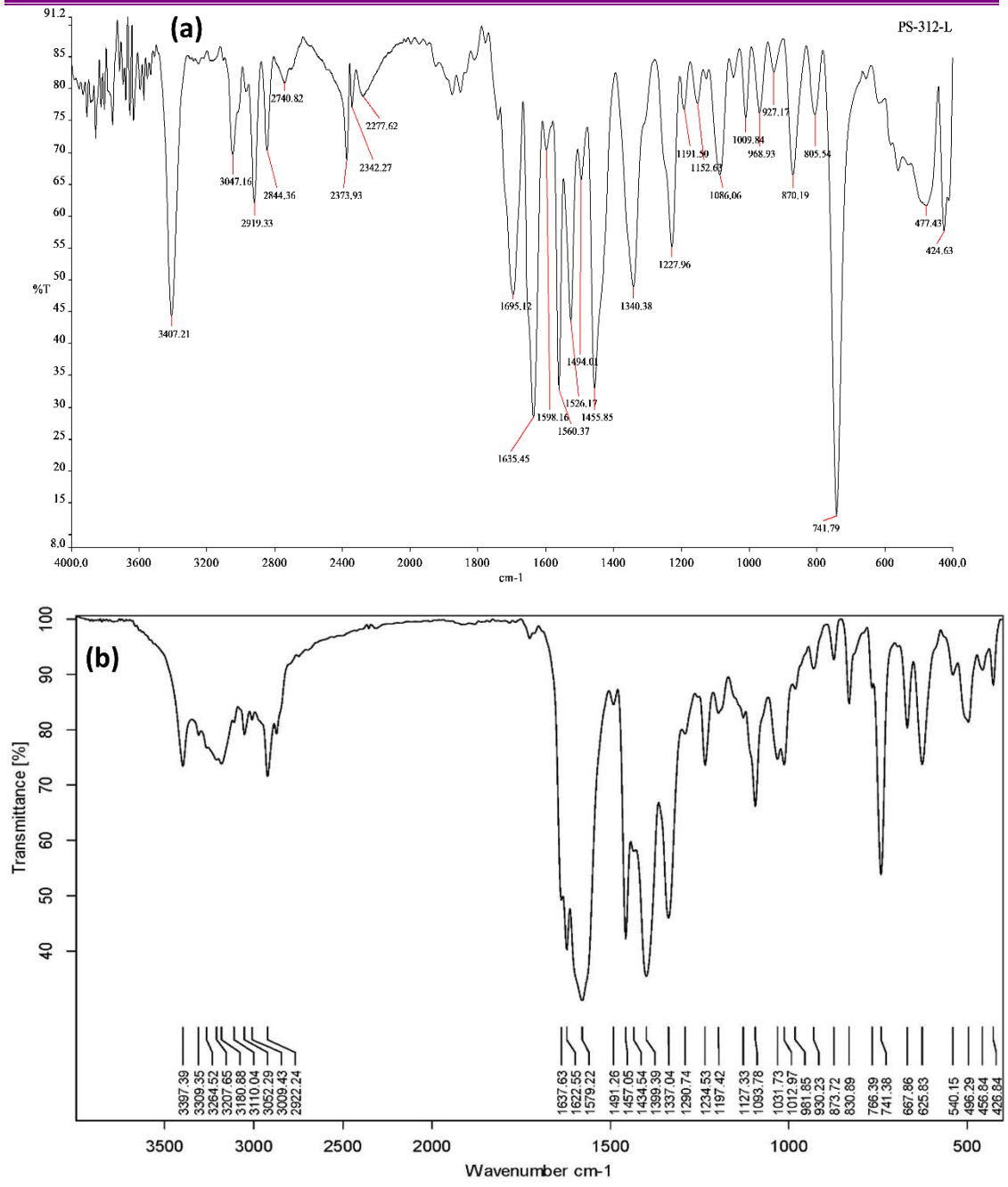

Fig. S2.5 *IR spectra of (a)* ***L²****, (b)* ***C2a***

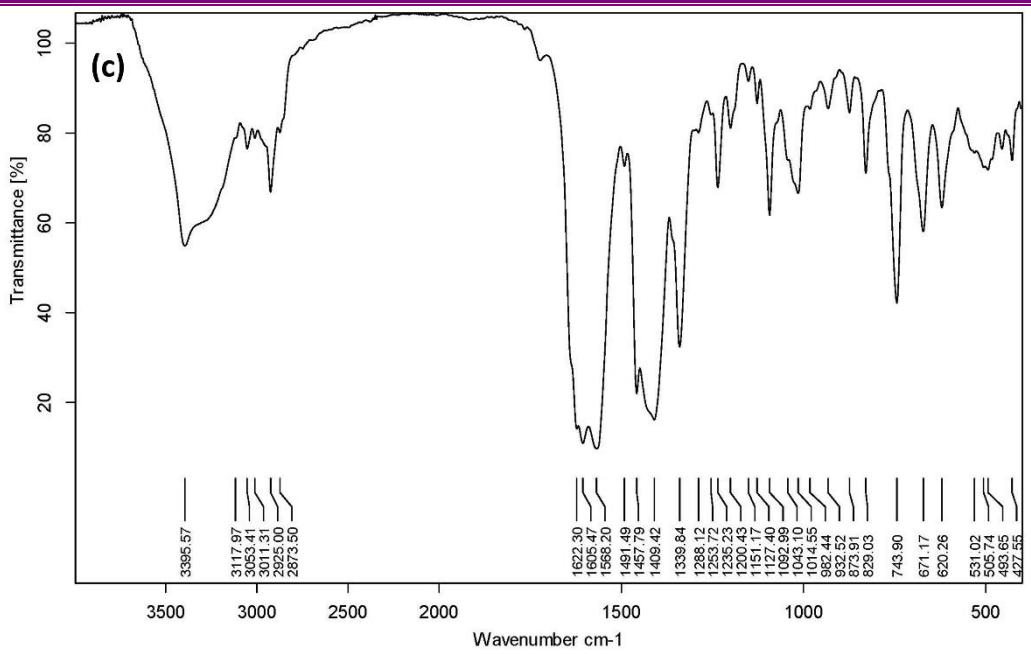

Fig. S2.5 *(Contd…) IR spectrum of (c)* ***C2b***

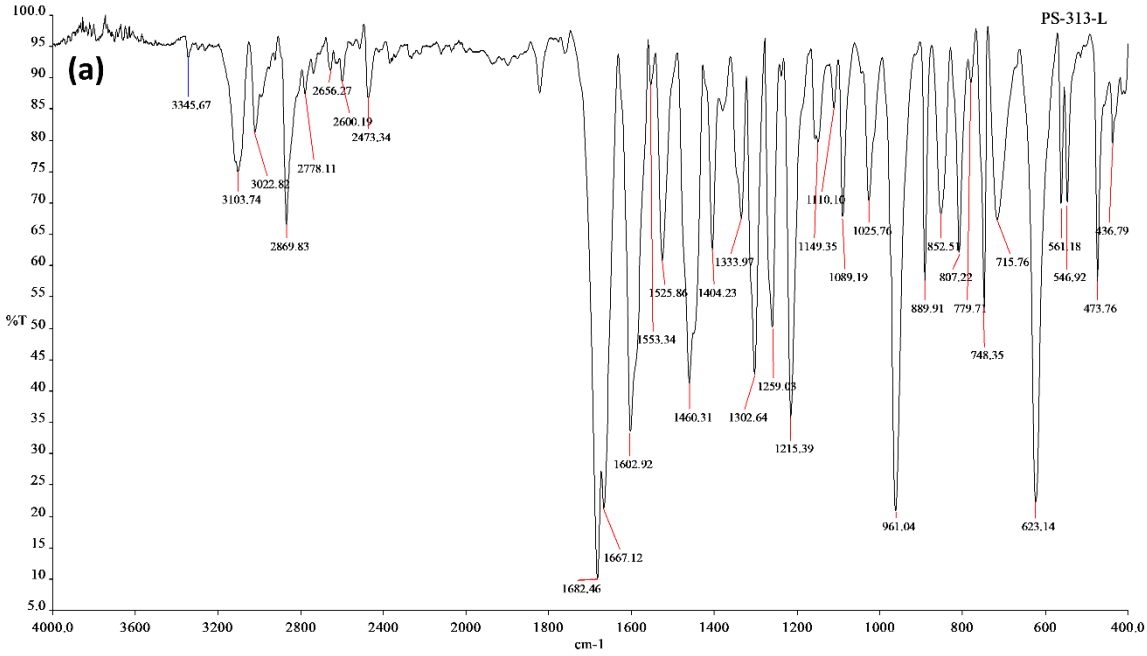

Fig. S2.6 *IR spectrum of (a)* ***L^3***

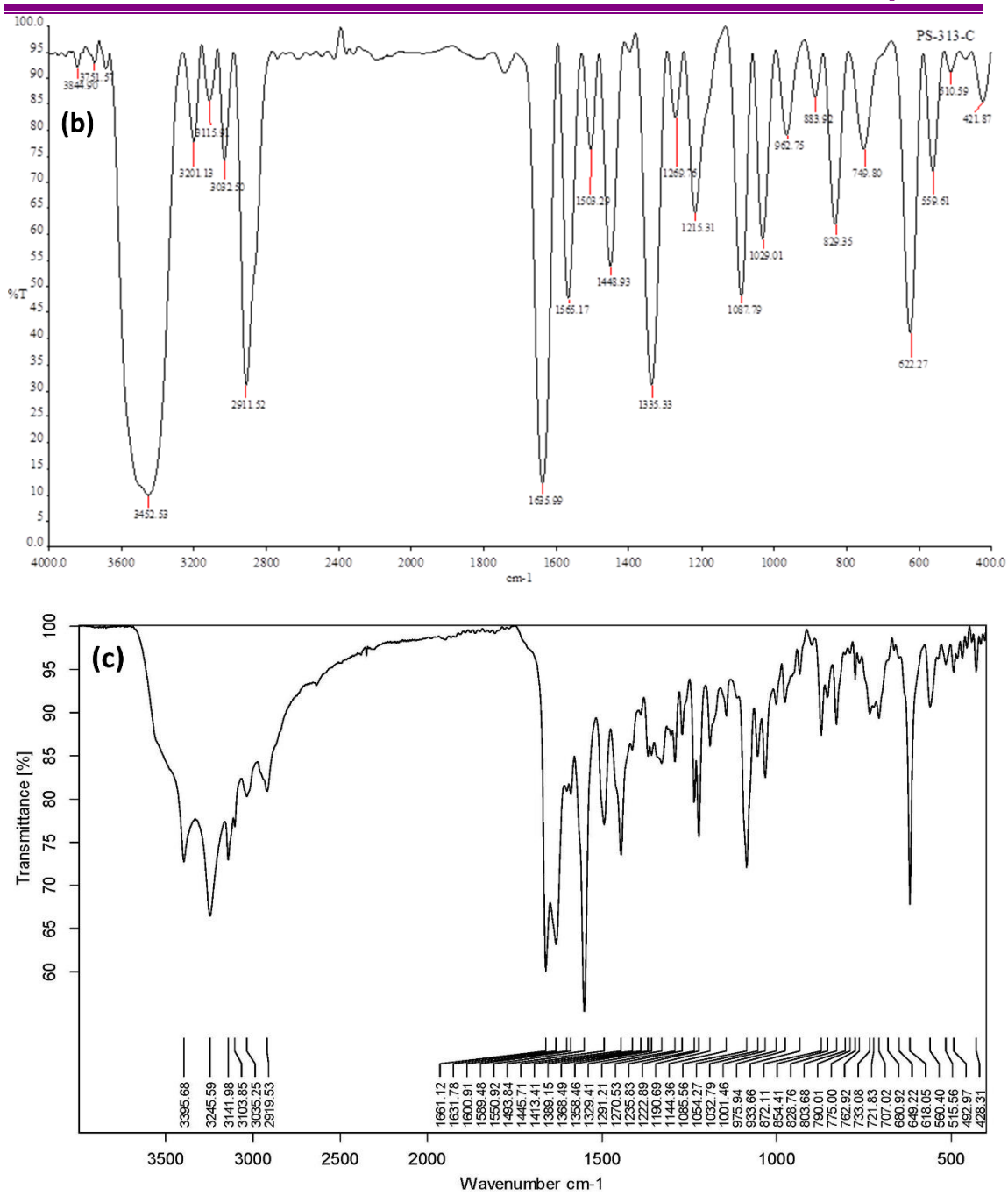

Fig. S2.6 *IR spectra of (b)* ***C3a*** *and (c)* ***C3b***

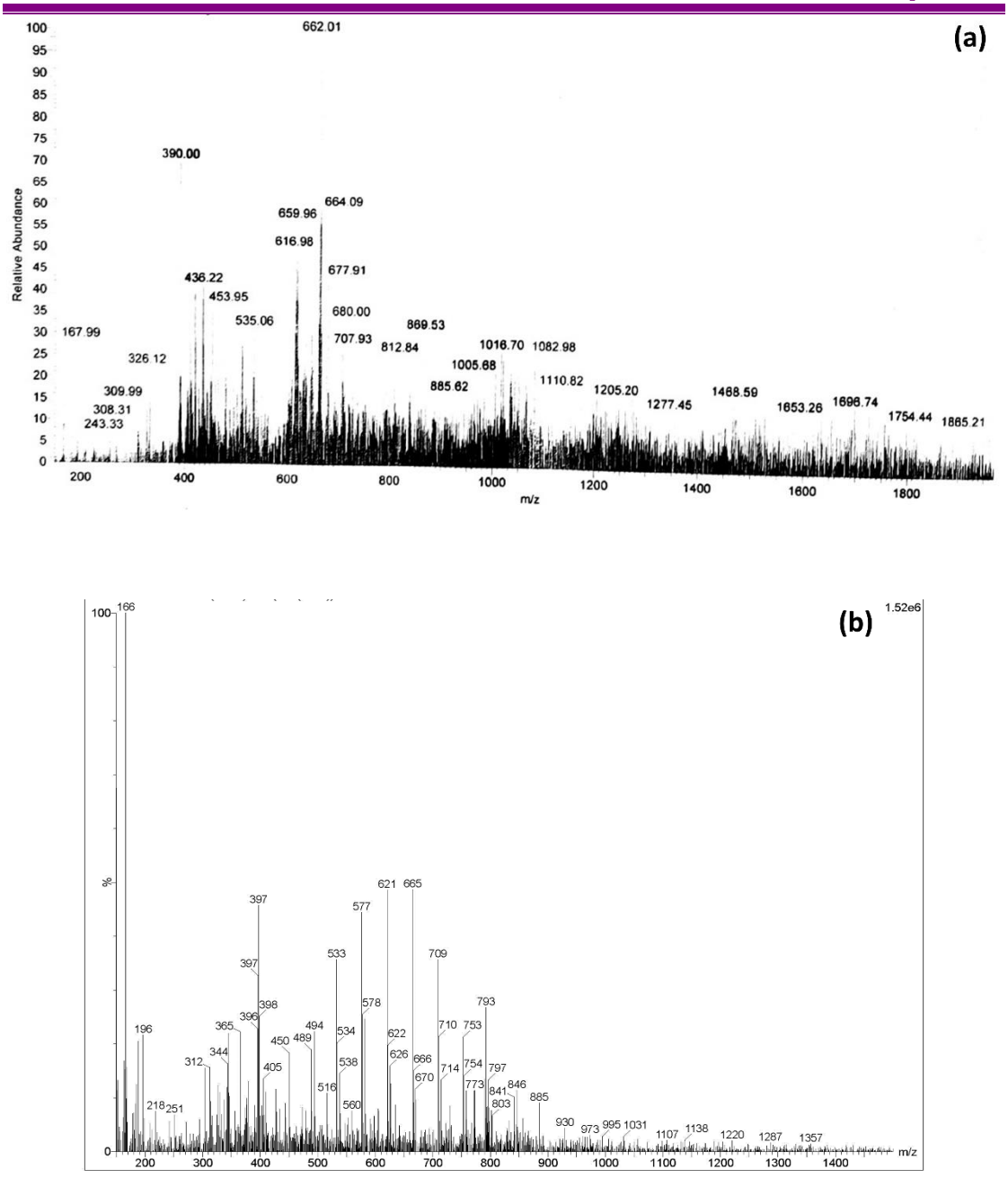

Fig. S2.7 *Mass spectra of (a)* ***C1a*** *and (b)* ***C1b***

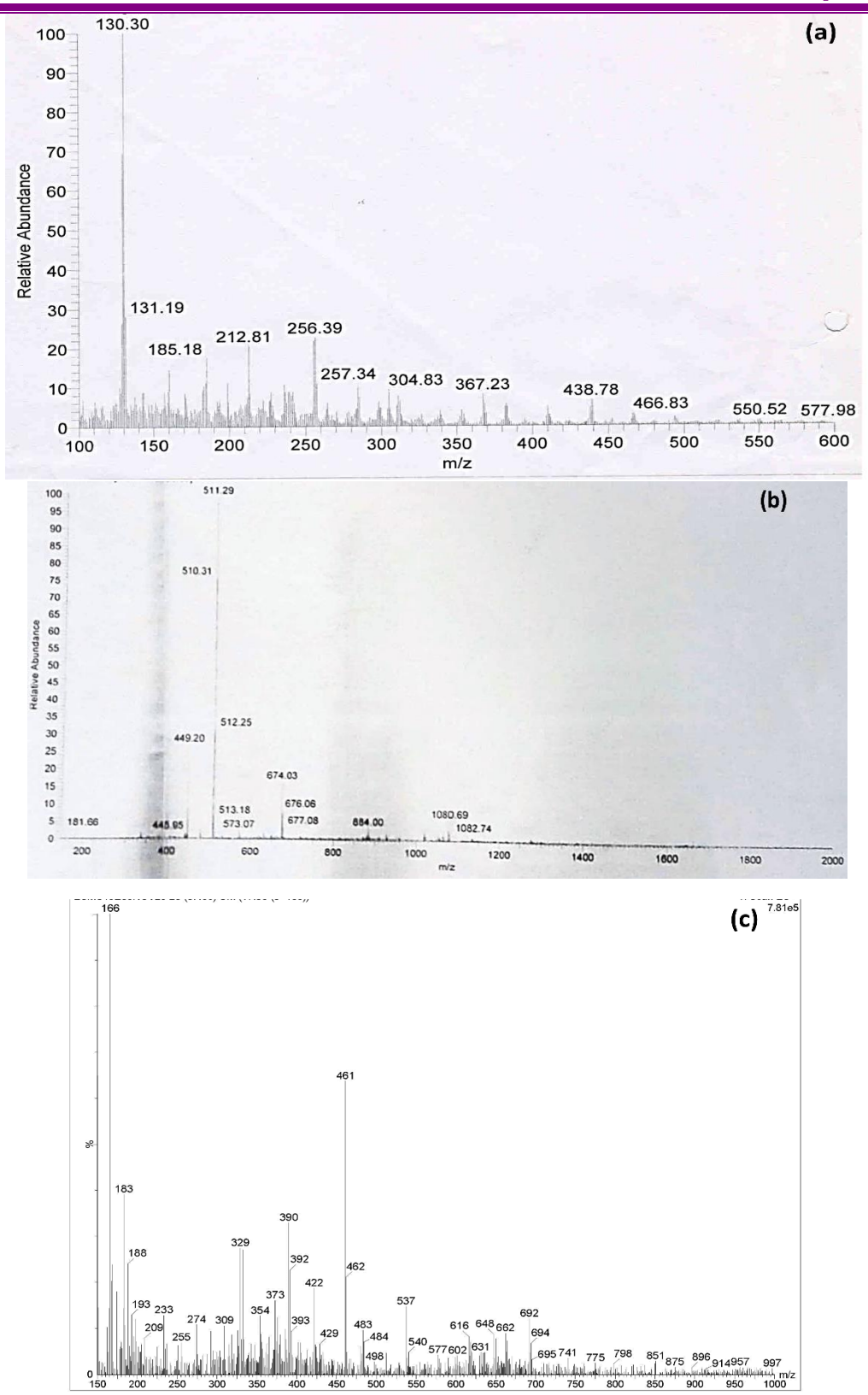

Fig. S2.8 *Mass spectra of (a)* ***L²*** *(b)* ***C2a*** *and (c)* ***C2b***

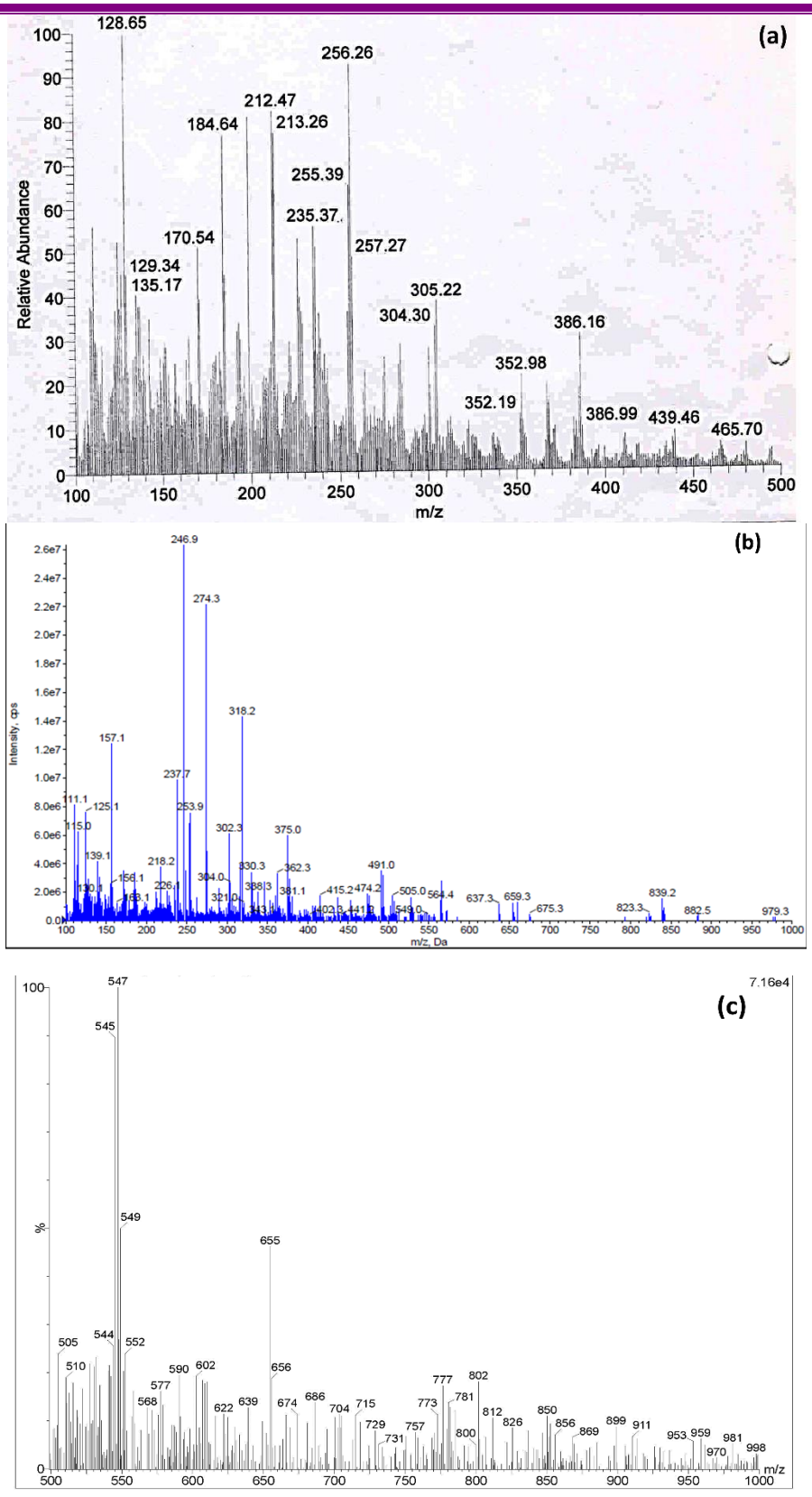

Fig. S2.9 *Mass spectra of (a)* ***L***^{3} *(b)* ***C3a*** *and (c)* ***C3b***

Table S2.1 *Bond lengths of all complexes(**C1-C3**)*

C1a		C1b	
Cu(61)-O(45)	1.9584	Cu(60)-O(45)	1.9058
Cu(61)-O(14)	2.0121	Cu(60)-O(14)	2.0227
Cu(61)-Cl(66)	2.3759	Cu(60)-Cl(65)	2.4023
Cu(61)-N(16)	2.0417	Cu(60)-N(16)	1.9951
Cu(60)-O(27)	1.9597	Zn(66)-O(27)	1.9214
Cu(60)-O(14)	2.0524	Zn(66)-O(14)	2.0879
Cu(60)-Cl(66)	2.3946	Zn(66)-Cl(65)	2.3713
Cu(60)-N(15)	2.0169	Zn(66)-N(15)	2.0656
C2a		**C2b**	
Cu(45)-O(36)	2.0210	N34-Cu45	2.0358
Cu(45)-N(34)	2.0209	N137-Cu45	2.0206
Cu(45)-N(138)	2.0075	O9-Cu45	2.0213
Cu(45)-O(80)	2.3238	O36-Cu45	2.0033
Cu(45)-O(77)	2.4221	O76-Cu45	2.4262
Cu(45)-O(9)	2.0393	O79-Cu45	2.3249
Cu(46)-O(36)	2.0126	N11-Zn138	2.0542
Cu(46)-N(104)	1.9922	N103-Zn138	2.0438
Cu(46)-N(11)	2.0030	O9-Zn138	2.0136
Cu(46)-O(79)	2.4080	O36-Zn138	2.0211
Cu(46)-O(78)	2.3427	O77-Zn138	2.2999
Cu(46)-O(9)	2.0085	O78-Zn138	2.3544
C3a		**C3b**	
Cu(2)-N(7)	1.9251	Cu(1)-N(7)	2.0296
Cu(2)-N(9)	2.0406	Cu(1)-N(5)	1.9570
Cu(2)-O(5)	1.9867	Cu(1)-O(4)	1.9560
Cu(2)-Cl(4)	2.3967	Cu(1)-Cl(2)	2.5504
Cu(1)-N(6)	1.9922	Cu(1)-Cl(3)	2.6544
Cu(1)-N(8)	2.0580	Zn(50)-N(8)	2.1260
Cu(1)-O(5)	2.0210	Zn(50)-O(4)	2.1044
Cu(1)-Cl(3)	2.3805	Zn(50))-Cl(2)	2.5116
Cu(2)-N(7)	1.9251	Zn(50)-Cl(3)	2.4933
Cu(2)-N(9)	2.0406	Zn(50)-N(6)	2.0682
Cu(1)-Cl(3)	2.3805	Cu(1)-N(7)	2.0296
		Cu(1)-N(5)	1.9570

Table S2.2 *Bond angles of all complexes*

C1a		C1b	
N(16)-Cu(61)-O(45)	90.1239	N(16)-Cu(60)-O(45)	92.2228
O(45)-Cu(61)-Cl(66)	97.7165	O(45)-Cu(60)-Cl(65)	94.2415
Cl(66)-Cu(61)-O(14))	90.8143	Cl(65)-Cu(60)-O(14))	84.4757
O(14)-Cu(61)-N(16)	90.3653	O(14)-Cu(60)-N(16)	89.8318
N(15)-Cu(60)-O(27)	92.7139	N(15)-Zn(66)-O(27)	90.6569
O(27)-Cu(60)-Cl(66)	104.9263	O(27)- Zn(66))-Cl(65)	119.1388
Cl(66)-Cu(60)-O(14))	89.3169	Cl(65)- Zn(66))-O(14))	84.9933
O(14)-Cu(60)-N(15)	90.8626	O(14)- Zn(66))-N(15)	88.7213
C2a		**C2b**	
O(9)-Cu(45)-O(36)	81.0254	O9-Cu76-O36	85.0792
O(36)-Cu(45)-N(34)	87.791	N34-Cu76-O36	86.5534
O(9)-Cu(45)-N(138)	86.0421	N34-Cu76-N137	103.3011
N(138)-Cu(45)-N(34)	105.2362	O9-Cu76-N137	85.0844
O(77)-Cu(45)-O(80)	160.6938	O9-Zn138-N11	87.292
N(104)-Cu(46)-N(11)	103.2387	N11-Zn138-N103	100.608
N(11)-Cu(46)-O(9)	87.5016	O36-Zn138-N103	87.4761
N(104)-Cu(46)-O(36)	87.5737	O9-Zn138-O36	84.8163
O(36)-Cu(46)-O(9)	81.9853		
O(78)-Cu(46)-O(79)	162.9399		
C3a		**C3b**	
N(9)-Cu(2)-N(7)	97.1416	N(5)-Cu(1)-N(7)	94.7188
N(7)-Cu(2)-Cl(4)	95.1102	N(7)-Cu(1)-O(4)	90.9549
Cl(4)-Cu(2)-O(5)	82.5554	O(4)-Cu(1)-Cl(2)	81.6227
O(5)-Cu(2)-N(9)	89.0580	N(5)-Cu(1)-Cl(2)	93.5113
N(8)-Cu(1)-N(6)	95.3751	N(5)-Cu(1)-Cl(3)	96.2596
N(6)-Cu(1)-Cl(4)		N(7)-Cu(1)-Cl(3)	126.7869
Cl(4)-Cu(1)-O(5)		O(4)-Cu(1)-Cl(3)	80.6076
O(5)-Cu(1)-N(8)	87.6935	N(8)-Zn(50)-N(6)	92.9667
Cl(3)-Cu(1)-O(5)	85.7522	N(8)- Zn(50)-O(4)	81.9589
Cl(3)-Cu(1)-N(6)	95.3218	O(4)- Zn(50)-Cl(2)	79.8681
		N(6)- Zn(50)-Cl(2)	104.2872
		N(6)- Zn(50)-Cl(3)	96.5344
		N(8)- Zn(50)-Cl(3)	142.6438
		O(4)- Zn(50)-Cl(3)	81.9589

Table S2.3 *Torsion angles of all complexes*

C2a		C2b	
O(9)-Cu(45)-N(34)-O(36) (-1)	168.8165	O9-Cu45-N34-O36 (-1)	171.6326
O(36)-Cu(45)-N(138)-O(9) (-1)	167.0675	O36-Cu45-O137-O9 (-1)	170.1637
O(9)-Cu(46)-N(104)-N(11) (-1)	190.7403	O9-Zn138-N103-N11 (-1)	187.9
N(11)-Cu(46)-O(36)-O(9) (-1)	169.4869	N11-Zn138-O36-O9 (-1)	172.1083
O(9)-Cu(45)-N(34)-O(36) (-2)	182.0564	O9-Cu45-N34-O36 (-2)	180.7583
O(36)-Cu(45)-N(138)-O(9) (-2)	183.3034	O36-Cu45-N137-O9 (-2)	181.6705
O(9)-Cu(46)-N(104)-N(11) (-2)	184.8689	O9-Cu138-N103-N11 (-2)	184.3473
N(11)-Cu(46)-O(36)-O(9) (-2)	183.8188	N11-Zn138-O36-O9 (-2)	182.7669
C3a		**C3b**	
Cl(3)-Cu(1)-N(8)-N(6) (-1)	190.6969	O(4)-Cu(1)-N(5)-Cl(2) (-1)	175.1339
N(5)-Cu(1)-N(6)-N(8) (-1)	183.0686	O(4)-Zn(50)-N(6)-Cl(2) (-1)	184.1553
O(5))-Cu(2)-N(7)-Cl(4) (-1)	177.6656	O(4)-Cu(1)-N(5)-Cl(2) (-2)	182.9628
Cl(3)-Cu(1)-N(8)-N(6) (-2)	155.3624	O(4)-Zn(50)-N(6)-Cl(2) (-2)	178.6823
N(5)-Cu(1)-N(6)-N(8) (-2)	171.0086		
O(5))-Cu(2)-N(7)-Cl(4) (-2)	191.2795		

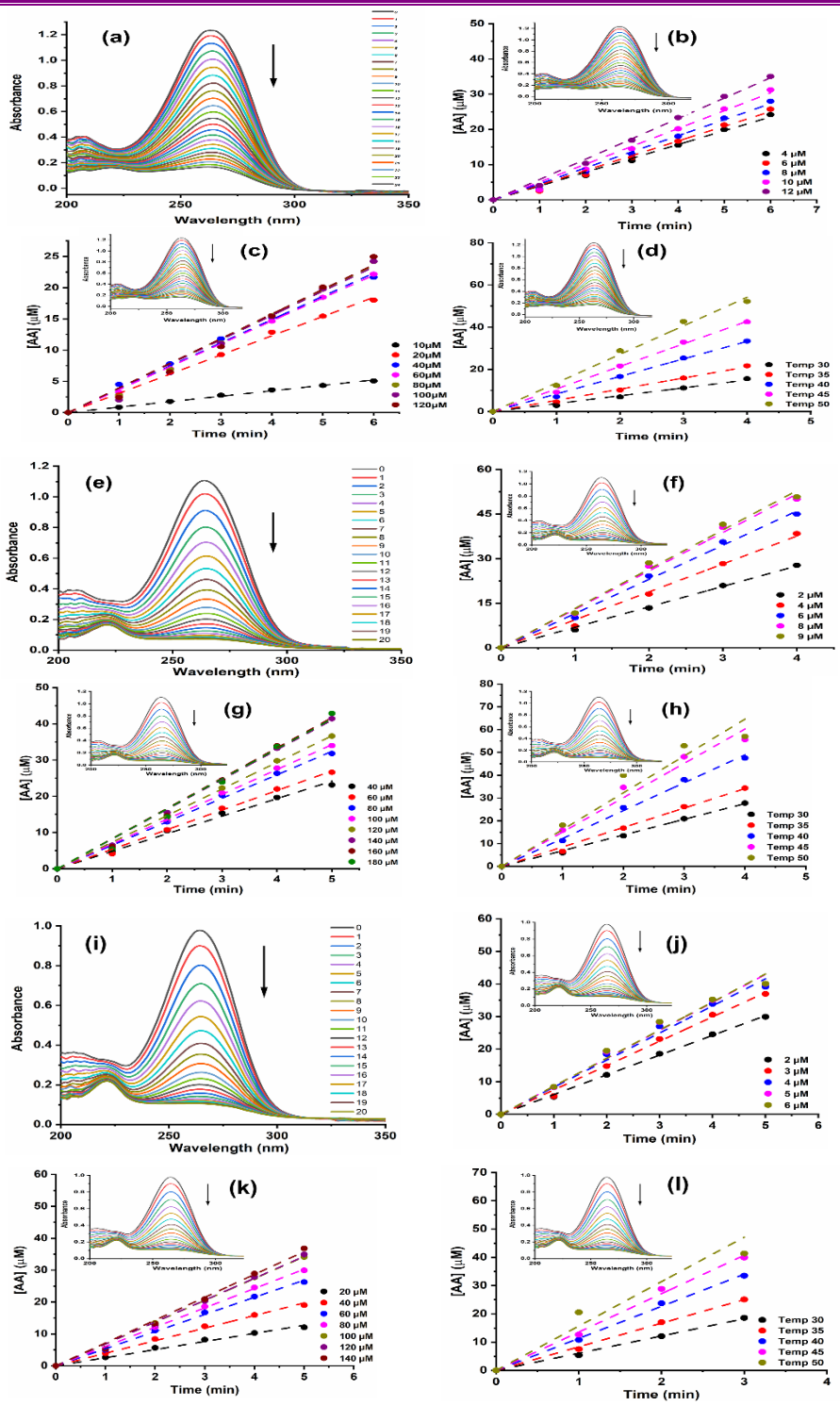

Fig. S2.10 *Time dependent spectral changes in AA corresponding to (a)* ***C1b*** *(e)* ***C2a*** *(i)* ***C2b*** *catalyzed oxidation and Plot of [AA] as function of time with respect to (b) Catalyst (c) Substrate (d) temperature of* ***C1b****, (f) Catalyst (g) Substrate (h) temperature of* ***C2a****, (j) Catalyst (k) Substrate (l) temperature of* ***C2b****, (Inset: Plot of absorbance vs wavelength at different time intervals)*

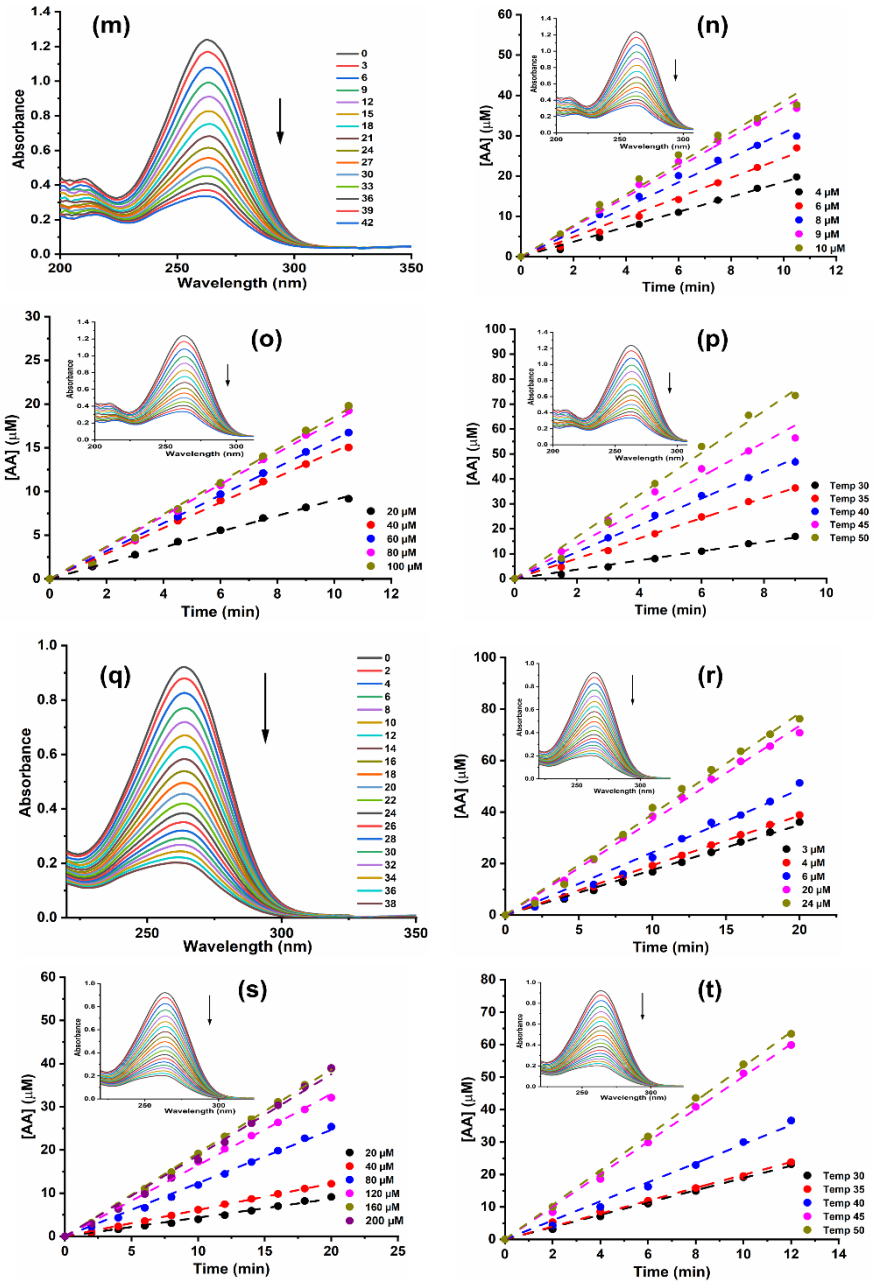

Fig. S2.10 *(Contd..): Time dependent spectral changes in AA corresponding to (m)* ***C3a*** *and (q)* ***C3b*** *catalyzed oxidation and Plot of [AA] as function of time with respect to (n) Catalyst (o) Substrate (p) temperature of* ***C3a****, and (r) Catalyst (s) Substrate (t) temperature of* ***C3b****. (Inset: Plot of absorbance vs wavelength at different time intervals)*

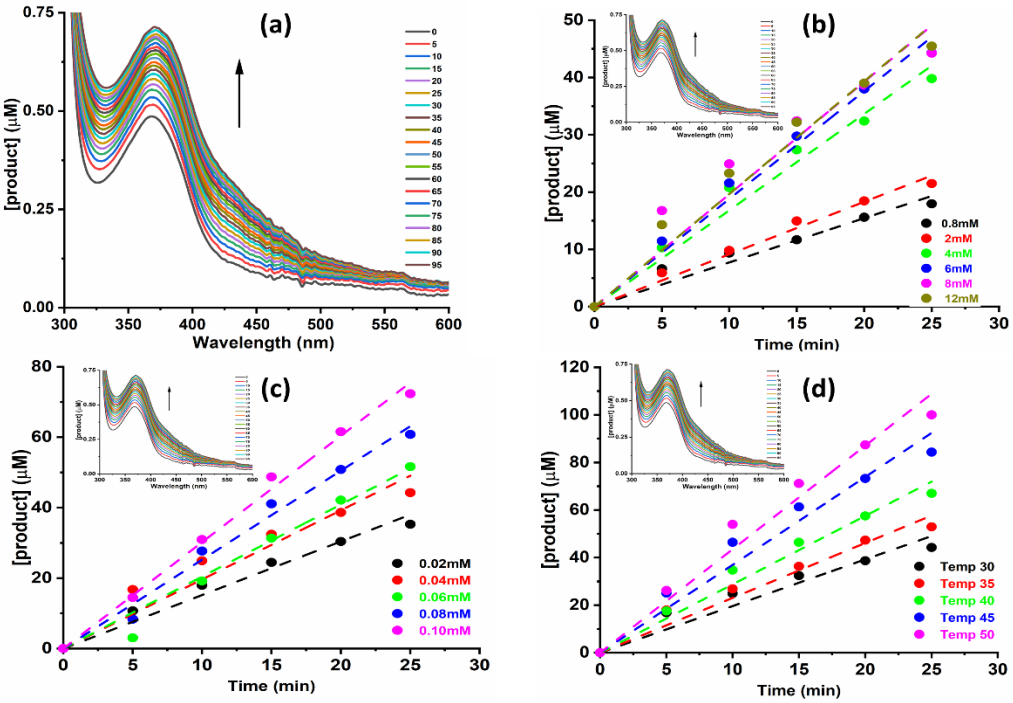

Fig. S2.11 *(a) Time dependent spectral changes from 0 to 14 mins of 4-MC corresponding to* ***C2a*** *catalyzed oxidation and (b-d) Plot of [product] as function of time with respect to catalyst (b), substrate (c) and temperature (d) (Inset: Plot of absorbance vs wavelength at different time interval*

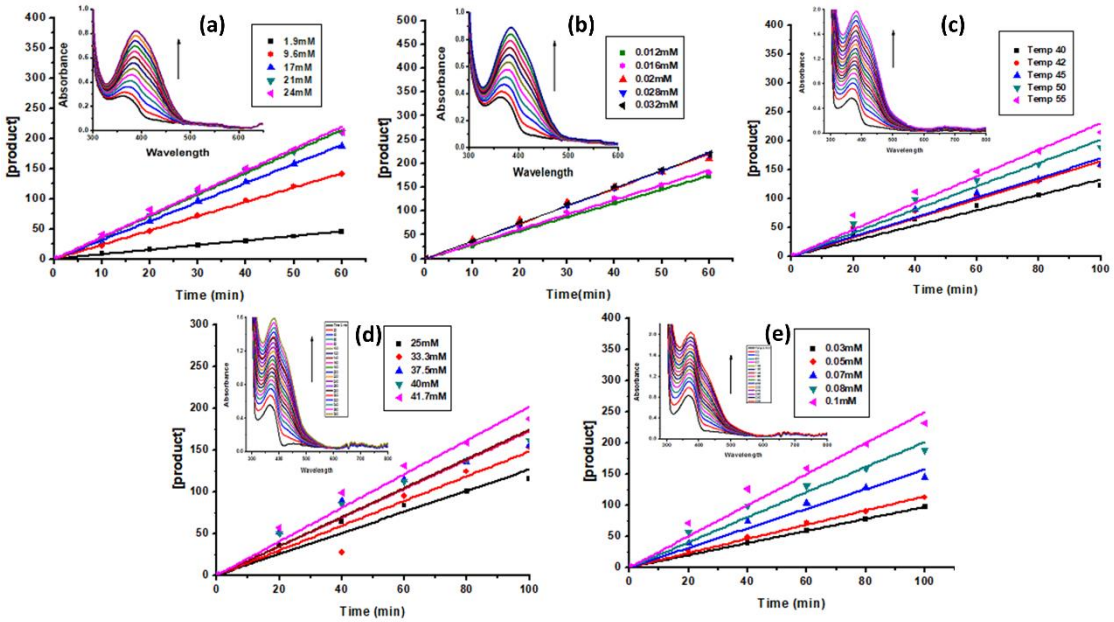

Fig. S2.12 *Plot of [product] as function of time with respect to (a)substrate (b) catalyst for 3,5-DTBC and Plot of [product] as function of time with respect to (c)substrate (d) catalyst (e) temperature for 4-MC of complex* ***C3a*** *(Inset: Plot of absorbance vs wavelength at different time intervals)*

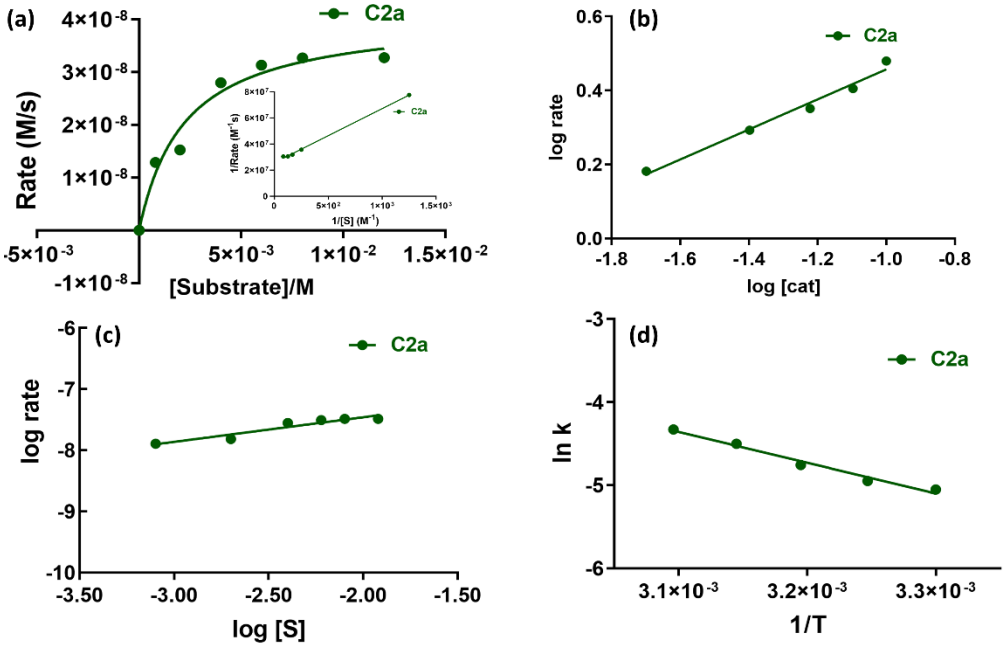

Fig. S2.13 *(a) Plot of Rate vs [Substrate]of Michaelis Menten model for complex* ***C2a*** *(Inset: Lineweaver Burk plot); (b) Plot of log(rate) vs log[cat] for complex* ***C2a****; (c) Plot of log(rate) vs log[S] for complex* ***C2a****; and (d) Arrhenius plot for complex* ***C2a*** *with 4-MC as substrate*

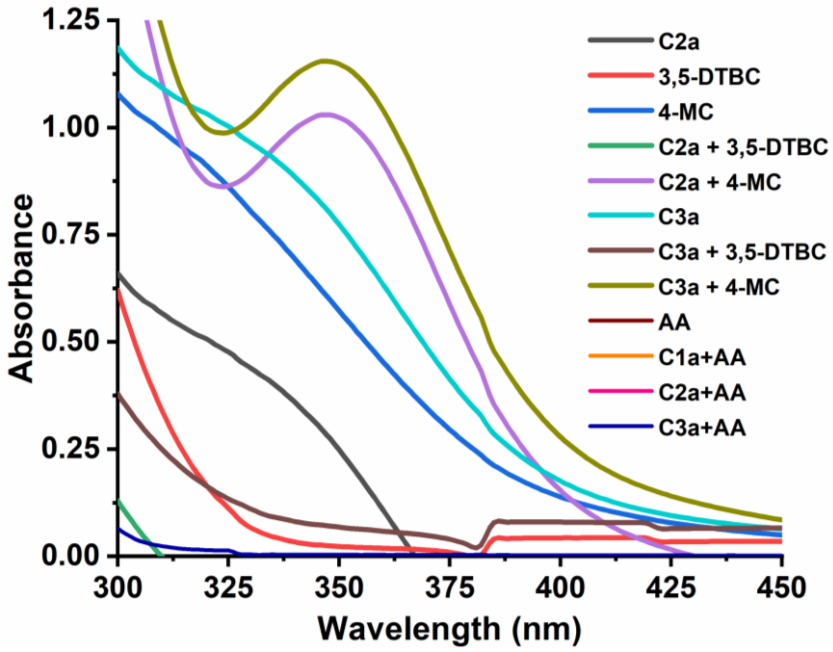

Fig. S2.14 *Electronic spectra of the formation of I_3^- ion in the presence of H_2O_2 (detection was achieved as mentioned in the text).*

References

1. Than, R., Feldmann, A. A. & Krebs, B. Structural and functional studies on model compounds of purple acid phosphatases and catechol oxidases. *Coord. Chem. Rev.* **182**, 211–241 (1999).
2. Trammell, R., Rajabimoghadam, K. & Garcia-Bosch, I. Copper-Promoted Functionalization of Organic Molecules: from Biologically Relevant Cu/O2 Model Systems to Organometallic Transformations. *Chem. Rev.* **119**, 2954–3031 (2019).
3. Lewis, E. A. & Tolman, W. B. Reactivity of Dioxygen−Copper Systems. *Chem. Rev.* **104**, 1047–1076 (2004).
4. Casellato, U. Vigato, P. A. Fenton, David E Vidali, M. Compartmental Ligands: Routes to Homo- and Heteroldinuclear Complexes. *Chem. Soc. Rev.* **8**, 199–220 (1979).
5. Robson, R. Complexes of Binucleating Ligands I Two Novel Binuclear Cupric Complexes. *Inorg. Nucl. Chem. Lett.* **6**, 125–128 (1970).
6. Vigato, P. A., Tamburini, S. & Fenton, D. E. The activation of small molecules by dinuclear complexes of copper and other metals. *Coord. Chem. Rev.* **106**, 25–170 (1990).
7. Willett, R. D., Gatteschi, D. & Kahn, O. Magneto-Structural Correlations in Exchange Coupled Systems. *Magneto-Structural Correl. Exch. Coupled Syst.* 2015 (1984).
8. Thompson, L. K., Mandai, S. K., Tandon, S. S., Bridson, J. N. & Park, M. K. Magnetostructural correlations in Bis(μ2-phenoxide)-bridged macrocyclic dinuclear copper(II) complexes. influence of electron-withdrawing substituants on exchange coupling. *Inorg. Chem.* **35**, 3117–3125 (1996).
9. Mandal, S. K., Thompson, L. K., Newlands, M. J. & Gabe, E. J. Structural, Magnetic, and Electrochemical Studies on Macrocyclic Dicopper(II) Complexes with Varying Chelate Ring Size. *Inorg. Chem.* **28**, 3707–3713 (1989).
10. Mandal, S. K., Thompson, L. K., Newlands, M. J., Gabe, E. J. & Nag, K. Structural and Magnetic Studies on Macrocyclic Dicopper(II) Complexes. Influence of Electron-Withdrawing Axial Ligands on Spin Exchange. *Inorg. Chem.* **29**, 1324–1327 (1990).
11. Kennedy, B. J., Rodgers, J. R. & Peter, R. Magnetic Interactions in Metal Complexes of Binucleating Ligands . 2 . Synthesis and Properties of Binuclear Copper (11) Compounds Containing Exogenous Ligands That Bridge through Two Atoms . Crystal and Molecular Structure of a Binuclear 1 , 3-Bis (sa. 3258–3264 (1985).
12. Kavlakoglu, E., Elmali, A. & Elerman, Y. Magnetic Super-Exchange Mechanism and Crystal Structure of a Binuclear μ-Acetato-Bridged Copper(II) Complex of Pentadentate Binucleating Ligand. An Influence of Overlap Interactions to Magnetic Properties. *Zeitschrift fur Naturforsch. - Sect. B J. Chem. Sci.* **57**, 223–230 (2002).
13. Thompson, L. K., Mandal, S. K., Charland, J.-P. & Gabe, E. J. Magnetism and structure in a series of halogen and hydroxo-bridged binuclear copper(II) diazine complexes. Structure of a dibromobridged derivative [Cu 2 (C 14 H 10 N 4 S 2)Br 4] . *Can. J. Chem.* **66**, 348–354 (1988).
14. Fusi, V., Llobet, A., Mahía, J., Micheloni, M., Paoli, P., Ribas, X. & Rossi, P. A new CuI complex that mimics the cresolase reaction of tyrosinase and the crystal structure of its oxygenated CuII complex. *Eur. J. Inorg. Chem.* 987–990 (2002).
15. Rodríguez, M., Llobet, A., Corbella, M., Müller, P., Usón, M. A., Martell, A. E. & Reibenspies, J. Solvent controlled nuclearity in Cu(II) complexes linked by the CO32- ligand: Synthesis, structure and magnetic properties. *J. Chem. Soc. Dalt. Trans.* 2900–

2906 (2002).
16. Gao, E. Q., Yang, G. M., Liao, D. Z., Jiang, Z. H., Yan, S. P. & Wang, G. L. Synthesis and magnetic properties of new tetranuclear copper(II)- nickel(II) complexes of macrocyclic oxamides. *J. Chem. Res. - Part S* 278–279 (1999).
17. Kitajima, N. & Moro-oka, Y. Copper-Dioxygen Complexes. Inorganic and Bioinorganic Perspectives. *Chem. Rev.* **94**, 737–757 (1994).
18. Kitajima, N. Synthetic approach to the structure and function of copper proteins. *Adv. Inorg. Chem.* **39**, 1–77 (1992).
19. Reim, J., Werner, R., Haase, W. & Krebs, B. From tetranuclear μ4-oxo to μ4-peroxocopper(II) complexes. *Chem. - A Eur. J.* **4**, 289–298 (1998).
20. Karlin, K. D., Hayes, J. C., Gultneh, Y., Cruse, R. W., McKown, J. W., Hutchinson, J. P. & Zubieta, J. Copper-Mediated Hydroxylation of an Arene: Model System for the Action of Copper Monooxygenases. Structures of a Binuclear Cu(I) Complex and Its Oxygenated Product. *J. Am. Chem. Soc.* **106**, 2121–2128 (1984).
21. Solomon, E. I., Sundaram, U. M. & Machonkin, T. E. Multicopper oxidases and oxygenases. *Chem. Rev.* **96**, 2563–2605 (1996).
22. Holland, P. L. & Tolman, W. B. Dioxygen activation by copper sites: Relative stability and reactivity of (μ-η2:η2-peroxo)- and bis(μ-oxo)dicopper cores. *Coord. Chem. Rev.* **190**–**192**, 855–869 (1999).
23. Kaim, W. & Rall, J. Copper-A "Modern" Bioelement. *Angew. Chemie - Int. Ed.* **35**, 43–60 (1996).
24. Lambert, E., Chabut, B., Chardon-Noblat, S., Deronzier, A., Chottard, G., Bousseksou, A., Tuchagues, J. P., Laugier, J., Bardet, M. & Latour, J. M. Synthesis, structural, magnetic, and redox properties of asymmetric diiron complexes with a single terminally bound phenolate ligand. Relevance to the purple acid phosphatase enzymes. *J. Am. Chem. Soc.* **119**, 9424–9437 (1997).
25. Murthy, N. N., Mahroof-Tahir, M. & Karlin, K. D. Dicopper(I) complexes of unsymmetrical binucleating ligands and their dioxygen reactivities. *Inorg. Chem.* **40**, 628–635 (2001).
26. Zhang, C. X., Liang, H.-C., Humphreys, K. J. & Karlin, K. D. Copper-dioxygen complexes and their roles in biomimetic oxidation reactions. in *Advances in Catalytic Activation of Dioxygen by Metal Complexes* (ed. Simándi, L. I.) 79–121 (Springer US, 2002).
27. Suzuki, M., Kanatomi, H. & Murase, I. Synthesis and Properties of Binuclear Cobalt(Ii) Oxygen Adduct With 2,6-Bis[Bis(2-Pyridylmethyl)Aminomethyl]-4-Methylphenol. *Chem. Lett.* **10**, 1745–1748 (1981).
28. Gamez, P., von Harras, J., Roubeau, O., Driessen, W. L. & Reedijk, J. Synthesis and catalytic activities of copper(II) complexes derived from a tridentate pyrazole-containing ligand. X-ray crystal structure of [Cu2(μ-dpzhp-O, N, N′)2][Cu(MeOH)Cl 3]2. *Inorganica Chim. Acta* **324**, 27–34 (2001).
29. Torelli, S., Belle, C., Gautier-Luneau, I., Pierre, J. L., Saint-Aman, E., Latour, J. M., Le Pape, L. & Luneau, D. pH-controlled change of the metal coordination in a dicopper(II) complex of the ligand H-BPMP: Crystal structures, magnetic properties, and catecholase activity. *Inorg. Chem.* **39**, 3526–3536 (2000).
30. Rey, N. A., Neves, A., Bortoluzzi, A. J., Pich, C. T. & Terenzi, H. Catalytic promiscuity in biomimetic systems: Catecholase-like activity, phosphatase-like activity, and hydrolytic DNA cleavage promoted by a new dicopper(II) hydroxo-bridged complex.

Inorg. Chem. **46**, 348–350 (2007).

31. Ryan, S., Adams, H., Fenton, D. E., Becker, M. & Schindler, S. Intramolecular Ligand Hydroxylation: Mechanistic Studies on the Reaction of a Copper(I) Schiff Base Complex with Dioxygen. *Inorg. Chem.* **37**, 2134–2140 (1998).
32. Gerdemann, C., Eicken, C. & Krebs, B. The crystal structure of catechol oxidase: New insight into the function of type-3 copper proteins. *Acc. Chem. Res.* **35**, 183–191 (2002).
33. Rompel, A., Fischer, H., Biildt-karentzopoulos, K., Meiwes, D. & Zippel, F. Spectroscopic and EXAFS studies on Catechol Oxidases with dinuclear copper centers of type 3: Evidence for μ-η2:η2-peroxo-intermediates during the reaction with catechol. *J. Inorg. Biochem.* **59**, 715 (1995).
34. Ghosh, D., Lal, T. K. & Mukherjee, R. Dicopper complexes of relevance to tyrosinase modelling: An overview. *Proc. Indian Acad. Sci. Chem. Sci.* **108**, 251–256 (1996).
35. Gentschev, P., Möller, N. & Krebs, B. New functional models for catechol oxidases. *Inorganica Chim. Acta* **300**–**302**, 442–452 (2000).
36. Fernandes, C., Neves, A., Bortoluzzi, A. J., Mangrich, A. S., Rentschler, E., Szpoganicz, B. & Schwingel, E. A new dinuclear unsymmetric copper(II) complex as model for the active site of catechol oxidase. *Inorganica Chim. Acta* **320**, 12–21 (2001).
37. González-Álvarez, M., Alzuet, G., Borrás, J., García-Granda, S. & Montejo-Bernardo, J. M. Structural and functional models for the dinuclear copper active site in catechol oxidases: Synthesis, X-ray crystal structures, magnetic and spectroscopic properties of μ-methoxo-bridged dinuclear copper(II) complexes with N-substituted sulfonamide ligan. *J. Inorg. Biochem.* **96**, 443–451 (2003).
38. Alves, W. A., Bagatin, I. A. & Da Costa Ferreira, A. M. Equilibria and tyrosinase activity of a dinuclear and its analogous tetranuclear imidazolate-bridged copper(II) complexes. *Inorganica Chim. Acta* **321**, 11–21 (2001).
39. Rompel, A., Fischer, H., Meiwes, D., Büldt-Karentzopoulos, K., Dillinger, R., Tuczek, F., Witzel, H. & Krebs, B. Purification and spectroscopic studies on catechol oxidases from Lycopus europaeus and Populus nigra: Evidence for a dinuclear copper center of type 3 and spectroscopic similarities to tyrosinase and hemocyanin. *J. Biol. Inorg. Chem.* **4**, 56–63 (1999).
40. Börzel, H., Comba, P. & Pritzkow, H. Structural studies on dicopper(II) compounds with catechol oxidase activity. *Chem. Commun.* **2**, 97–98 (2001).
41. Gupta, M., Mathur, P. & Butcher, R. J. Synthesis, crystal structure, spectral studies, and catechol oxidase activity of trigonal bipyramidal Cu(II) complexes derived from a tetradentate diamide bisbenzimidazole ligand. *Inorg. Chem.* **40**, 878–885 (2001).
42. Than, R., Feldmann, A. A. & Krebs, B. Structural and functional studies on model compounds of purple acid phosphatases and catechol oxidases. *Coord. Chem. Rev.* **182**, 211–241 (1999).
43. Knight, J. A. & Wu, J. T. Catecholamines and their metabolites: Clinical and laboratory aspects. *Lab. Med.* **18**, 153–158 (1987).
44. Sorrell, T. N. Synthetic models for binuclear copper proteins. *Tetrahedron* **45**, 3–68 (1989).
45. Koval, I. A., Gamez, P., Belle, C., Selmeczi, K. & Reedijk, J. Synthetic models of the active site of catechol oxidase: Mechanistic studies. *Chem. Soc. Rev.* **35**, 814–840 (2006).
46. Zanello, P., Tamburini, S., Vigato, P. A. & Mazzocchin, G. A. Syntheses, structure and electrochemical characterization of homo- and heterodinuclear copper complexes with

compartmental ligands. *Coord. Chem. Rev.* **77**, 165–273 (1987).

47. Koval, I. A., Belle, C., Selmeczi, K., Philouze, C., Saint-Aman, E., Schuitema, A. M., Gamez, P., Pierre, J.-L. & Reedijk, J. Catecholase activity of a μ-hydroxodicopper(II) macrocyclic complex: structures, intermediates and reaction mechanism. *JBIC J. Biol. Inorg. Chem.* **10**, 739–750 (2005).
48. Selmeczi, K., Réglier, M., Giorgi, M. & Speier, G. Catechol oxidase activity of dicopper complexes with N-donor ligands. *Coord. Chem. Rev.* **245**, 191–201 (2003).
49. Yang, C. T., Vetrichelvan, M., Yang, X., Moubaraki, B., Murray, K. S. & Vittal, J. J. Syntheses, structural properties and catecholase activity of copper(ii) complexes with reduced Schiff base N-(2-hydroxybenzyl)-amino acids. *J. Chem. Soc. Dalt. Trans.* **4**, 113–121 (2004).
50. Zerón, P., Westphal, M., Comba, P., Flores-Álamo, M., Stueckl, A. C., Leal-Cervantes, C., Ugalde-Saldívar, V. M. & Gasque, L. Dinuclear Copper(II) Complexes with Distant Metal Centers: Weaker Donor Groups Increase Catecholase Activity. *Eur. J. Inorg. Chem.* **2017**, 56–62 (2017).
51. Reim, J. & Krebs, B. Synthesis, structure and catecholase activity study of dinuclear copper(II) complexes. *J. Chem. Soc. - Dalt. Trans.* 3793–3804 (1997).
52. Chakraborty, P., Adhikary, J., Ghosh, B., Sanyal, R., Chattopadhyay, S. K., Bauzá, A., Frontera, A., Zangrando, E. & Das, D. Relation between the Catalytic Efficiency of the Synthetic Analogues of Catechol Oxidase with Their Electrochemical Property in the Free State and Substrate-Bound State. *Inorg. Chem.* **53**, 8257–8269 (2014).
53. Neves, A., Rossi, L. M., Bortoluzzi, A. J., Szpoganicz, B., Wiezbicki, C., Schwingel, E., Haase, W. & Ostrovsky, S. Catecholase activity of a series of dicopper(II) complexes with variable Cu-OH(phenol) moieties. *Inorg. Chem.* **41**, 1788–1794 (2002).
54. Belle, C., Beguin, C., Gautier-Luneau, I., Hamman, S., Philouze, C., Pierre, J. L., Thomas, F., Torelli, S., Saint-Aman, E. & Bonin, M. Dicopper(II) complexes of H-BPMP-type ligands: Ph-induced changes of redox, spectroscopic (19F NMR studies of fluorinated complexes), structural properties, and catecholase activities. *Inorg. Chem.* **41**, 479–491 (2002).
55. Sanyal, R., Ketkov, S., Purkait, S., Mautner, F. A., Zhigulin, G. & Das, D. Nuclearity dependent solvent contribution to the catechol oxidase activity of novel copper(ii) complexes derived from Mannich-base ligand platforms: synthesis{,} crystal structure and mechanism. *New J. Chem.* **41**, 8586–8597 (2017).
56. Wegner, R., Gottschaldt, M., Görls, H., Jäger, E. G. & Klemm, D. Copper(II) complexes of aminocarbohydrate β-ketoenaminic ligands: Efficient catalysts in catechol oxidation. *Chem. - A Eur. J.* **7**, 2143–2157 (2001).
57. Zippel, F., Ahlers, F., Werner, R., Haase, W., Nolting, H. F. & Krebs, B. Structural and functional models for the dinuclear copper active site in catechol oxidases: Syntheses, X-ray crystal structures, magnetic and spectral properties, and x-ray absorption spectroscopic studies in solid state and in solution. *Inorg. Chem.* **35**, 3409–3419 (1996).
58. Patel, R. N., Singh, N. & Gundla, V. L. N. Synthesis, characterization and superoxide dismutase activity of some octahedral nickel(II) complexes. *Polyhedron* **26**, 757–762 (2007).
59. Patel, R. N. Synthesis, characterization and superoxide dismutase activity of some four coordinated copper(ii) complexes. *Indian J. Chem. - Sect. A Inorganic, Phys. Theor. Anal. Chem.* **48**, 1370–1377 (2009).
60. Patel, R. N., Singh, N., Shukla, K. K. & Gundla, V. L. N. E.S.R., magnetic, electronic

and superoxide dismutase studies of imidazolate-bridged Cu(II)-Cu(II) complexes with ethylenediamine as capping ligand. *Spectrochim. Acta - Part A Mol. Biomol. Spectrosc.* **61**, 1893–1897 (2005).

61. Patel, M. N., Gandhi, D. S. & Parmar, P. A. SOD mimic activity, DNA binding and in-vitro antibacterial studies of drug based copper(II) complexes. *Inorg. Chem. Commun.* **13**, 618–621 (2010).
62. Patel, M. N., Bhatt, B. S. & Dosi, P. A. Study of SOD mimic and nucleic acid interaction activity exerted by enrofloxacin-based copper(II) complexes. *Chem. Biodivers.* **9**, 2810–2824 (2012).
63. Jakab, N. I., Jancsó, A., Gajda, T., Gyurcsik, B. & Rockenbauer, A. Copper(II), nickel(II) and zinc(II) complexes of N-acetyl-His-Pro-His-His-NH2: Equilibria, solution structure and enzyme mimicking. *J. Inorg. Biochem.* **102**, 1438–1448 (2008).
64. Abuhijleh, A. L. Mononuclear copper (II) salicylate complexes with 1,2-dimethylimidazole and 2-methylimidazole: Synthesis, spectroscopic and crystal structure characterization and their superoxide scavenging activities. *J. Mol. Struct.* **980**, 201–207 (2010).
65. Pierre, J. L., Chautemps, P., Refaif, S., Beguin, C., Marzouki, A. El, Serratrice, G., Saint-Aman, E. & Rey, P. Imidazolate-Bridged Dicopper(II) and Copper—Zinc Complexes of a Macrobicyclic Ligand (Cryptand). A Possible Model for the Chemistry of Cu—Zn Superoxide Dismutase. *J. Am. Chem. Soc.* **117**, 1965–1973 (1995).
66. Guo, D., Li, C., Liu, G., Luo, X. & Wu, F. Oxidase Mimetic Activity of a Metalloporphyrin-Containing Porous Organic Polymer and Its Applications for Colorimetric Detection of Both Ascorbic Acid and Glutathione. *ACS Sustain. Chem. Eng.* **9**, 5412–5421 (2021).
67. He, S.-B., Hu, A.-L., Zhuang, Q.-Q., Peng, H.-P., Deng, H.-H., Chen, W. & Hong, G.-L. Ascorbate Oxidase Mimetic Activity of Copper(II) Oxide Nanoparticles. *ChemBioChem* **21**, 978–984 (2020).
68. Liu, C., Cai, Y., Wang, J., Liu, X., Ren, H., Yan, L., Zhang, Y., Yang, S., Guo, J. & Liu, A. Facile Preparation of Homogeneous Copper Nanoclusters Exhibiting Excellent Tetraenzyme Mimetic Activities for Colorimetric Glutathione Sensing and Fluorimetric Ascorbic Acid Sensing. *ACS Appl. Mater. Interfaces* **12**, 42521–42530 (2020).
69. Weng, C. H., Cheng, S. C., Wei, H. M., Wei, H. H. & Lee, C. J. Magnetostructural correlations and catecholase-like activities of μ-alkoxo-μ-carboxylato double bridged dinuclear and tetranuclear copper(II) complexes. *Inorganica Chim. Acta* **359**, 2029–2040 (2006).
70. Nuñez, M., del Olmo, A. & Calzada, J. Biogenic Amines. *Encycl. Food Heal.* 416–423 (2015).
71. Jenkins, T. A., Nguyen, J. C. D., Polglaze, K. E. & Bertrand, P. P. Influence of tryptophan and serotonin on mood and cognition with a possible role of the gut-brain axis. *Nutrients* **8**, 56–70 (2016).
72. Grover, M., Linden, D. R., Akiba, Y. & Karunya, K. Gut Microbiota Produced Tryptamine Activates an Epithelial G- protein Coupled Receptor to Increase Colonic Secretion. *Cell Host Microbe* **23**, 775–785 (2018).
73. Cologno, D., Mazzeo, A., Lecce, B., Mundi, C., Petretta, V., Casucci, G. & D'Onofrio, F. Triptans: Over the migraine. *Neurol. Sci.* **33**, S193–S198 (2012).
74. Adrover, M., Vilanova, B., Frau, J., Muñoz, F. & Donoso, J. The pyridoxamine action on Amadori compounds: A reexamination of its scavenging capacity and chelating

effect. *Bioorganic Med. Chem.* **16**, 5557–5569 (2008).

75. Voziyan, P. A. & Hudson, B. G. Pyridoxamine as a multifunctional pharmaceutical: Targeting pathogenic glycation and oxidative damage. *Cell. Mol. Life Sci.* **62**, 1671–1681 (2005).
76. Chetverikova, V. A., Popov, L. D., Levchenkov, S. I., Burlov, A. S., Lazarenko, V. A., Zubavichus, Y. V. & Shcherbakov, I. N. Synthesis, Structural, and Physico-Chemical Study of Transition Metal Complexes with Schiff Base: A Product of Condensation of 2-N-Tosylaminobenzaldehyde and Tryptamine. *Russ. J. Gen. Chem.* **90**, 418–424 (2020).
77. Thierry, F. Y., Monisola, I. I., Berka, N. P. & Derek, N. T. Biological Applications of Tryptamine Schiff Base Derivatives. *9th Int'l Conf. Adv. Sci. Eng. Technol. Waste Manag. Nov. 27-28, 2017 Parys, South Africa* (2017).
78. Mathews, I. I. & Manohar, H. Synthesis, spectral and structural studies on metal complexes of Schiff bases involving vitamin B6 and histamine. *J. Chem. Soc. Dalt. Trans.* **1**, 2289–2294 (1991).
79. Akocak, S., Lolak, N., Vullo, D., Durgun, M. & Supuran, C. T. Synthesis and biological evaluation of histamine Schiff bases as carbonic anhydrase I, II, IV, VII, and IX activators. *J. Enzyme Inhib. Med. Chem.* **32**, 1305–1312 (2017).
80. Kanwal, Mohammed Khan, K., Salar, U., Afzal, S., Wadood, A., Taha, M., Perveen, S., Khan, H., Lecka, J., Sévigny, J. & Iqbal, J. Schiff bases of tryptamine as potent inhibitors of nucleoside triphosphate diphosphohydrolases (NTPDases): Structure-activity relationship. *Bioorg. Chem.* **82**, 253–266 (2019).
81. Touafri, L., Hellal, A., Chafaa, S., Khelifa, A. & Kadri, A. Synthesis, characterisation and DFT studies of three Schiff bases derived from histamine. *J. Mol. Struct.* **1149**, 750–760 (2017).
82. Liu, C., Niu, J. F., Li, Y., Xu, J. G. & Liu, X. H. Syntheses, crystal structures and antibacterial activities of cobalt(II) and manganese(II) complexes with Schiff base ligand derived from tryptamine. *Jiegou Huaxue* **35**, 1002–1010 (2016).
83. Banerjee, S., Dixit, A., Maheswaramma, K. S., Maity, B., Mukherjee, S., Kumar, A., Karande, A. A. & Chakravarty, A. R. Photocytotoxic ternary copper(II) complexes of histamine Schiff base and pyridyl ligands. *J. Chem. Sci.* **128**, 165–175 (2016).
84. Abe, M., Nakao, Y., Suzuki, S., Kimura, M. & Nakahara, A. Copper (II) Complexes of Schiff Based derived from Histamine or 2-(2-Aminoethyl)pyridine and 2,3-Burabedione or 4-Hydroxy-4-methyl-2-pentanone. *Bull. Chem. Soc. Jpn.* **55**, 3027–3028 (1982).
85. Padmaja, M., Anupama, B. & Gyana Kumari, C. Synthesis , Spectral Characterization , Molecular Modeling and Antimicrobial Studies of Transition Metal Complexes and the Schiff Base Derived From 3- Formylchromone and Tryptamine Synthesis , Spectral Characterization , Molecular Modeling and Antimicrobi. *Asian J. Res. Chem.* **4**, 1043–1049 (2011).
86. Ishida, T., Hatta, K., Yamashita, S., Doi, M. & Inoue, M. Crystal Structure of Copper(II) Complex with Tryptamine-Pyridoxal Schiff Base and Conformational Study of Tryptophan in Pyridoxal-Catalyzed Reactions. *Chem. Pharm. Bull.* **34**, 3553–3562 (1986).
87. Verani, C. N., Rentschler, E., Weyhermüller, T., Bill, E. & Chaudhuri, P. Exchange coupling in a bis(heterodinuclear) [CuIINiII]2 and a linear heterotrinuclear complex CoIIICuIINiII. Synthesis, structures and properties. *J. Chem. Soc. Dalt. Trans.* **3**, 251–

258 (2000).
88. Potapov, A. S., Nudnova, E. A., Domina, G. A., Kirpotina, L. N., Quinn, M. T., Khlebnikov, A. I. & Schepetkin, I. A. Synthesis, characterization and potent superoxide dismutase-like activity of novel bis(pyrazole)-2,2′-bipyridyl mixed ligand copper(II) complexes. *Dalt. Trans.* 4488–4498 (2009).
89. Patel, M. N., Patel, C. R. & Joshi, H. N. Metal-based biologically active compounds: Synthesis, characterization, DNA interaction, antibacterial, cytotoxic and SOD mimic activities. *Appl. Biochem. Biotechnol.* **169**, 1329–1345 (2013).
90. Dolomanov, O. V., Bourhis, L. J., Gildea, R. J., Howard, J. A. K. & Puschmann, H. OLEX2: A complete structure solution, refinement and analysis program. *J. Appl. Crystallogr.* **42**, 339–341 (2009).
91. Sheldrick, G. M. A short history of SHELX. *Acta Crystallogr. Sect. A Found. Crystallogr.* **64**, 112–122 (2008).
92. Sheldrick, G. M. Crystal structure refinement with SHELXL. *Acta Crystallogr. Sect. C* **71**, 3–8 (2015).
93. Frisch, M. J., Trucks, G. W., Schlegel, H. B., Scuseria, G. E., Robb, M. A., Cheeseman, J. R., Scalmani, G., Barone, V., Petersson, G. A., Nakatsuji, H., Li, X., Caricato, M., Marenich, A. V., Bloino, J., Janesko, B. G., Gomperts, R., Mennucci, B., Hratchian, H. P., Ortiz, J. V. *et al.* Gaussian 16, Revision A.03. *Gaussian, Inc., Wallingford CT* (2016).
94. Stephens, P. J., Devlin, F. J., Chabalowski, C. F. & Frisch, M. J. Ab Initio Calculation of Vibrational Absorption and Circular Dichroism Spectra Using Density Functional Force Fields. *J. Phys. Chem.* **98**, 11623–11627 (1994).
95. Hay, P. J. & Wadt, W. R. Ab initio effective core potentials for molecular calculations. Potentials for K to Au including the outermost core orbitals. *J. Chem. Phys.* **82**, 299–310 (1985).
96. Wadt, W. R. & Hay, P. J. Ab initio effective core potentials for molecular calculations. Potentials for main group elements Na to Bi. *J. Chem. Phys.* **82**, 284–298 (1985).
97. Dennington, R., Keith, T. A. & Millam, J. M. GaussView, Version 6. at (2016).
98. Grzybowski, J. J., Merrell, P. H. & Urbach, F. L. Binuclear Metal Complexes. 1. Dicopper(II) Complexes with Binucleating Ligands Derived from 2-Hydroxy-5-methylisophthalaldehyde and 2-(2-Aminoethyl)pyridine or Histamine. *Inorg. Chem.* **17**, 3078–3082 (1978).
99. Lorösch, J. & Haase, W. Crystal structure and magnetic properties of an asymmetric bridged binuclear Cu(II)-complex with a macrocyclic ligand derived from 2-hydroxy-5-methyl-isophthalaldehyde and histamine. *Inorganica Chim. Acta* **108**, 35–40 (1985).
100. Bleaney, B. & Bowers, K. D. Anomalous paramagnetism of copper acetate. *Proc. R. Soc. London. Ser. A. Math. Phys. Sci.* **214**, 451–465 (1952).
101. Crawford, V. H., Richardson, H. W., Wasson, J. R., Hodgson, D. J. & Hatfield, W. E. Relation between the singlet-triplet splitting and the copper-oxygen-copper bridge angle in hydroxo-bridged copper dimers. *Inorg. Chem.* **15**, 2107–2110 (1976).
102. Gupta, R., Mukherjee, S. & Mukherjee, R. Synthesis, magnetism, 1H NMR and redox activity of dicopper(II) complexes having a discrete {Cu2(μ-phenoxide)2}2+ unit supported by a non-macrocyclic ligand environment. Crystal structure of [Cu2(L)2(OClO3)2] [HL = 4-methyl-2,6-bis(pyrazol-1-ylmethyl)phen. *J. Chem. Soc. Dalt. Trans.* 4025–4030 (1999).
103. Saimiya, H., Sunatsuki, Y., Kojima, M., Kashino, S., Kambe, T., Hirotsu, M., Akashi, H., Nakajima, K. & Tokii, T. Antiferromagnetism induced by successive protonation of

terminal phenol groups of a bis(μ-phenoxide)-bridged dicopper(II,II) complex. *J. Chem. Soc. Dalt. Trans.* 3737–3742 (2002).

104. Chattopadhyay, T., Banu, K. S., Banerjee, A., Ribas, J., Majee, A., Nethaji, M. & Das, D. A novel single pot synthesis of binuclear copper(II) complexes of macrocyclic and macroacyclic compartmental ligands: Structures and magnetic properties. *J. Mol. Struct.* **833**, 13–22 (2007).
105. Nag, K. Structure function relationship in some macrocyclic dicopper complexes. *Proc. Indian Acad. Sci. Chem. Sci.* **102**, 269–282 (1990).
106. Thirumavalavan, M., Akilan, P., Kandaswamy, M., Chinnakali, K., Kumar, G. S. & Fun, H. K. Synthesis of lateral macrobicyclic compartmental ligands: Structural, magnetic, electrochemical, and catalytic studies of mono- and binuclear copper(II) complexes. *Inorg. Chem.* **42**, 3308–3317 (2003).
107. Ruiz, E., Alemany, P., Alvarez, S. & Cano, J. Structural Modeling and Magneto-Structural Correlations for Hydroxo-Bridged Copper(II) Binuclear Complexes. *Inorg. Chem.* **36**, 3683–3688 (1997).
108. Ruiz, E., Alemany, P., Alvarez, S. & Cano, J. Toward the prediction of magnetic coupling in molecular systems: Hydroxo- and alkoxo-bridged Cu(II) binuclear complexes. *J. Am. Chem. Soc.* **119**, 1297–1303 (1997).
109. Shoba, D., Periandy, S., Karabacak, M. & Ramalingam, S. Vibrational spectroscopy (FT-IR and FT-Raman) investigation, and hybrid computational (HF and DFT) analysis on the structure of 2,3-naphthalenediol. *Spectrochim. Acta Part A Mol. Biomol. Spectrosc.* **83**, 540–552 (2011).
110. Fukui, K. Role of Frontier Orbitals in Chemical Reactions. *Science (80-.).* **218**, 747–754 (1982).
111. Wang, Q., Chen, D., Liu, X. & Zhang, L. Theoretical mechanisms of the superoxide radical anion catalyzed by the nickel superoxide dismutase. *Comput. Theor. Chem.* **966**, 357–363 (2011).
112. Jawaria, R., Hussain, M., Khalid, M., Khan, M. U., Tahir, M. N., Naseer, M. M., Braga, A. A. C. & Shafiq, Z. Synthesis, crystal structure analysis, spectral characterization and nonlinear optical exploration of potent thiosemicarbazones based compounds: A DFT refine experimental study. *Inorganica Chim. Acta* **486**, 162–171 (2019).
113. Koopmans, T. Über die Zuordnung von Wellenfunktionen und Eigenwerten zu den Einzelnen Elektronen Eines Atoms. *Physica* **1**, 104–113 (1934).
114. Yang, L., Powell, D. R. & Houser, R. P. Structural variation in copper(i) complexes with pyridylmethylamide ligands: structural analysis with a new four-coordinate geometry index, τ4. *Dalt. Trans.* 955–964 (2007) doi:10.1039/B617136B.
115. Terra, W. S., Ferreira, S. S., Costa, R. O., Mendes, L. L., Franco, R. W. A., Bortoluzzi, A. J., Resende, J. A. L. C., Fernandes, C. & Horn, A. Evaluating the influence of the diamine unit (ethylenediamine, piperazine and homopiperazine) on the molecular structure, physical chemical properties and superoxide dismutase activity of copper complexes. *Inorganica Chim. Acta* **450**, 353–363 (2016).
116. Weser, U. & Schubotz, L. M. Imidazole-bridged copper complexes as Cu2Zn2-Superoxide dismutase models. *J. Mol. Catal.* **13**, 249–261 (1981).
117. Singh, Y., Patel, R. N., Patel, S. K., Jadeja, R. N., Patel, A. K., Patel, N., Roy, H., Bhagriya, P., Singh, R., Butcher, R. J., Jasinski, J. P., Herrero, S. & Cortijo, M. Supramolecular assemblies of new pseudohalide end-to-end bridged copper(II) complex and molecular structural variety of penta and hexa-coordinted metal(II) complexes with

hydrazido-based ligand. *Inorganica Chim. Acta* **503**, 119371 (2020).

118. Patel, R. N., Singh, Y., Singh, Y. P., Patel, A. K., Patel, N., Singh, R., Butcher, R. J., Jasinski, J. P., Colacio, E. & Palacios, M. A. Varying structural motifs, unusual X-band electron paramagnetic spectra, DFT studies and superoxide dismutase enzymatic activity of copper(ii) complexes with N′-[(E)-phenyl(pyridin-2-yl)methylidene]benzohydrazide. *New J. Chem.* **42**, 3112–3136 (2018).
119. Patel, R. N., Patel, D. K., Sondhiya, V. P., Shukla, K. K., Singh, Y. & Kumar, A. Synthesis, crystal structure and superoxide dismutase activity of two new bis(μ-acetato/μ-nitrato) bridged copper(II) complexes with N′-[phenyl(pyridin-2-yl)methylidene]benzohydrazone. *Inorganica Chim. Acta* **405**, 209–217 (2013).
120. Bhardwaj, V., Salunke, P. S., Puranik, A. A., Kulkarni, N. D. & Ballabh, A. Design and synthesis of novel heterocyclic pivalamide ligands and their copper(II) complexes: Structure, BSA/DNA interactions and SOD synzyme activity. *Polyhedron* **225**, 116054 (2022).
121. Monzani, E., Battaini, G., Perotti, A., Casella, L., Gullotti, M., Santagostini, L., Nardin, G., Randaccio, L., Geremia, S., Zanello, P. & Opromolla, G. Mechanistic, structural, and spectroscopic studies on the catecholase activity of a dinuclear copper complex by dioxygen. *Inorg. Chem.* **38**, 5359–5369 (1999).
122. Monzani, E., Quinti, L., Perotti, A., Casella, L., Gullotti, M., Randaccio, L., Geremia, S., Nardin, G., Faleschini, P. & Tabbì, G. Tyrosinase models. Synthesis, structure, catechol oxidase activity, and phenol monooxygenase activity of a dinuclear copper complex derived from a triamino pentabenzimidazole ligand. *Inorg. Chem.* **37**, 553–562 (1998).
123. Ackermann, J., Meyer, F., Kaifer, E. & Pritzkow, H. Tuning the Activity of Catechol Oxidase Model Complexes by Geometric Changes of the Dicopper Core. *Chem. – A Eur. J.* **8**, 247–258 (2002).

•